

Electronic Thesis and Dissertation Repository

---

8-12-2019 3:00 PM

## Porous membranes from 2D materials and their integration into chemiresistive sensors for in-line detection of cadmium in water filtration devices

Sheldon Van Middelkoop, *The University of Western Ontario*

Supervisor: Fanchini, Giovanni, *The University of Western Ontario*

A thesis submitted in partial fulfillment of the requirements for the Master of Science degree in Physics

© Sheldon Van Middelkoop 2019

Follow this and additional works at: <https://ir.lib.uwo.ca/etd>

 Part of the [Condensed Matter Physics Commons](#)

---

### Recommended Citation

Van Middelkoop, Sheldon, "Porous membranes from 2D materials and their integration into chemiresistive sensors for in-line detection of cadmium in water filtration devices" (2019). *Electronic Thesis and Dissertation Repository*. 6359.  
<https://ir.lib.uwo.ca/etd/6359>

This Dissertation/Thesis is brought to you for free and open access by Scholarship@Western. It has been accepted for inclusion in Electronic Thesis and Dissertation Repository by an authorized administrator of Scholarship@Western. For more information, please contact [wlsadmin@uwo.ca](mailto:wlsadmin@uwo.ca).

## Abstract

As the global population increases, the need for drinking water is an ever-present concern. Water contamination from cadmium needs to be avoided due to the damaging effects of Cd divalent cations to human health. The Environmental Protection Agency (EPA) has set an extremely low permissible limit for Cd<sup>2+</sup> in water, at 5 parts-per-billion (PPB), which poses extreme challenges towards Cd<sup>2+</sup> detection and retention in specific water purification devices. This has led to a rush in the development of low-cost and scalable devices with in-line Cd<sup>2+</sup> sensing capabilities, with the ability to simultaneously purify water and monitor its quality, as opposed to less effective off-line monitoring systems that cannot be integrated in water purification apparatus. The goal of my thesis is to fabricate, and explore for sensing purposes, porous membranes assembled from novel two-dimensional (2D) materials. Our goal is to integrate these membranes into nanofiltration devices previously developed by Fanchini's group, with the objective to selectively detect Cd<sup>2+</sup> in concentrations at or below the EPA's limit. In this thesis, membranes assembled from two distinct 2D materials have been incorporated into a computer-controlled chemiresistive sensing platform I have specially designed for this work: (1) multilayer graphene platelets exfoliated from low-defect hydrothermal graphite using block copolymers, and (2) L-cysteine functionalized molybdenum disulfide (MoS<sub>2</sub>) platelets. Platelets of 2D materials have large surface areas. Adsorption of metal ions onto their surfaces during water permeation alters the electronic properties of 2D electron gases confined in these materials, thus affecting their electrical conductivity. More critical is to attain these effects only when Cd<sup>2+</sup>, not other ions, are absorbed. Selective electrical conductivity changes due to Cd<sup>2+</sup> absorption has been observed in this thesis, both in block-copolymer exfoliated multilayer graphene (down to about 1 PPB) and L-cysteine functionalized MoS<sub>2</sub> (down to 0.1 PPB). In the first case, Cd selectivity has been

obtained by adjusting the distance between graphene layers at values matching the hydrodynamic radius of  $\text{Cd}^{2+}$ . In the second case, selectivity to Cd is assigned to the preferential attachment of  $\text{Cd}^{2+}$  to L-cysteine functional groups, which alter the density of electronic gap states in  $\text{MoS}_2$ . Both types of chemiresistive sensing membranes perform at concentrations below the EPA's permissible limit for cadmium and can be easily integrated into water nanofiltration devices.

**Keywords:** Cadmium, EPA, Graphite, L-Cysteine, Molybdenum Disulfide, nanofiltration

## Authorship Statement

Chapter 1 was written by the author of this thesis and edited by Prof. Giovanni Fanchini.

Chapter 2 was written by the author of this thesis and edited by Prof. Giovanni Fanchini.

Chapter 3 was written by the author of this thesis and edited by Prof. Giovanni Fanchini. The author of this thesis designed (with some assistance from Prof. Giovanni Fanchini) and built the sensing apparatus discussed in this chapter. The author of this thesis also performed all experimental work required by the fabrication of multilayer graphene membranes, the preparation of  $\text{Cd}^{2+}$ ,  $\text{Mn}^{2+}$ , and  $\text{Hg}^{2+}$  solutions for water sensing, and carried out all of the sensing experiments and tests. The graphite/block-copolymer suspensions used for membrane fabrication were prepared by the author of this thesis, with some help from undergraduate student Andason Cen. Additional membrane characterization was performed by third parties: Raman and scanning electron microscopy (SEM) characterizations were performed by Dr. Paul Bazylewski, and analysis of the results was performed by the author of this thesis. X-Ray Diffraction (XRD) characterization was performed at Western's XRD facility. Samples for all of these additional characterization experiments were fabricated and provided by the author of this thesis. Electron paramagnetic resonance (EPR) characterization and analysis was performed by Dr. Reg Bauld. It has been published in *FlatChem* 17 (2019) 100118.

Chapter 4 was written by the author of this thesis and Dr. Paul Bazylewski and edited by Prof. Giovanni Fanchini and Dr. Ranjith Divigalpitiya from 3M Canada. The author of this thesis designed (with some assistance from Prof. Giovanni Fanchini) and fabricated the filtration apparatus used in this chapter. The author of this thesis carried out (with assistance from Dr. Paul

Bazylewski) the molybdenum disulphide membrane fabrication (including the preparation of various MoS<sub>2</sub> suspensions from material chemically functionalized by Dr. Paul Bazylewski) as well as all of the filtration experiments and tests. Additional characterization was completed at Western University Nanofabrication Facility. The author of this thesis performed all of the atomic force microscopy (AFM) characterization of the samples. It has been published in FlatChem 11 (2018) 15.

Chapter 5 was written by the author of this thesis and edited by Prof. Giovanni Fanchini

## Acknowledgements

First, I would like to express my gratitude towards my supervisor Prof. Giovanni Fanchini for all the patience and support over the past couple of years. You have been a great mentor and someone who has taught me a great deal, not only academically, but also regarding personal development. I will carry the skills and knowledge you have bestowed on me into the future. I thank you for your endless belief in my ability to tackle the interesting problems we often encountered during the projects we worked on together. Lastly, thank you for the awesome reference letters you have given me, it is greatly appreciated.

I would also like to acknowledge my group members as they have been instrumental to the success of my work as well as helping to keep the mood light. Dr. Paul Bazylewski was especially an incredible help, regarding my work. Not only did he teach me an enormous amount in lab. He also often gave very useful ideas to help me solve the many problems I encountered. I would also like to thank Dr. Deepa Singh, Victor Wong, Angela Ezugwu, and Andason Cen for being awesome colleagues.

I want to thank the faculty members of the Department of Physics and Astronomy at the University of Western Ontario from whom I had a pleasure learning from. I would like to especially thank Prof. Wayne Hocking for his very interesting course on statistical mechanics, which taught me an enormous amount about ‘down to earth physics’. Additionally, I would also like to thank Prof. Allan MacIssac for his fascinating course on mathematical modelling and simulation. Lastly, I would also like to acknowledge all other professors whose courses I have taken.

I would also like to thank the staff of the Department of Physics and Astronomy, for their endless high-quality work and commitment to the maintenance of UWO.

Lastly, I would like to thank my family and friends for all their support in my endeavours. I would like to thank my mom, dad, sister, and last but certainly not least my loving girlfriend for their endless encouragement.

## Summary for Lay Audience

Due to the enormous use of cadmium in industry, as well as natural sources of contamination, such as volcanoes, cadmium is often found in water supplies and ecological systems around the world. Cadmium has negative health effects on human populations by causing substantial lung, and renal damage, bone demineralization, and even brain damage in children. Current methods of detecting and capturing cadmium are expensive, off-line and require trained personnel. In order to address these issues, we looked at two different 2D materials, (1) graphene and (2) molybdenum disulfide. In chapter 3, multi layer graphene was exfoliated allowing the graphene flakes to be held in suspension for long periods of time. The exfoliation process was found to change the spacing between layers of multi layer graphene. This was found to be ideal for capturing and sensing heavy metal ions, specifically cadmium. The apparatus has a chemically resistive (chemiresistor) design and is simple and easy to manufacture without the need for on site trained personnel. In chapter 4, we looked at utilizing exfoliated MoS<sub>2</sub>, which has been functionalized with L-Cysteine, an amino acid commonly found in biological systems. Due to the high affinity of heavy metal ions towards L-Cysteine, functionalizing MoS<sub>2</sub> allows for the selective capture of cadmium divalent cations.

# Table of Contents

Abstract.....	ii
Authorship Statement.....	iv
Acknowledgements.....	vi
Summary for Lay Audience.....	viii
Table of Contents.....	ix
List of Figures.....	xii
List of Tables.....	xvii
List of Abbreviations.....	xviii
Chapter 1: Introduction.....	1
1.1 Graphene.....	1
1.1.1 Physical Structure of Graphene.....	2
1.1.2 Electronic Structure of Graphene.....	5
1.2 Molybdenum Disulfide.....	8
1.3.1 Physical Structure of MoS <sub>2</sub> .....	9
1.3.2 Electronic Structure of MoS <sub>2</sub> .....	10
1.3 2D Materials for Water Purification.....	11
1.4.1 Vacuum Filtration.....	14
1.4 Thesis Overview.....	15
Chapter 2: Experimental Techniques.....	21
2.1 Thermal Evaporation.....	21
2.2 Raman Spectroscopy.....	24
2.2.1 Raman Spectroscopy of Graphene.....	27
2.3 Atomic Force Microscopy.....	29
2.4 Electron Paramagnetic Resonance .....	32
2.5 X-Ray Diffraction .....	34

Chapter 3: Multi layer graphene chemiresistor for detecting Cd <sup>2+</sup> .....	42
3.1 Materials and Methods.....	43
3.1.1 Sensor and Platform Design.....	43
3.1.2 Sensor Data Acquisition.....	46
3.1.3 Sensing Experiments.....	47
3.1.4 Scanning Electron Microscopy.....	48
3.1.5 Raman Spectroscopy.....	49
3.1.6 Electron Paramagnetic Resonance.....	49
3.1.7 Powder X-Ray Diffraction.....	50
3.2 Results and Discussion.....	50
3.2.1 Membrane Characterization.....	50
3.2.1.1 Scanning Electron Microscopy.....	50
3.2.1.2 Raman Spectroscopy.....	52
3.2.1.3 Electron Paramagnetic Resonance.....	54
3.2.1.4 Powder X-Ray Diffraction.....	56
3.2.2 Chemiresistor Sensing Performance.....	58
3.2.2.1 Effect of Molecular Weight of Surfactant on Sensing Performance.....	64
3.4 Conclusion.....	67
Chapter 4: L-Cysteine Functionalized MoS <sub>2</sub> for Selective Capture Cd <sup>2+</sup> .....	70
4.1 Introduction.....	70
4.2 Experimental.....	72
4.2.1 Exfoliated MoS <sub>2</sub> .....	72
4.2.2 Cysteine Functionalization.....	73
4.2.3 Raman/FTIR/UV-Vis.....	75
4.2.4 SEM/EDX/AFM/TGA/XRD.....	76
4.3 Results and Discussion.....	77
4.3.1 MoS <sub>2</sub> Nanosheet Characterization.....	77

4.3.2 Preferred Sensitivity to Cd <sup>2+</sup> ions.....	87
4 Conclusion.....	91
Chapter 5: Conclusion and Future Work.....	97
5.1 Conclusion.....	97
5.2 Future Work.....	98
5.3 List of Permissions.....	100
5.4 Appendix.....	106
5.5 Curriculum Vitae.....	110

## List of Figures

Figure 1.1 a) Electron configuration of ground state of carbon b) Promotion of  $2s^2$  electron into the  $2p_z$  state

Figure 1.2: Different allotropes of carbon a) diamond, b) graphite, c)  $C_{60}$  fullerene (buckyball), d) amorphous carbon, e) carbon nanotube (CN)

Figure 1.3: a) Shows graphene's honeycomb structure, the unit cell (blue) is shown along with the diatomic basis labelled with A and B, primitive vectors are also shown as  $a_1$  and  $a_2$  b) shows the Brillouin zone with k-points shown (grey), the reciprocal lattice vectors are also shown and denoted as  $g_1$  and  $g_2$

Figure 1.4: Energy dispersion relation for a) typical semiconductor and b) graphene. Blue and red colors represent the conduction and valence bands respectively.

Figure 1.5: a) Honeycomb structure of  $MoS_2$  with unit cell (green), b) sides view of  $MoS_2$  multilayer structure showing Mo (dark blue) and S (light blue)

Figure 1.6: First Brillouin zone of  $MoS_2$  showing the reciprocal lattice vectors  $K_1$  and  $K_2$ , as well as high symmetry points  $\Gamma$ ,  $K$ ,  $K'$ ,  $M$

Figure 1.7: Images of current cadmium detection methods a) atomic emission spectroscope, b) electrochemical cells, and c) thiolated gold nanoparticle based chemiresistors

Figure 1.8: Comparison between two filtration architectures a) shows a water filtration apparatus operating in a dead-end design b) shows a cross flow architecture

Figure 2.1: Thermal evaporation setup

Figure 2.2: Illustration from which Langmuire-Knudsen relation is derived

Figure 2.3: Illustration of shadow masking technique used to pattern a  $25\ \mu\text{m}$  gap between aluminum electrodes

Figure 2.4: A comparison of various Raman scattering processes. a) shows the process of Rayleigh scattering, where the energy of the absorbed and emitted photons are equal, b) shows Stokes scattering where a photon is absorbed and the Raman active mode takes some energy and emits a photon with less energy, c) shows the anti-Stokes scattering where a photon is absorbed in a material which already has excited vibrational modes, the emitted photon has the same energy as the vibrational mode plus the absorbed photon

Figure 2.5: Diagram of Raman spectrometer where light interacts with sample, and Raman shifted light is emitted from sample and directed into spectrograph

Figure 2.6: Raman spectrum of graphene showing D, G, and 2D peaks

Figure 2.7: Atomic force microscope (AFM), a) shows device schematic, b), c) and d) show contact mode, non-contact mode, and tapping mode AFM, respectively

Figure 2.8: Regions in the Lennard-Jones potential where different AFM modes operate, contact mode (blue) operates in the repulsive region where the tip is closest to the sample, tapping mode (magenta) operates in the most attractive region where the tip is moderately close to sample, and non-contact mode (green) which operates where the distance between the tip and sample is large and the electrostatic attraction is minimal

Figure 2.9: X-ray diffraction setup a) shows an XRD schematic consisting of monochromatic X-ray source which is then collimated and directed to sample where diffraction pattern is produced, b) shows the process of Bragg diffraction c) shows a typical XRD spectra of graphite, graphene, and graphene oxide

Figure 2.10: Electron paramagnetic resonance technique a) shows schematic of apparatus where sample (blue) is placed into microwave cavity where microwaves (pink) interact with paramagnetic centers (red), Helmholtz coils induced tunable magnetic fields, b) shows the Zeeman effect where the energy separation of electron spins is tunable by application of magnetic field, c) shows typical spectra of EPR with both the absorption and the first derivative (signal)

Figure 3.1. Graphene-based water filtration and sensing apparatus used in this study. The apparatus utilizes a data acquisition card to create IV curves which allows a computer to

calculate the resistivity across the gap cell. The gap cell is the area in between the two aluminum contacts (black and blue). Water is filtered through this apparatus with various types of contaminants and with varying concentrations. The graphene-based filter cake captures contaminants which results in a change in the gap cells resistivity acquired over time by the data acquisition system.

Figure 3.2: Scanning Electron Microscopy images showing filtration “cakes” prepared from synthetic graphite (top row) at (a) low and (b) high magnification; and natural vein graphite at (a) low and (b) high magnification. Comparison of micrographs recorded from synthetic and hydrothermal graphite reveal that the flake size is the same in both cases.

Figure 3.3: Raman spectra showing the G ( $1580\text{ cm}^{-1}$ ) and D ( $1360\text{ cm}^{-1}$ ) peaks of natural vein and synthetic graphite, as well as the second-order 2D peak. The higher D peak and  $I_D/I_G$  ratio of synthetic graphite is clearly noticeable

Fig. 3.4: Concentration of paramagnetic point defects determined from EPR measurements showing the number of spins of hydrothermal vein graphite versus the average size of graphite flakes suggesting that a vast majority of defects sit on the edge of measured flakes.

Figure 3.5: (a) X-ray diffraction spectra of graphite powder and multilayer graphene exfoliated from different surfactants. The (002) peak is evident in all cases. A satellite peak is present in SDS-exfoliated multilayer graphene, indicating a multimodal distribution in c-axis spacings; (b) detail of (002) peaks showing shifts different at different values of  $2\theta$  as a consequence of different c-axis spacings; (c) c-axis spacings calculated using Bragg’s law. We anticipate that different c-axis spacings lead to different abilities to selectively trap  $\text{Cd}^{2+}$  ions in multilayer graphene interlayers, different electrical properties of graphene and, therefore, tunable sensing performance.

Figure 3.6: Response, in terms of resistivity change, of a sensing system with graphene-based active component prepared from natural hydrothermal vein graphite to (a)  $\text{Cd}^{2+}$ , (b)  $\text{Mn}^{2+}$ , and (c)  $\text{Hg}^{2+}$  divalent cations at 125 ppb concentration.

Figure 3.7: Suggested mechanism for capture and sensing of  $\text{Cd}^{2+}$  ions from water by multilayer graphene. Ions get trapped between layers of graphite when their hydrodynamic diameter is close to the interlayer spacing between graphene planes, which is on its turn controlled by intercalation

of PEG-PPG-PEG of different chain length. Smaller divalent cations are not retained within the interlayer spacings, while excessively larger ions are not able to intercalate graphene layers.

Figure 3.8: Relative change of resistivity of the sensing system as a function of the concentration of  $\text{Cd}^{2+}$  and manganese  $\text{Mn}^{2+}$  divalent cations in water. Resistivity changes at 5 ppb, 25 ppb, 125 ppb, and 500 ppb concentrations are reported, with a linear regime at low concentrations and a saturation regime at higher concentrations.

Figure 3.9: Comparison of the responses to  $\text{Cd}^{2+}$  divalent cations at different concentrations with sensing systems using multilayer graphene sensing “cakes” prepared from (a) natural graphite and (b) synthetic/turbostratic graphite.

Figure 3.10: Response of chemiresistors prepared with varying PEG-PPG-PEG molecular weight using natural hydrothermal vein graphite. Data refer to the insertion of 125 ppb of cadmium in water. It can be observed that  $M_n=14,600$  amu lead to the best sensing performance.

Figure 3.11. Density and volume changes of multilayer graphene “cakes” as a function of the molecular weight of PEG-PPG-PEG copolymer used to exfoliate graphite, indicating that the molecular weight has effects on the multilayer graphene density and, therefore, on the interlayer spacing distance. Data refer to multi-layer graphene exfoliated from hydrothermal vein graphite.

Figure 4.1: Scheme of the process used to functionalize  $\text{MoS}_2 - \text{COOH}$  with L-cysteine. Three possible reaction pathways that may result in a stable amide bond or a regenerated carboxyl group are indicated. NHS is used to stabilize the reaction and prevent quenching of the intermediate ester and subsequent regeneration of the carboxyl group, such that reaction pathway (3) dominates. Images of the  $\text{MoS}_2\text{-COOH}$  and  $\text{MoS}_2\text{-Cys}$  solutions after sedimentation are shown.

Figure 4.2: Characterization of thioglycolic acid-exfoliated  $\text{MoS}_2$  flakes: (a) Tapping mode AFM topography and (b) phase images Comparison of AFM images for  $\text{MoS}_2\text{-COOH}$  filtrated onto polycarbonate membranes. (c) An SEM image of  $\text{MoS}_2$  flakes filtrated onto a track etched polycarbonate membrane shows small flakes ranging from 100 to 300 nm in diameter. (d) AFM cross sections, showing that the thickness of  $\text{MoS}_2$  flakes prior to functionalization with L-cysteine is in the 7–12 nm range, with an average height of  $10 \pm 1$  nm. (e) UV–Vis spectra of  $\text{MoS}_2\text{-COOH}$  and  $\text{MoS}_2\text{-Cys}$  water solutions, identifying two blue-shifted excitonic peaks.

Figure 4.3: (a) Raman spectra of MoS<sub>2</sub>-COOH compared to MoS<sub>2</sub>-Cys. (b) Characteristic peaks of MoS<sub>2</sub> before and after L-cysteine functionalization. After the addition of L-cysteine, characteristic L-cysteine bands are visible in the Raman spectrum. (c) Raman bands representing SH stretching modes in L-cysteine can be identified and they are necessary for the coordination of metal ions. (d) FTIR spectra confirm the results from Raman, showing peaks representing amide bonds between MoS<sub>2</sub> and cysteine.

Figure 4.4: Powder X-ray diffraction patterns of the MoS<sub>2</sub> original powder (blue line) and powder samples prepared from solution after mixing with thioglycolic acid (red line) and after L-cysteine functionalization (black line).

Figure 4.5: (a) Membranes prepared from MoS<sub>2</sub>-COOH or MoS<sub>2</sub>-Cys solution by vacuum filtration onto PES membranes (42 mm diameter) with different filtration volumes as labelled. (b) The change in ionic conductivity of a 10 ppm soaking solution due to adsorption of Cd or Mn metal ions versus the mass of MoS<sub>2</sub>-Cys deposited on the filter, compared to a bare PES support and a reference MoS<sub>2</sub>-COOH membrane. (c) EDX shows evidence of Cd absorbed to the surface MoS<sub>2</sub>-Cys, while Mn could not be detected on either MoS<sub>2</sub>-Cys or the MoS<sub>2</sub>-COOH reference (Fig. A3). Si, Al, and Ag signals are also present from the stub used to mount the sample, as well as from silver paste. (d) TGA analysis of MoS<sub>2</sub>-Cys after exposure to 50 ppm Mn or Cd metal ions in solution. Examination of the residual inorganic products shows a larger mass of absorbed Cd compared to Mn. The control sample was tested as-prepared without any metal ion exposure.

## List of Tables

Table 3.1:  $I_D/I_G$  and  $L_a$  values from Raman on natural (hydrothermal) and synthetic graphite.

Table 4.1: Experimental Raman peak assignments.  $\omega(a)$ -mode and  $\omega(b)$ -mode refer to notation in Fig. 4.3.

Table 4.2: Experimental FTIR peak assignments

Table 4.3: Elemental atomic and weight composition of Cysteine functionalized  $\text{MoS}_2$  nanosheets determined from analysis of the EDX spectra shown in Fig. 4.5.

## List of Abbreviations

0D	0-dimensional
1D	1-dimensional
2D	2-dimensional
3D	3-dimensional
AFM	Atomic Force Microscopy
AMU	Atomic Mass Unit
Al	Aluminum
Ag	Silver
As	Arsenic
BZ	Brillouin Zone
CCD	Charged Coupled Device
Cd	Cadmium
CdCl <sub>2</sub>	Cadmium (II) Chloride
CdS	Cadmium Sulfide
CdSe	Cadmium Selenide
CNT	Carbon Nanotube
COOH	Carboxylic Acid
Cr	Chromium
Cu	Copper
DAQ	Digital-Analog Data Acquisition
DI	DeIonized
EDC	Ethylcarbodiimid Hydrochloride
EDX	Energy-Dispersive X-Ray Spectroscopy
EPR	Electron Paramagnetic Resonance
EPA	Environmental Protection Agency
ESR	Electron Spin Resonance

FBZ	First Brillouin Zone
FTIR	Fourier Transform Infrared
GNR	Graphene Nanoribbon
Hg	Mercury
KPFM	Kelvin Probe Force Microscopy
LED	Light Emitting Diode
MoS <sub>2</sub>	Molybdenum Disulfide
Mn	Manganese
MnCl <sub>2</sub>	Manganese (II) Chloride
NHS	N-Hydroxysuccinimide
Ni	Nickel
NiCd	Nickel Cadmium
NR	Nanorod
Pb	Lead
PbS	Lead (II) Sulfide
PEG	Poly(ethylene)Glycol
PPB	Parts per Billion
PPG	Poly(propylene)Glycol
PPM	Parts per Million
PPT	Parts per Trillion
QD	Quantum Dot
RO	Reverse Osmosis
SEM	Scanning Electron Microscopy
SDS	Sodium Dodecyl Sulfate
SPM	Scanning Probe Microscopy
TBA	Tight Binding Approximation
TGA	Thermogravimetric Analysis
TGA	Thioglycolic Acid

UHV	Ultra High Vacuum
UV-Vis	Ultra Violet - Visible
XRD	X-Ray Diffraction
Zn	Zinc

# Chapter 1

## 1 Introduction

In recent years 2-dimensional (2D) materials have garnered significant attention due to their interesting and strange material properties. Most notably graphene has become a household name. This is due to the enormous possible applications the material promises. Graphene's unique electronic structure is of particular interest, yielding possible drastic improvements to the electronics industry. These include but are not limited to solar cells, capacitors, batteries, and more. Graphene may also allow for improvements in the field of water filtration and sensing. Many post-graphene materials have been investigated such as 'phosphorene', however these materials are often difficult to work with and sometimes even dangerous. Molybdenum disulfide ( $\text{MoS}_2$ ) is a post graphene semiconducting material, which is safe to use, and can easily be exfoliated into a 2D crystalline structure. This has led to massive research efforts into this material. The field of water filtration and sensing has had major improvements due to both graphene and  $\text{MoS}_2$ .

### 1.1 Graphene

The term 'graphene' was originated by H.P Boehm in 1962. [1] In 2004, Novoselov and Geim through a technique called mechanical exfoliation were able to isolate graphene for the first time. [2] Graphene is a two-dimensional (2D) material composed of carbon atoms in a honeycomb lattice. Each of the carbon atoms are bonded to three adjacent carbon atoms by a sigma ( $\sigma$ ) bond and one  $\pi$ -bond which is oriented out of the plane. Six carbon atoms are covalently bonded in hexagons which extend 'infinitely' throughout the xy-plane.

Graphene is of great interest to researchers due to its many useful properties. The strong covalent (C-C) bonds caused by the  $sp^2$  hybridization gives graphene an immense mechanical strength. [3] In addition to its mechanical strength, graphene also has a high thermal conductivity on the order of 5000 W/mK, high electron mobility (250,00  $cm^2/V s$ ) at room temperature, large optical transparency (>90%), as well as a very large surface area (2630  $m^2/g$ ). [3-9] As previously mentioned, the electronic properties of graphene have been especially exciting in regard to the electronics industry, and the many other potential applications that graphene makes feasible. These properties are due to graphene's band structure which has the conduction and valence bands touching at a point with a shape known as the Dirac cone. The linear slope of the bands causes the electrons within graphene to be massless and thus travel at the speed of light. This gives the high electron mobility and the low resistivity of  $10^{-6} \Omega \cdot cm$  which is lower than the most conductive metal (silver). [10] Carbon has the ability to crystalize itself into many various forms or "allotropes", all of which allow for different applications. One of these allotropes is graphene, and when graphene is stacked on top of one another by Van der Waals forces, it is known as graphite. Graphene can also be made into quantum dots (QD) and graphene nanoribbons (GNR) which are zero-dimensional (0D) and one-dimensional (1D) structures. Graphene in its typical 2D as well as its 1D and 0D forms have found uses in many areas. These include transistors, sensors, LED's and solar cell devices. [13-15] Other applications include water purification, as well as the sensing of specific contaminants in water. [16]

### 1.1.1 Physical Structure of Graphene

Carbon is the 6<sup>th</sup> element in the periodic table by atomic mass and the 4<sup>th</sup> most abundant element in the universe, making it relatively cheap and easy to mine. Carbon can be found in several isotopes  $^{12}C$ ,  $^{13}C$ , and  $^{14}C$  of which  $^{12}C$  is the most abundant and is also stable. [48] Carbon-14,

although rarer has found use in dating techniques. The ground state of  $^{12}\text{C}$  is  $1s^2 2s^2 2p^2$ . By promotion of electrons, carbon is able to maintain a crystalline structure. [48] When carbon is in the ground state, two electrons are available for chemical bonding. When an electron is promoted to the  $2p_z$  state, the carbon atom is able to covalently bond to a maximum of four other atoms (see Fig 1.1). It is carbon's ability to form four bonds which allows for the various carbon allotropes and thus graphene as well.

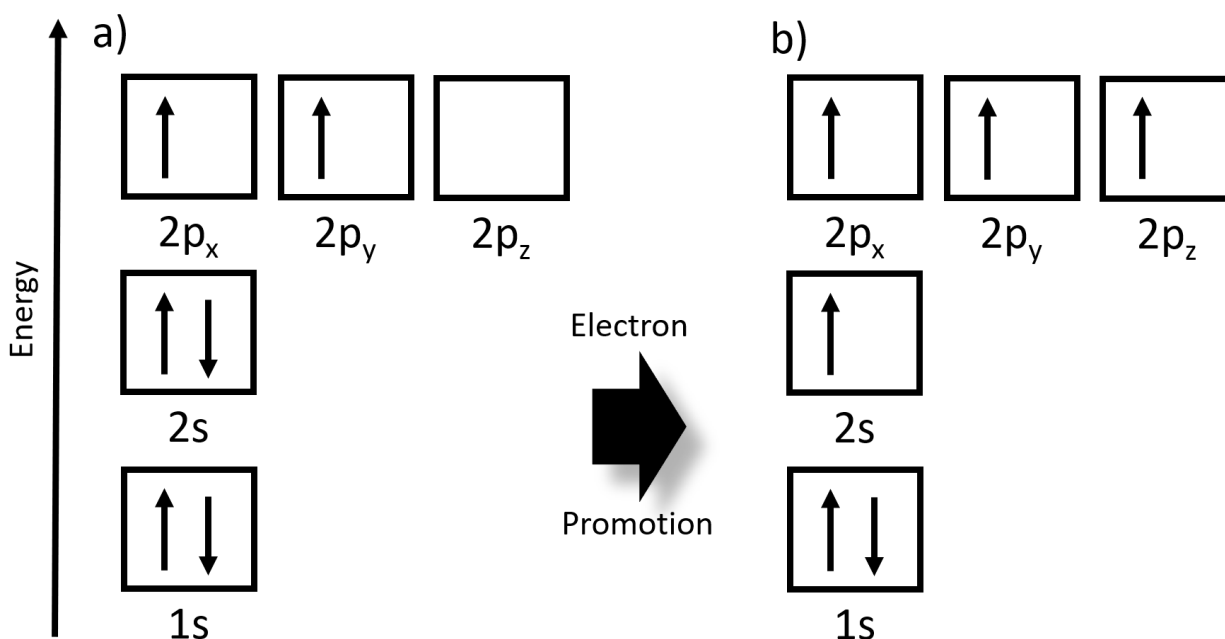


**Figure 1.1 a) Electron configuration of ground state of carbon b) Promotion of  $2s^2$  electron into the  $2p_z$  state**

Carbon also has the interesting ability to form many hybridizations due to the overlap in electron orbitals. The hybridization allows for the many allotropes of carbon (see Fig 1.2). These hybridizations are the  $sp^1$ ,  $sp^2$ , and lastly the  $sp^3$  hybridization. [17]

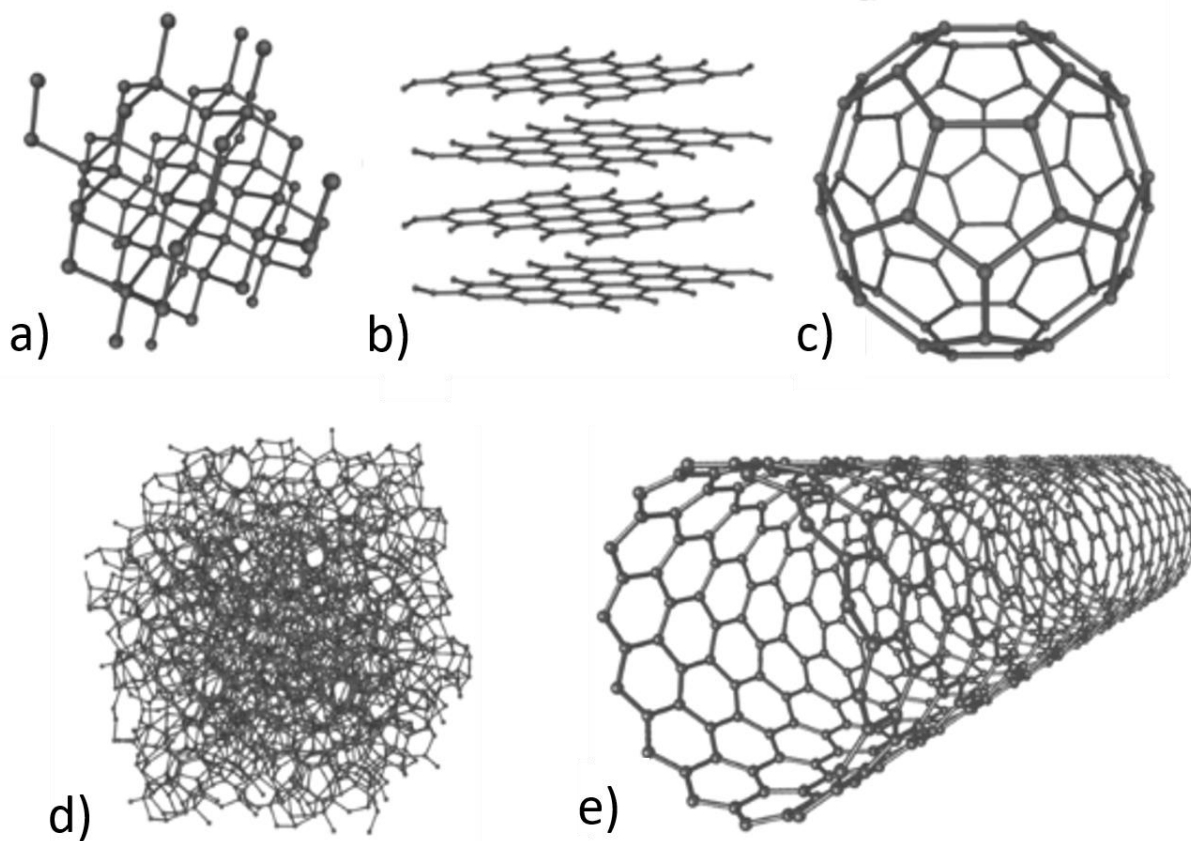


**Figure 1.2: Different allotropes of carbon a) diamond, b) graphite, c) C<sub>60</sub> fullerene (buckyball), d) amorphous carbon, e) carbon nanotube (CN). (This figure [46] is licensed under a Creative Commons Attribution 4.0 Unported License)**

These various allotropes allow carbon to be used in a variety of applications. Such as the interesting structure of diamond causing the material to be one of the hardest materials known to mankind, thus making it a prime candidate for drilling applications. Carbon nanotubes have also shown great promise for the field of bioimaging as a contrast agent for both photoacoustic tomography as well as thermoacoustic tomography. The crystal structure of graphene yields a particularly interesting band structure, which we will discuss in the upcoming section.

### 1.1.2 Electronic Structure of Graphene

The band structure of graphene can be theoretically determined by utilizing the Tight Binding Approximation (TBA). It can be shown that graphene is a zero-band gap semiconductor. The honeycomb lattice consists of  $sp^2$  bonded carbon atoms, where the bond lengths between adjacent carbon atoms is  $1.42 \text{ \AA}$ . The angle between the bonds is  $120^\circ$ , which forms the honeycomb structure. The band structure can be determined by considering the lattice structure, which is illustrated below.

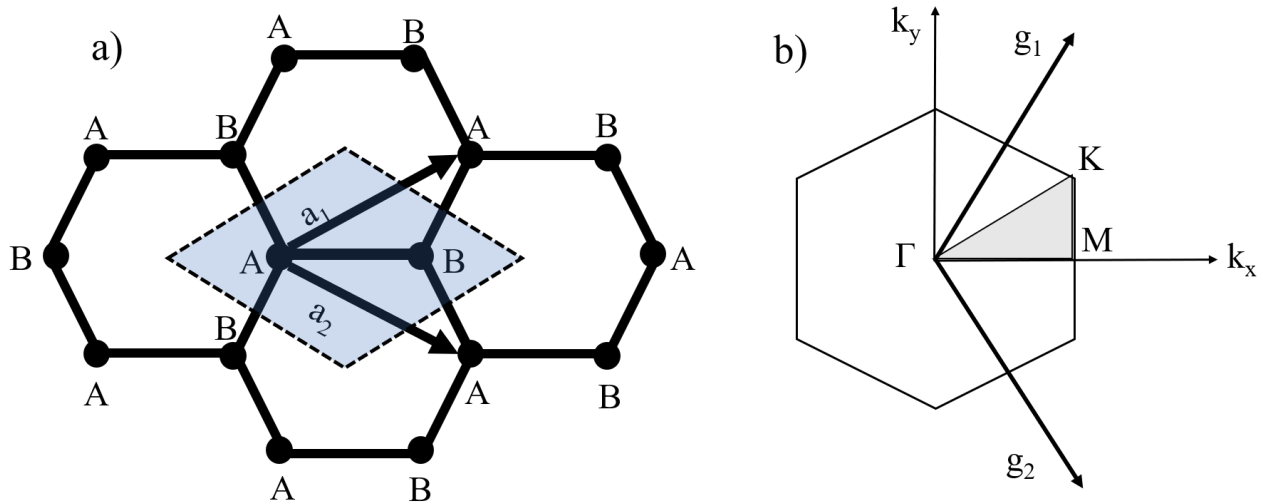


**Figure 1.3: a) Shows graphene's honeycomb structure, the unit cell (blue) is shown along with the diatomic basis labelled with A and B, primitive vectors are also shown as  $a_1$  and  $a_2$  b) shows the Brillouin zone with k-points shown (grey), the reciprocal lattice vectors are also shown and denoted as  $g_1$  and  $g_2$  [18,19] Reprinted with permission from the American Physical Society**

We can define the primitive vectors as the following.

$$a_1 = \frac{a}{2} (3, \sqrt{3}), \quad a_2 = \frac{a}{2} (3, -\sqrt{3}) \quad (1.1)$$

By using the lattice vectors, we can calculate the reciprocal lattice vectors using,  $a_i \cdot b_j = 2\pi\delta_{ij}$  then the reciprocal lattice vectors are derived as the following. [20]

$$b_1 = \frac{2\pi}{3a}(1, \sqrt{3}), b_2 = \frac{2\pi}{3a}(1, -\sqrt{3}) \quad (1.2)$$

The planes bisecting these vectors form the boundary of the (FBZ) first Brillouin zone (see Fig 1.3 b)). Wallace in his 1947 paper, first derived the theoretical energy dispersion relation. [19]

$$E_D = E_F \pm t \left\{ 1 + 4 \cos\left(\frac{3ak_x}{2}\right) \cos\left(\frac{ak_y}{2}\right) + 4 \cos\left(\frac{ak_y}{2}\right)^2 \right\}^{\frac{1}{2}} \quad (1.3)$$

$E_F$  is the fermi level of the material which is defined as the thermodynamic work used to add an electron to the material,  $a$  is the lattice constant. The variable  $t$  is the nearest neighbour hopping parameter which for graphene has a magnitude of approximately 1.8 eV, this value quantifies the energy needed for an electron to hop into neighbouring sites. [19] The sign of the hopping parameter is determined by the bonding and antibonding  $\pi$ -band. This can then be plotted around the K symmetry point; this point is also known as the ‘Dirac point’ and the shape of the energy dispersion relation is called the ‘Dirac cone’. The effective mass of the electrons within graphene is inversely proportionally to the curvature of energy dispersion relation. Because the slope of the energy dispersion in graphene at the Dirac point is infinite (non-smooth function), the effective mass of the electrons tends toward zero and thus become relativistic electrons.

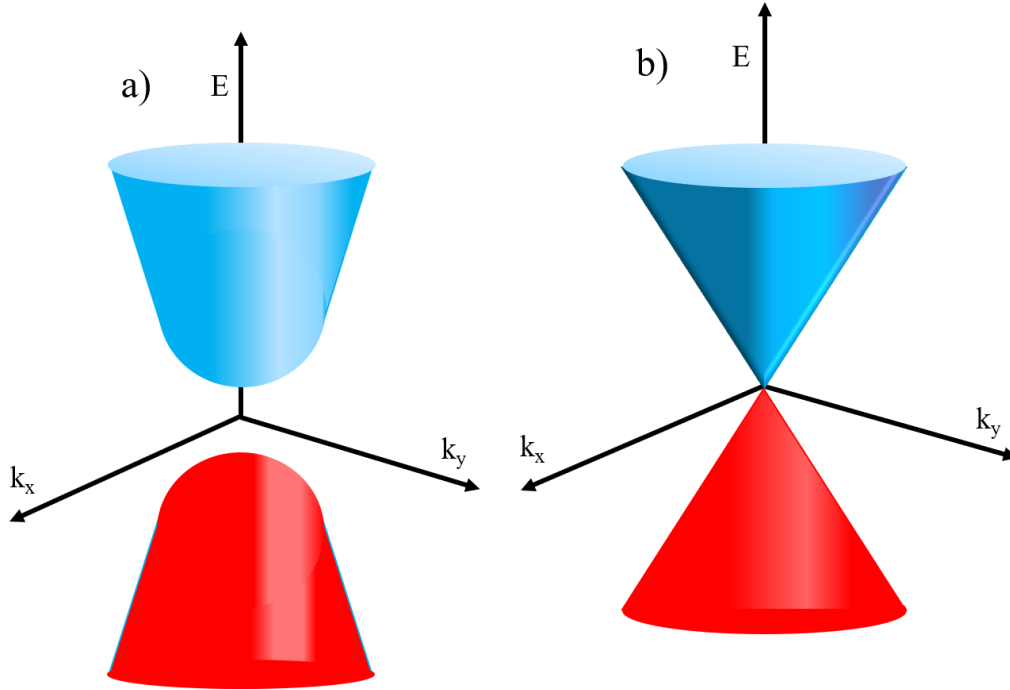


**Figure 1.4: Energy dispersion relation for a) typical semiconductor and b) graphene. Blue and red colors represent the conduction and valence bands respectively. (This figure from [18] and is reprinted with permission from the American Physical Society)**

Fig 1.4 shows the band structure of a typical semiconductor (left) and pristine graphene (right). The equation describing the shape of the band structure of graphene can be derived from equation 3) and is given in equation 4). [21]

$$\varepsilon(k) = \pm \hbar v_F |k| \quad (1.4)$$

This then yields an interesting relationship between the total particle energy and effective mass of the charge carriers. This can be done by considering the wave-particle duality of the charge carriers with their group and phase velocities as follows. [21]

$$\varepsilon = m^* v_g v_p \quad (1.5)$$

Because, the conduction and valence bands touch at the Dirac point, graphene is considered a zero band-gap semiconductor or a 'semimetal' material. It is these electronic properties that this thesis is attempting to exploit for the filtration and detection of heavy metal ions. However, there are a host of post graphene materials, one of particular interest is molybdenum disulfide.

## 1.2 Molybdenum Disulfide

After the flurry of research in graphene in the early 2000's from the mechanical exfoliation of graphene at the University of Manchester by Geim and Novoselov, researchers began searching for new 2D materials. One such materials is molybdenum disulfide ( $\text{MoS}_2$ ), which is a semiconductor with the ability to easily be exfoliated into 2D form. Due to the low friction coefficient values of less than 0.1,  $\text{MoS}_2$  is often used as a dry lubricant, especially when particle sizes are 1-100  $\mu\text{m}$ . [23] Due to this, it is often used as lubricants in two-stroke engines, ski waxes, and even bullets. [24-26] When added to plastics,  $\text{MoS}_2$  forms composite materials which are ubiquitous throughout the modern world and are found in materials such as Vespel<sup>®</sup> (Polyimide), Teflon<sup>™</sup> (polytetrafluoroethene), and Nylon 66 (polyamide 6,6). [27] Due to its electronic structure,  $\text{MoS}_2$  has found enormous use in the field of electronics.  $\text{MoS}_2$  nanoflakes have been used as multi-layered memristive and memcapacitive devices by utilizing a solution-processed fabrication which allows for flexible memory devices. [28,29]  $\text{MoS}_2$  has also been utilized in field-effect transistor (FET) biosensors, due to its nonzero band gap (unlike graphene) which allows for greater sensitivity. This is because the zero bandgap of graphene will allow for current leakage across the 3 terminals. [30] Additionally, two dimensional  $\text{MoS}_2$  has even been shown to be successful in creating a microprocessor. [31] Furthermore, researchers at Berkley's National Lab (Materials Science Division) created the smallest transistor to date using  $\text{MoS}_2$ . The design has a bilayer of 2D  $\text{MoS}_2$  which act as the active layer and a 1 nm carbon nanorod

(NR) embedded in a layer of Zirconium dioxide which act as the gate and insulating layers respectively. [32] This 1 nm transistor has gone far beyond what was previously thought possible and may assist in the continuation of the so-called “Moore’s Law”.

### 1.2.1 Physical Structure of MoS<sub>2</sub>

From the top down, MoS<sub>2</sub> has a very similar structure to that of graphene, both having a honeycomb structure. However, the sulfur atoms extend in opposite directions along the c-axis. MoS<sub>2</sub> is known to have two crystalline phases, 2H-MoS<sub>2</sub> and 3R-MoS<sub>2</sub> which represent hexagonal and rhombohedral symmetry respectively. [33] In both cases the molybdenum atoms are placed in the center of a trigonal prismatic coordination sphere and are semiconducting. [33] There is also a third metastable crystalline phase of MoS<sub>2</sub> which is created by intercalating Li ions between layers.

MoS<sub>2</sub> has a three-atom basis, one for molybdenum and two for each sulfur. The two Bravais lattice primitive vectors are given as follows. [34]

$$R_1 = \frac{a}{2}(3, \sqrt{3}) , \quad R_2 = \frac{a}{2}(3, -\sqrt{3}) \quad (1.6)$$

The lattice constant is  $a = 3.42 \text{ \AA}$ , where the sulfur atoms  $1.56 \text{ \AA}$  above and below the XY-plane. The length of the Mo-S bonds is  $2.40 \text{ \AA}$ . [34]

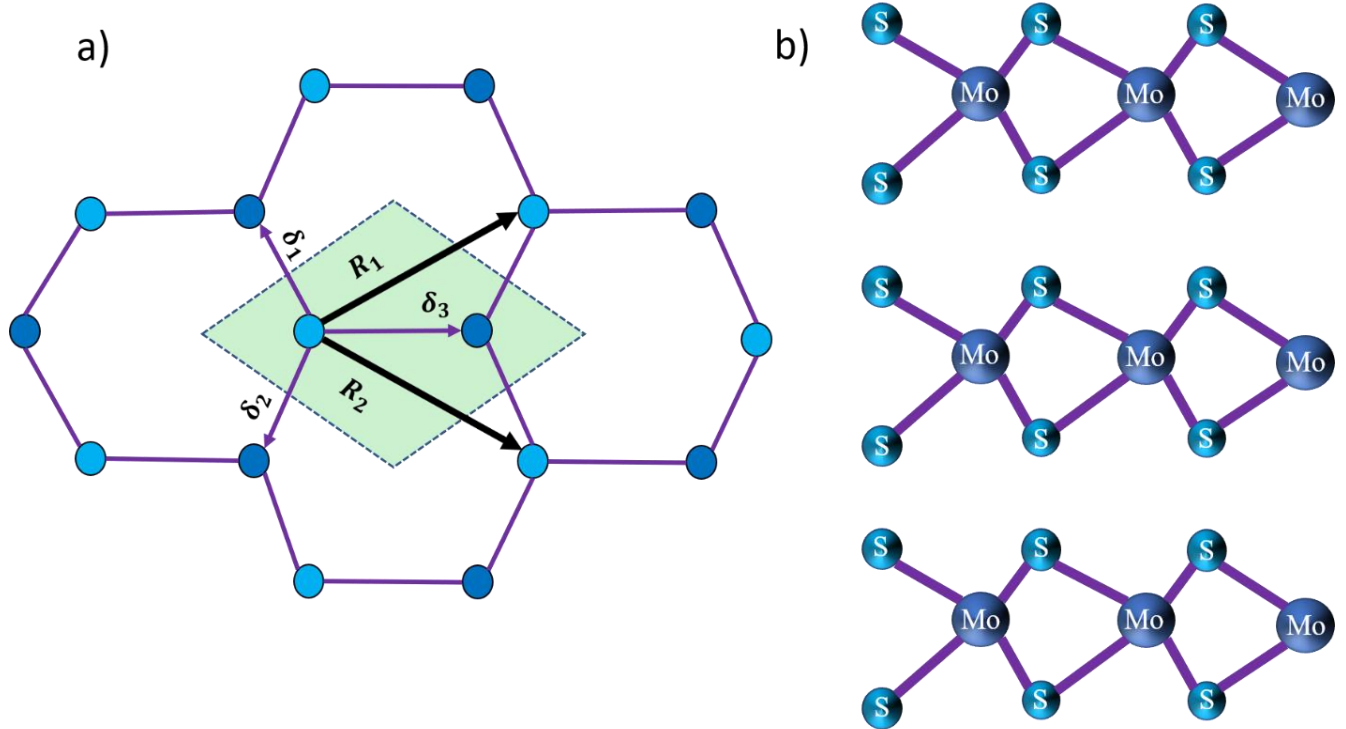


**Figure 1.5: a) Honeycomb structure of MoS<sub>2</sub> with unit cell (green), b) sides view of MoS<sub>2</sub> multilayer structure showing Mo (dark blue) and S (light blue)**

### 1.2.2 Electronic Structure of MoS<sub>2</sub>

Similar to graphene, the Brillouin zone (BZ) is hexagonal and the important symmetry points and lines are given as follows. [34]

$$\Gamma = (0,0), K = \left(\frac{2\pi}{3a}, -\frac{2\pi}{\sqrt{3}a}\right), M = \left(\frac{\pi}{a}, -\frac{\pi}{\sqrt{3}a}\right) \quad (1.7)$$

The reciprocal lattice basis vectors are given as follows. [34]

$$K_1 = \frac{4\pi}{\sqrt{3}a} \left(\frac{\sqrt{3}}{2}, -\frac{1}{2}, 0\right), K_2 = \frac{4\pi}{\sqrt{3}a} (0, 1, 0) \quad (1.8)$$

The first Brillouin zone (FBZ), is illustrated below. The FBZ of MoS<sub>2</sub> is noticeably different from that of graphene, this is due to the corrugated structure of the Mo and S bonding, meaning

that although the primitive lattice vectors are equivalent, the basis is triatomic, whereas graphene has a diatomic basis causing a different BZ.

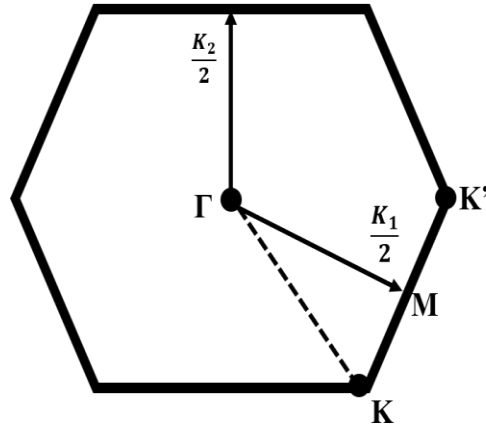


**Figure 1.6: First Brillouin zone of MoS<sub>2</sub> showing the reciprocal lattice vectors  $K_1$  and  $K_2$ , as well as high symmetry points  $\Gamma$ ,  $K$ ,  $K'$ ,  $M$ . (This figure [27] is licenced under the CC BY-NC-ND 3.0 licence)**

Thus, theoretical calculations can be done to approximate the band structure of monolayer as well as bulk MoS<sub>2</sub>, this is often done with density functional theory (DFT) simulations.

Monolayer MoS<sub>2</sub> has a direct bandgap of about 1.81 eV, bulk MoS<sub>2</sub> has an indirect bandgap of 1.29 eV. [35] Because MoS<sub>2</sub> is a semiconductor, the conductivity of the material can be easily measured, this can be utilized for a variety of applications including (and notably for this thesis) the detection of heavy metals in water, by measuring material resistivity.

### 1.3 Application of 2D materials for water purification and sensing of cadmium

Due to the growing population globally, a need for readily available clean drinking water is of vital importance. This becomes exponentiated by the substantial growth of the electronics industry. Many current electronic devices utilize heavy metals for many applications, such as

touch screens, rechargeable batteries, switches etc. Due to the industrial applications of these heavy metals which include mercury, lead, cadmium etc. trace amounts of these toxic elements contaminate water supplies and ecologies. Thus, it is also vitally important to be able to monitor the levels of these heavy metals.

Cadmium has been in industrial use for several decades. Cadmium has found use in NiCd rechargeable batteries, CdSe luminescent quantum dots, control rods in nuclear reactors, anticorrosive agents, as well as pigments. [36-40] Phosphate fertilizers are also known to cause large cadmium loads which, due to water run off, contaminates the water supply. Additionally, cadmium is often found in ores along with zinc, copper, and lead. Volcanic activity often exposes these ores to water supplies, temporarily increasing the concentration of cadmium in a natural way. [41] The concern for these contaminants comes from harmful health effects these heavy metals often cause on populations. These include but are not limited to, bone demineralization, severe kidney damage, lung damage, as well as brain damage in children due to the high permeability of the blood brain barrier in childhood. [42-43] This has led to the Environmental Protection Agency (EPA) placing a minimum permissible limit of 5 parts per billion (PPB) on cadmium divalent cations in water. Thus, it is of the utmost importance that methods of filtering and monitoring cadmium become ubiquitous.

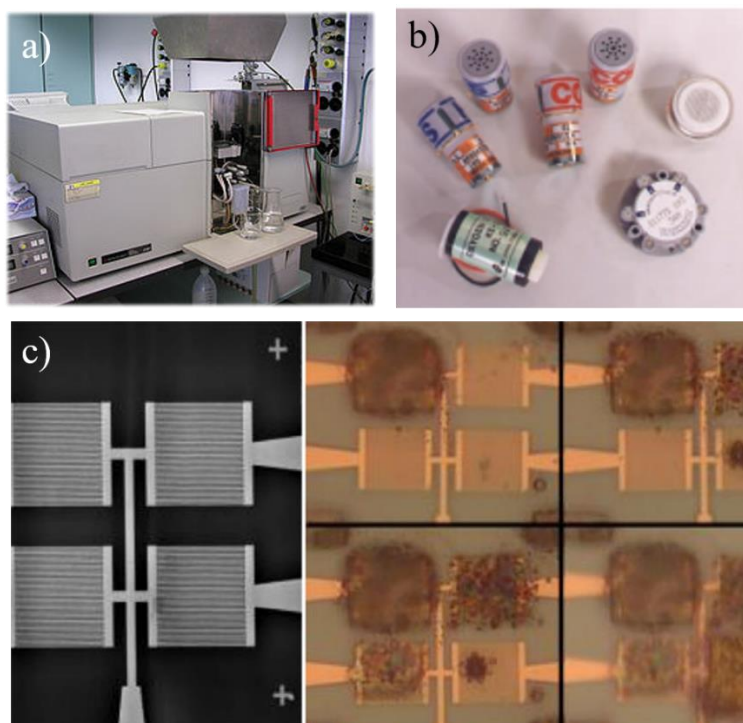


**Figure 1.7: Images of some current cadmium detection methods a) atomic emission spectroscope, b) electrochemical cells, and c) thiolated gold nanoparticle based chemiresistors (Lurie Nanofabrication Facility, University of Michigan)**

Currently, there are a variety of methods to detect trace amounts of cadmium and other heavy metals in water. These include atomic emission spectroscopy which uses the intensity of light at particular wavelengths to retrieve spectra from which elements can be identified. Also, electrochemical cells are fairly simple devices with the ability to cause a chemical reaction by using electricity, or conversely, uses a chemical reaction to generate electricity, such as a Galvanic cell. However, both of these techniques come with several drawbacks. These techniques are expensive and in need of on-site trained personnel in order to take measurements, making real-time monitoring impossible. Additionally, chemiresistor methods are being developed which include thiolated gold nanoparticles (NP) [44,47]. These techniques do provide

solutions to some of the problems that occur in the previously mentioned methods. However, these techniques still utilize expensive metals such as gold.

Another issue with many detection methods, is their inability to work in an in-line architecture. This type of architecture allows for filtration and sensing to be done in parallel. Whereas, devices operating off-line require the user to take the sample away from the source to the device in order to run the required tests. This however can be improved by utilizing a vacuum filtration setup. The goal of this thesis is to develop methods and devices to both selectively detect and filter cadmium contaminants in water.

### 1.3.1 Water filtration and purification techniques

Currently, in the field of water filtration, reverse osmosis (RO) is reigning king. The quality of filtration done by this process is nearly untouchable. However, it suffers from a major drawback, which is its relatively large energy consumption. Thus, vacuum filtration methods have grown in popularity. Reverse osmosis allows permeability of particles  $< 0.1$  nm and requires differential pressures of about 4200 kPa. [45] Whereas, nanofiltration has a pore size in the range of 0.1 nm to  $< 1$  nm and requires a differential pressure of about 1200 kPa. [45] Additionally, nanofiltration (and greater than nanoscale) has the benefit of being able to perform in dead-end as well as cross flow architectures. The differences in the architectures are highlighted in Fig 1.8.

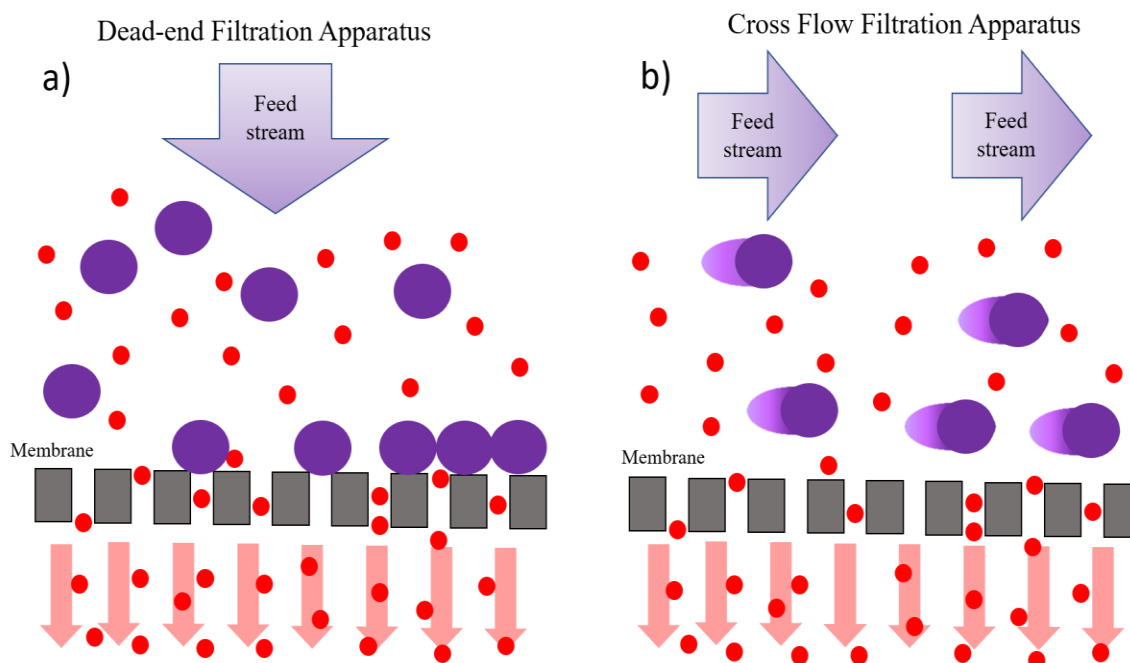


**Figure 1.8: Comparison between two filtration architectures a) shows a water filtration apparatus operating in a dead-end design b) shows a cross flow architecture**

Although, the dead-end filtration architecture is beneficial for the ease of manufacturing as well as rapid prototyping, it does however, often suffer from fouling which impacts the performance of filtration and decreases the lifetime of the filter. However, the cross-flow architecture has improved filter life time. We utilize the dead-end filtration architectures due to the ease of prototyping and the low energy required for this device to operate effectively. Most importantly, the low cost of manufacturing of these devices allows for interesting possibilities, such as having this device in homes or monitoring protected ecological zones. This thesis is composed of the results from two papers which address the aforementioned issues.

## 1.4 Thesis Overview

Chapter 3 is an article published in *FlatChem*. This article showed the development of a novel chemiresistor based apparatus for the selective detection of cadmium divalent cations at low

concentration in water. The method utilizes graphite which has been exfoliated into multilayer graphene (MLG). The exfoliation process used a widely available surfactant, poly(ethylene-glycol)-*block*-poly(propylene-glycol)-*block*-poly(ethylene-glycol) (PEG-PPG-PEG) by solution processing. This material was then used in the filtration device. Both synthetic turbostratic graphite and natural hydrothermal vein graphite were exfoliated and characterized to test for optimal affinity to PEG-PPG-PEG. Resulting multilayer graphene samples were characterized using X-Ray diffraction (XRD) to determine the interlayer spacing. Raman spectroscopy, scanning electron microscopy (SEM), and electron paramagnetic resonance (EPR) were used to test for defect density of MLG samples.

Chapter 4 is also an article published in *FlatChem*. We sought to provide a technique of filtration of cadmium divalent cations in water by the means of L-Cysteine functionalized molybdenum disulfide. L-Cysteine has been shown to have a strong affinity towards heavy metal ions. Cd as well as Fe and Mn (as controls) solutions were vacuum filtered, where comparisons can be made between before and after filtration. Electron paramagnetic resonance was done in order test concentrations of metal ions.

## References

- [1] H. P. Boehm, A. Clauss, G. O. Fischer, U. Hofmann, Z. Dünnsche Kohlenstoff-Folien, *Naturforsch. B.*, **1962**, 17:150-153
- [2] K. Novoselov, A. Geim, S. Morozov, D. Jiang, Y. Zhang, S. Dubonos, I. Grigorieva, A. Firsov, *Science*, **2004**, 306:666-669
- [3] C. Lee, X. Wei, J. W. Kysar and J. Hone, *Science*, **2008**, 321, 385-388
- [4] A. H. C. Neto, F. Guinea, N. M. R. Peres, K. S. Novoselov and A. K. Geim, *Reviews of Modern Physics*, **2009**, 81, 109- 162
- [5] A. Balandin, S. Ghosh, W. Bao, I. Calizo, D. Teweldebrhan, F. Miao, and C. N. Lau, *Nano Letters* **2008** 8 (3), 902-907
- [6] D. E. Sheehy, and J. Schmalian, **2009**, *Phys. Rev. B*, 80, 193411
- [7] F. Bonaccorso, L. Colombo, G. Yu, M. Stoller, V. Tozzini, A.C. Ferrari, R.S. Ruoff, V. Pellegrini, *Science*, **2015**, 347, 1246501
- [8] A. Balandin, S. Ghosh, W. Bao, I. Calizo, D. Teweldebrhan, F. Miao, N. Chun, *NanoLetters ASAP*, **2008**, 8, 902907
- [9] C. Faugeras, B. Blaise, M. Orlita, M. Putemski, R. Rahul, A.K. Geim, *ACS Nano*, **2010**, 4, 1889-1892
- [10] A. K. Geim, K. S. Novoselov, *Nature Materials*, **2007**, 6, 183-191
- [11] X. Li, X. Wang, L. Zhang, S. Lee and H. Dai, *Science*, **2008**, 319, 1229-1232, 2

- [12] Y. Wang and A. Hu, *Journal of Materials Chemistry C*, **2014**, 2, 6921, 6
- [13] G. Eda, A. Nathan, P. Wöbkenberg, F. Colleaux, K. Ghaffarzadeh, T. D. Anthopoulos, M. Chhowalla, *App. Phys. Lett.*, **2013**, 102, 133108
- [14] C. X. Guo, H. B. Yang, Z. M. Sheng, Z. S. Lu, Q. L. Song, C. M. Li, *Angew. Chem. Int. Ed.* **49**, **2010**, 3014 – 3017
- [15] J. T. Robinson, F. K. Perkins, E. S. Snow, Z. Wei, P. E. Sheehan, *Nano Lett.*, **2008**, 8, 3137-3140, 2008.
- [16] Han, Y., Xu, Z. and Gao, C., *Adv. Funct. Mater.*, **2013**, 23, 3693-3700.
- [17] J. McMurray, *Prentice Hall. P.* 1995, 272, 978-0-131-40221-8
- [18] A. H. Castro Neto, F. Guinea, N. M. R. Peres, K. S. Novoselov, A. K. Geim, *Rev. Mod. Phys.*, **2009**, 81, 109-162
- [19] P. R. Wallace, *Phys. Rev.*, **1947**, 71, 622-634
- [20] Geim et al., *Nature Materials*, **2007**, 6, 183
- [21] V. Ariel, *arXiv*, **2012**, 3995, 1205
- [22] M. Han, S. Zhigang, B. Shuang, *Journal of Colloid and Interface Science*, **2018**, 517, 204-212
- [23] F.L. Claus, *Academic Press: New York*, **1972**
- [24] L, Karlöf, L. T. Axell, *Swix Sport AX*, **2011**
- [25] C. Larsson, *Norma*, **2009**

- [26] E.R. Braithwaite, A.B. Greene, B.M. Train, *Industrial Lubrication and Tribology*, **1999**, 51, 274-286, 6
- [27] R. Bissessur, J. L. Schindler, C. R. Kannewurf and M. Kanatzidis, Section A. *Molecular Crystals and Liquid Crystals*, **1994**, 245, 249-254, 1
- [28] R. Xu, H. Jang, M-H. Lee, D. Amanov, Y. Cho, H. Kim, S. Park, H-J Shin, and D. Ham, *Nano Lett.*, **2019**, 2411-2417
- [29] A. K. Khan, B. H. Lee, *AIP Advances*, **2016**, 6, 095022
- [30] D. Sarkar, W. Liu, X. Xie, A. C. Anselmo, S. Mitragotri, and K. Banerjee, *ACS Nano.*, **2014**, 3992-4003
- [31] S. Wachter, D. K. Polyushkin, O. Bethge, T. Mueller, *Nature Communications*, **2017**, 8, 14948
- [32] S. B. Desai, S. R. Madhvapathy, A. B. Sachid, J. P. Lilnas, Q. Wang, G. H. Ahn, G. Piltner, M. J. Kim, J. Bokor, C. Hu, H. P. Wong, A. Javey, *Science*, **2016**, 354, 99-102
- [33] M-H. Wu, L. Li, N. Liu, D-J. Wang, Y-C. Xue, L. Tang, *Process Safety and Environmental Protection*, **2018**, 118, 40-58
- [34] E. Ridolfi et al, *J.Phys.: Condensed Matt.*, **2015**, 27, 365501
- [35] K. F. Mak, C. Lee, J. Hone, J. Shan, and T. F. Heinz, *Phys Rev Lett.*, **2010**, 105, 136805
- [36] B. R. Bowsher, R. A. Jenkins, A. L. Nichols, N. A. Rowe, J. a. H. Simpson, *UKAEA Atomic Energy Establishment*, **1986**
- [37] T. L. Roberts, *Procedia Engineering*, **2014**, 83, 52-59

- [38] A. Cesaratto, C. D'Andrea, A. Nevin, G. Valentini, F. Tassone, R. Alberti, T. Frizzi, and D. Comelli, *Anal. Methods*, **2014**, 6, 130-138
- [39] D. Mo, L. Hu, G. Zeng, G. Chen, J. Wan, Z. Yu, Z. Huang, K. He, C. Zhang, M. Cheng, *Appl Microbiol Biotechnol.*, **2017**, 107, 2713-2733
- [40] F. Putois, *Journal of Power Sources*, **1995**, 57, 67-70, 1-2
- [41] M. Hutton, *Ecotoxicol Environ Saf.*, **1983**, 9-24, 1
- [42] L. Järup, *British medical bulletin.*, **2003**, 68, 167-182
- [43] A. Bernard, *Indian J. Med. Res.*, **2008**, 128, 557
- [44] B. Raguse, E. Chow, C. S. Barton, L. Wiczorek, *Anal. Chem.*, **2007**, 7919, 7333-7339
- [45] A. Aghigh, V. Alizadeh, H. Y. Wong, M. S. Islam, N. Amin and M. Zaman, *Desalination*, **2015**, 365, 389-397, 6
- [46] V. Mott, "Introduction to Chemistry: Allotropes of Carbon", *Lumen*,
- [47] E. Covington, F. I. Bohrer, C. Xu, E. T. Zellers and Ç. Kurdak, *Lab Chip*, **2010**, 10, 3058
- [48] J. Meija, *Pure and Applied Chemistry*, **2013**, 88, 265-91, 3

## Chapter 2

### 2 Introduction

In this thesis, we propose two novel methods of filtering and sensing heavy metal divalent cations in water. This was accomplished by: (1) utilizing the tunable interlayer spacing of exfoliated graphite to trap the metal ions, which subsequently alters the conductivity of the material, allowing for detection by a chemiresistor architecture and, (2) functionalizing MoS<sub>2</sub> with L-cysteine, which due to the ideal crystalline size of MoS<sub>2</sub> as well as the coordination number of the thiol group of cysteine, allows for a high affinity to heavy metal divalent cations. In order to verify, the effect of alterations to multi layer graphene's interlayer spacing found in chapter 3, X-ray diffraction (XRD) was used. The effect of defects within the multilayer graphene to sensing performance, was investigated through a combination of Scanning Electron Microscopy (SEM), Electron Paramagnetic Resonance (EPR), and Raman Spectroscopy. In chapter 4, a wide variety of characterization techniques were used, most notably for this thesis (the authors work) is Atomic Force Microscopy, was utilized to image MoS<sub>2</sub> flakes to gain further understanding of the effect that functionalization has on the structure of the material. All previously mentioned characterization techniques are explained in detail in this chapter.

#### 2.1 Thermal Evaporation

Thermal evaporation is a technique often used to deposit thin films. In comparison to similar techniques, including but not limited to, electron beam physical vapor deposition, RF sputtering, etc., thermal evaporation allows for low energy and high purity in evaporating metals with high vaporization points. Additionally, because film uniformity is not of utmost concern for our

purposes, other methods which yield more uniform films are not required. The technique heats some material (often metals) above its vaporization point. The material is able to be deposited in a controllable and adequately uniform manner. The technique requires the sample and evaporate material to be positioned inside of a chamber which is held in “ultra” high vacuum (UHV) where pressures are  $< 10^{-7}$  pa. [1] This not only lowers the vaporization point of the material, but also decreases contamination and allows for a highly pure film. Due to the very high melting point of tungsten (W), which is about  $3,422^{\circ}\text{C}$ , tungsten is used as the material for the basket heaters in the device. [2]

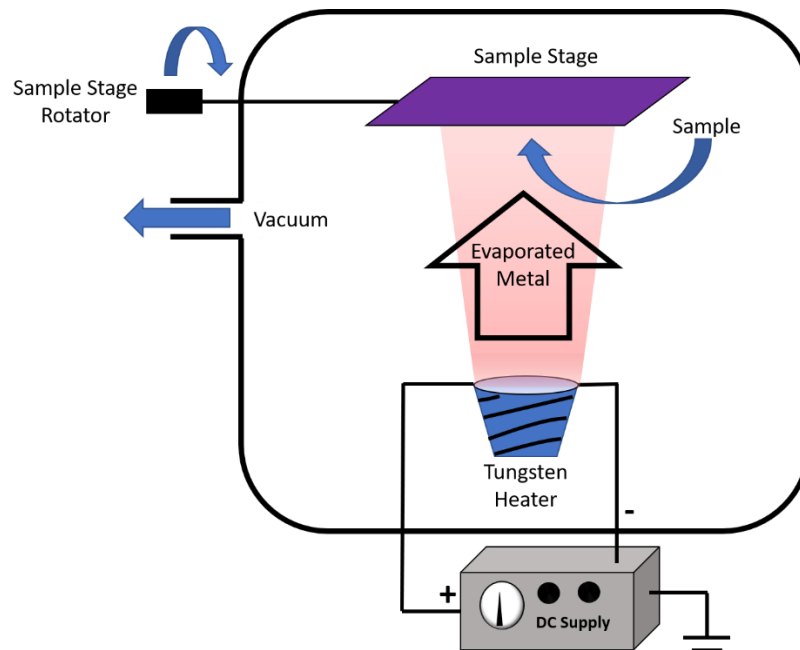


**Figure 2.1: Thermal evaporation setup**

Although, thermal evaporation can be used to evaporate many materials, for the purposes of this thesis, the metal aluminum (Al) was utilized for its low cost and high conductivity. In order for the vacuum chamber to reach the needed low pressures, two pumps are required. The first, is a

roughing pump which is the initial pump and gets the chamber to a low enough pressure for a diffusion pump to take over.

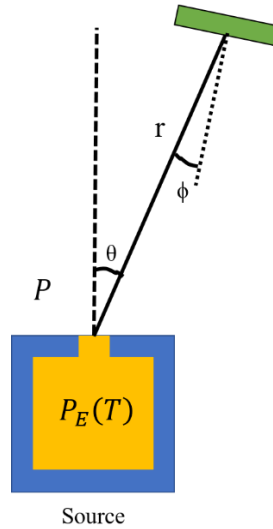


**Figure 2.2: Typical evaporation setup from which the Langmuire-Knudsen relation (Eq. 2.1) is derived**

$$R_m = C_m \sqrt{\left(\frac{M}{T}\right)} \cos(\theta) \cos(\phi) \frac{\{P_E(T) - P\}}{r^2} \quad (2.1)$$

Where  $R_m$  is the mass deposition rate,  $C_m = 1.85 \times 10^{-2}$ ,  $M$  is the evaporant molecular-mass (g),  $T$  is the sources temperature,  $P$  is the pressure of vacuum (torr),  $P_E(T)$  is the pressure of the source, lastly  $r$  is the distance between the source and sample (cm). The diffusion pump maintains the extremely low pressures in the UHV. The need for UHV has two purposes: (1) to maintain low impurities in evaporate material, and (2) to maximize the mass rate of deposition as demonstrated by the Langmuire-Knudsen relation (Eq 2.1).

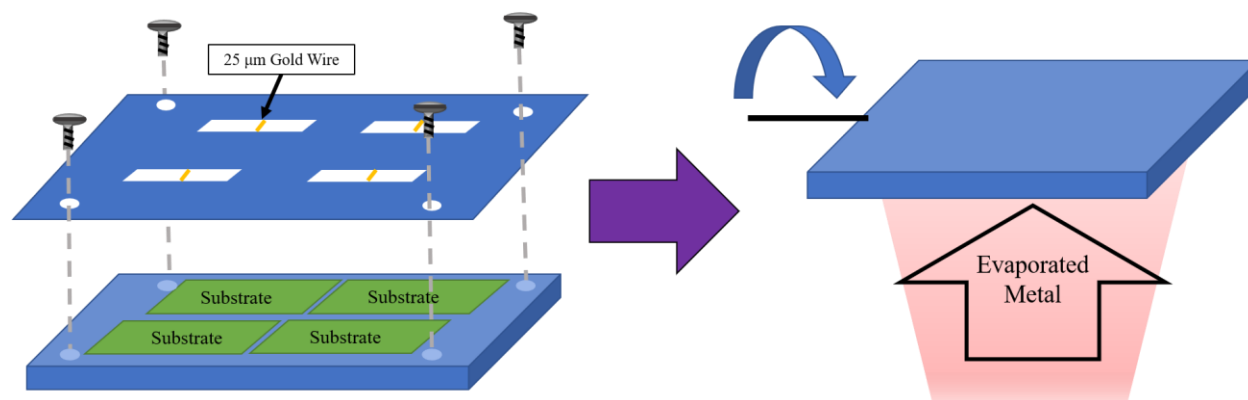


**Figure 2.3: Illustration of shadow masking technique used to pattern a 25  $\mu\text{m}$  gap between aluminum electrodes**

In order to create a small gap between electrodes we employed the shadow masking technique of micro patterning (see fig 2.3). The space left between aluminum electrodes is referred to as the gap cell. For this thesis, aluminum was evaporated onto a microporous polymer support. The material of interest (MLG or  $\text{MoS}_2$ ) will be vacuum filtered onto the Al contact containing support. With the dimensions of the gap cell known the resistivity of material contained in the gap cell is easily determined.

## 2.2 Raman Spectroscopy

Raman spectroscopy has become one of the most widely utilized and ideal surface characterization techniques. High-quality spectrometers are available commercially, allowing many laboratories to gain access to the technique. It is especially useful for characterizing the defectiveness of graphene, fullerenes and nanotubes. [34] The technique utilizes monochromatic light usually from a laser source, which results in low energy excitation of vibrational modes by phonon scattering. [3,5,6] The light source usually operates from the near infrared, through the visible, and into the near ultraviolet (100 – 1000 nm). [4]

A molecule or material with no Raman-active modes will absorb a photon with a frequency  $\nu_0$ , the molecule will then reemit the photon with the same frequency as the photon that was absorbed and return to its original vibration/rotational state. This type of elastic scattering is known as Rayleigh scattering which is also the most probable. The second scattering occurs when an incident photon is absorbed into a molecule or material which has Raman active modes, with a frequency  $\nu_0$ . Some of the energy from the photon is transferred to the Raman active modes of the material with a frequency  $\nu_R$ . The material then emits a photon with a frequency of  $\nu_0 - \nu_R$ . In this case the Raman frequency is called the Stokes frequency and this type of scattering is known as Stokes scattering. [7-9] The third and final type of scattering happens when a photon is absorbed by a material with Raman active modes with a frequency of  $\nu_0$  much like the aforementioned. However, this material may already be in an excited vibrational state  $\nu_R$ . This causes an excessive energy of the Raman active mode. Thus, a photon will be released with a higher frequency than the incident photon. This emitted frequency is  $\nu_0 + \nu_R$ . [7-9] These scattering processes are shown in fig 2.4.

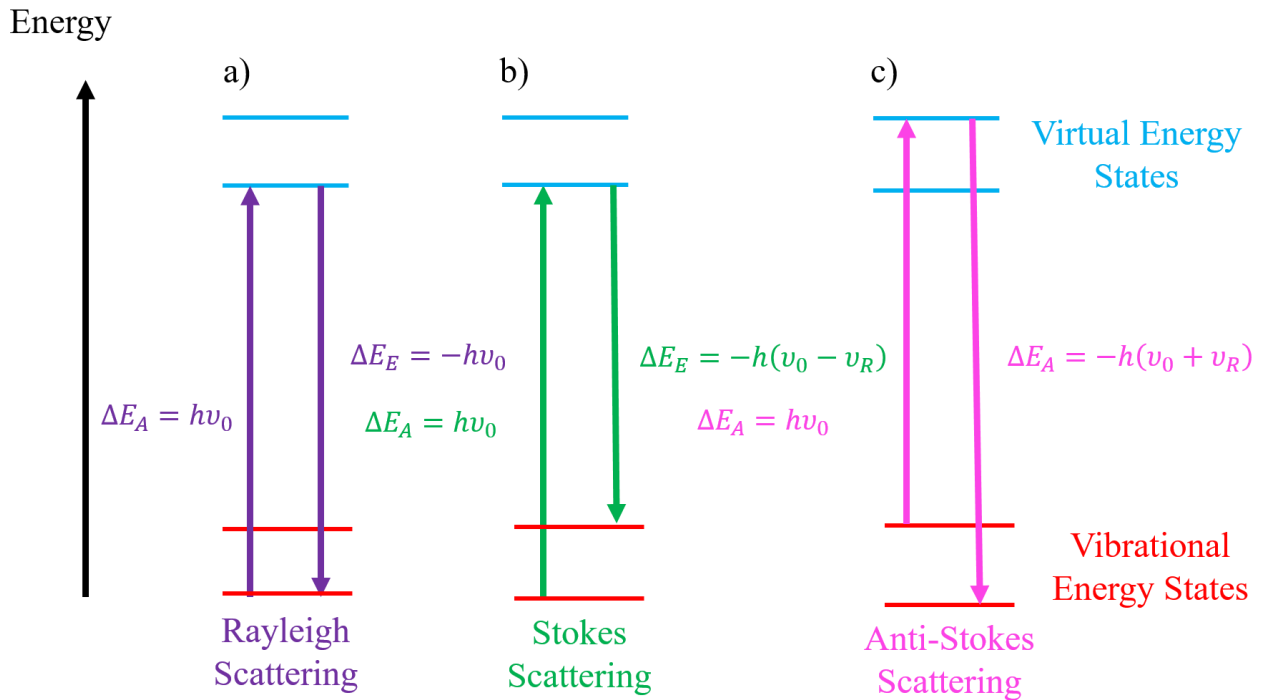


**Figure 2.4: A comparison of various Raman scattering processes. a) shows the process of Rayleigh scattering, where the energy of the absorbed and emitted photons are equal, b) shows Stokes scattering where a photon is absorbed and the Raman active mode takes some energy and emits a photon with less energy, c) shows the anti-Stokes scattering where a photon is absorbed in a material which already has excited vibrational modes, the emitted photon has the same energy as the vibrational mode plus the absorbed photon [10]**

A typical Raman spectrometer has an architecture which is shown in fig 2.5. Where a monochromatic light source irradiates the sample. Reemitted light is directed back towards the spectrograph where Rayleigh scattered light (same frequency as source) is filtered.

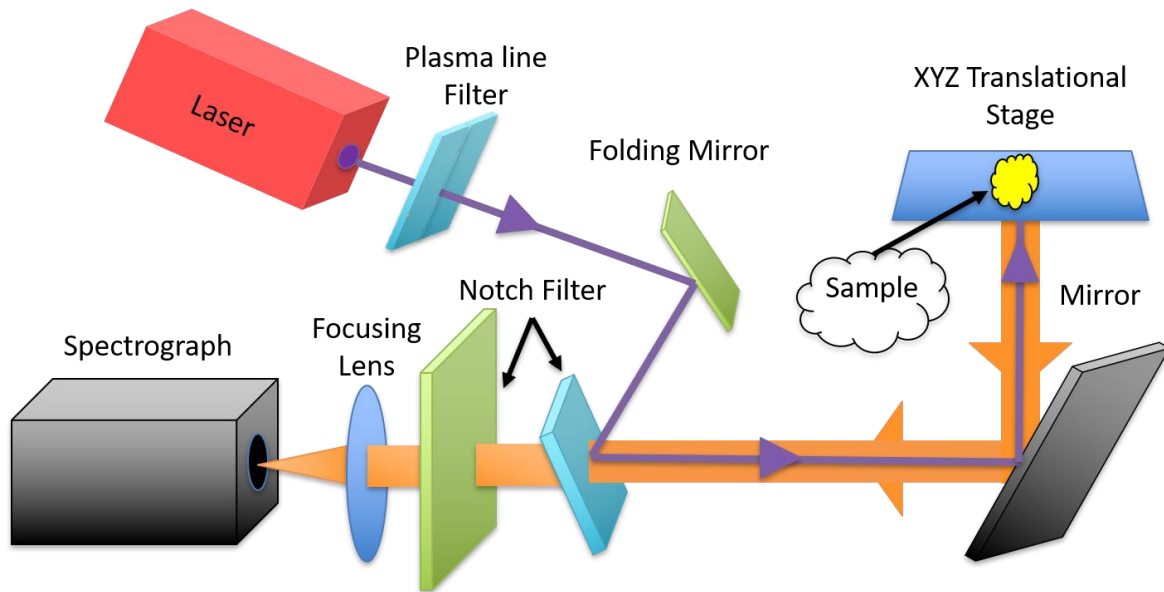


**Figure 2.5: Diagram of Raman spectrometer where light interacts with sample, and Raman shifted light is emitted from sample and directed into spectrograph**

The laser sweeps through a range of wavelengths creating the horizontal axis for the spectra. Elastically scattered (Rayleigh) radiation is filtered by the notch filters in the apparatus. The light is then collected and focused into the spectrograph by a collecting lens. The spectrometer is then able to measure a frequency shift between the observed light and that of initial beam. There is a proportionality between the number of scattered photons at a given frequency and number of vibrational states of a given phonon dispersion mode.

### 2.2.1 Raman of graphene and $sp^2$ carbon materials

Single layer graphene has two Raman active modes: The D-peak and the G-peak. In order to gain insight into these modes, we must consider which modes are Raman active according to the phonon-dispersion relation. Only modes or vibrational states which are anisotropically (directional) polarizable are Raman active. A dipole moment may be induced by interacting light (electromagnetic radiation), this dipole may either scatter or emit light at equivalent frequency to

the (optical) electromagnetic wave which induced the dipole. If, however the material is isotropically (non-directional) polarizable, the phonon mode and the incident electromagnetic wave oscillate at the same frequency, in that case Rayleigh scattering occurs. Vibrations may cause changes in polarizability, causing inelastic scattering of the incident light, and thus a measurable Raman shift which appears as spectral peaks.

The two-atom unit cell of graphene (fig 1.3 a) results in 6 phonon dispersion branches, which may be optical (3 branches) or acoustic (3 branches). [33] The acoustic branches yield Brillouin scattering, whereas the optical branches yield Raman scattering. The phonon dispersion branches also differentiate if the vibrations are in-plane (i) or out-of-plane (o) to the graphene layer, as well as if the vibrations are transverse (T) or longitudinal (L) in relation to atoms within the unit cell. [33] The six phonon dispersion curves of graphene are given the following labels, LO, iTO, oTO, LA, iTA, and oTA. The modes which are associated with the G-peak are the iTO, and LO modes (both of which are optical). [11,13,14] The D-peak originates from second order processes, the D-peak results from one iTO phonon interacting with a defect. Thus, the G and D peak loosely correspond to the frequency of the optical transverse frequency at the zone center and boundary. The 2D-peak also originates from the second order process where the interaction between two iTO phonons and is always permitted. The D-peak is due to the breathing modes of the six carbon rings which requires a defect to be present.

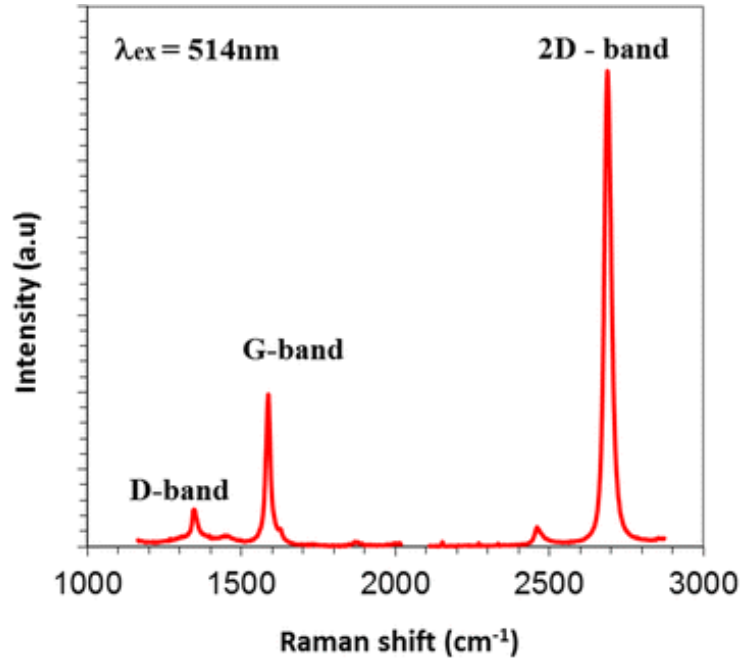


**Figure 2.6: Raman spectrum of graphene showing the D-band at 1350 cm<sup>-1</sup>, G-band at 1580 cm<sup>-1</sup>, and the 2D-band at 2700 cm<sup>-1</sup> (This figure from [31] is under a Creative Commons Attribution 4.0 International License)**

The ratio of the intensity of the D and G peaks allows us to characterize the defectiveness of graphene samples. At a substantially ‘low’ defect density, the ratio of the D and G peak increases with increasing defect density due to elastic scattering within the graphene crystal structure. This occurs up to a regime, where at a substantially high defect density the carbon structure is considered highly amorphous. This results in a decrease in all Raman active peaks. [14,17] It has been proposed that an empirical formula can relate the ratio, and the average distance between defects,  $L_G$ , which is given below. [17]

$$\frac{I_D}{I_G} \propto L_D^{-2} \quad (2.2)$$

This is valid for point defects in the graphene layer, which is intuitive as point defects are spread throughout the area of the graphene flake. For edge defects within the graphene layer the following is more appropriate. [17]

$$\frac{I_D}{I_G} \propto L_D^{-1} \quad (2.3)$$

This allows us to easily characterize the defectiveness of graphene samples which may have implications for the effectiveness of sensing performance. This will be useful when we discuss the defectiveness of synthetic and natural graphite by Raman spectroscopy.

### 2.3 Atomic Force Microscopy

Atomic force microscopy (AFM) is a widely used scanning probe microscopy (SPM) characterization technique. AFM has an enormous resolution on the order of a fraction of a nanometer in some cases, a resolution thousands of times beyond Abbe's optical diffraction limit. [18] There are three major applications of AFM. First, is the imaging of nanoscale objects, second is the measurement of materials properties such as the Young's Modulus, and lastly to manipulate objects at the atomic scale. [19,20] The technique is able to create high resolution 3D images of the topography of a sample using raster scanning. The topography (phase etc.) are often plotted with pseudo color with colors of black, yellow, orange, and white.

A typical AFM apparatus is composed of a cantilever which is positioned by a support, this connects to a piezoelectric element (optional). The cantilever has a probe which interacts with the sample due to oscillations of the cantilever. A beam of light from a laser diode deflects from the cantilever and into a detector which measures changes in this deflection. From this,

topography, phase, and more are able to be imaged. An illustration is given for the apparatus in fig 2.7.

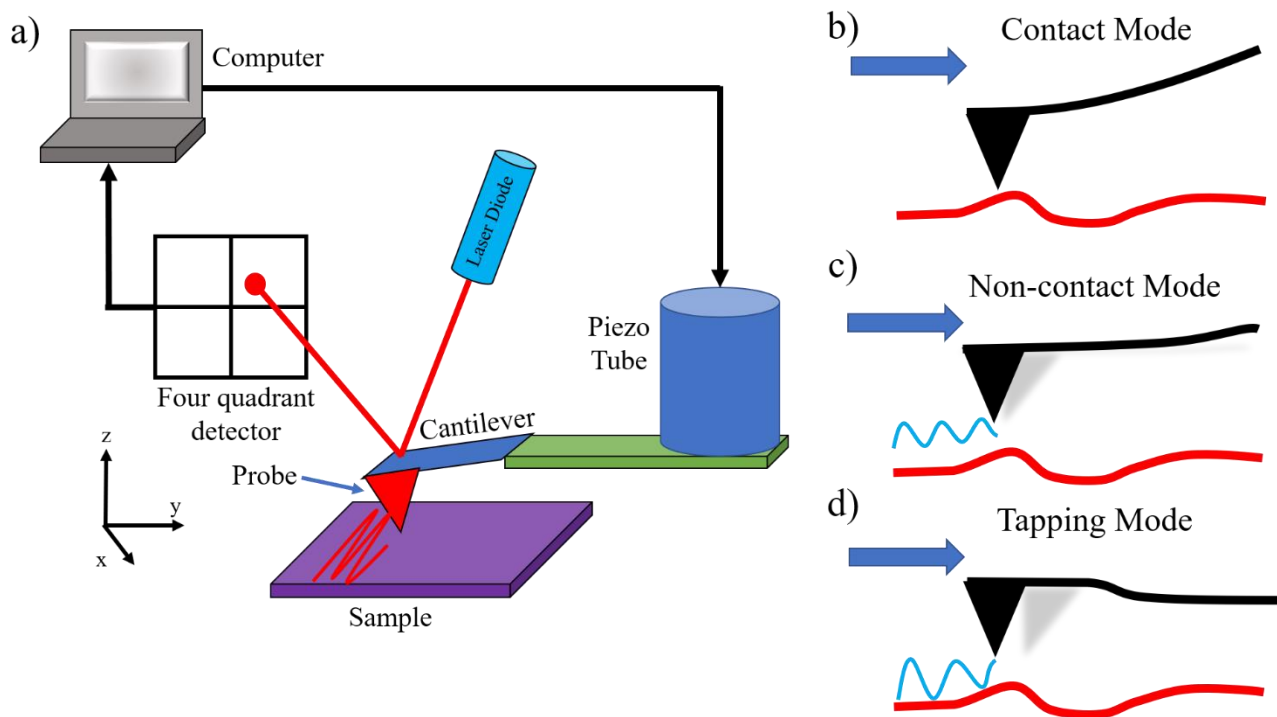


**Figure 2.7: Atomic force microscope (AFM) a) shows device illustration, b) shows contact mode whereas c) shows a non-contact mode AFM, d) shows tapping mode AFM**

The AFM probe is dragged along the surface of the sample in an array of points which creates an image.

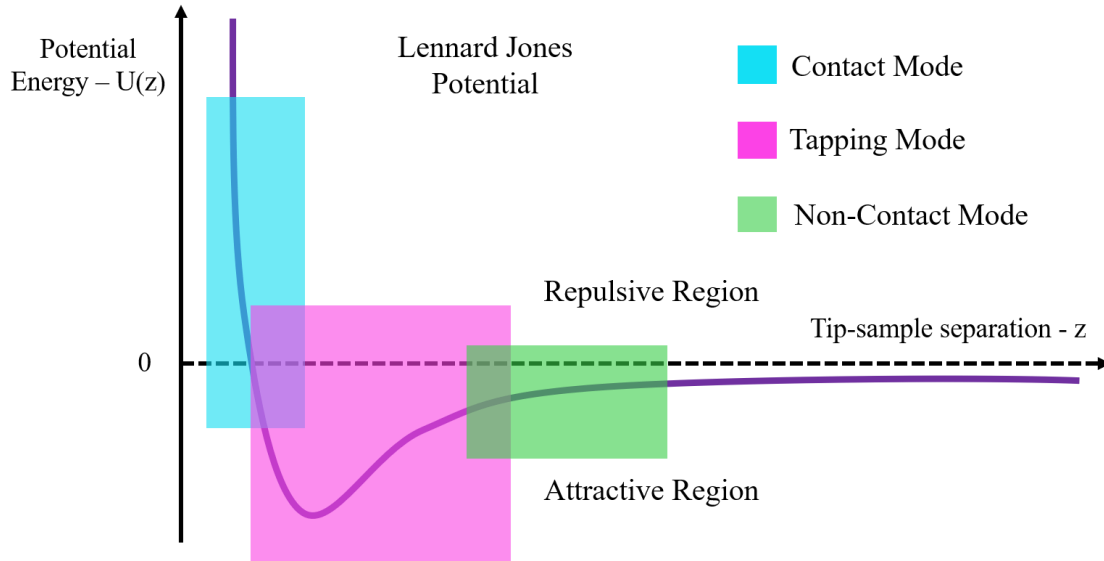


**Figure 2.8: Regions in the Lennard-Jones potential where different AFM modes operate, contact mode (blue) operates in the repulsive region where the tip is closest to the sample, tapping mode (magenta) operates in the most attractive region where the tip is moderately close to sample, and non-contact mode (green) which operates where the distance between the tip and sample is large and the electrostatic attraction is minimal**

The interaction between the tip and the sample has a potential energy which is given by the Lennard-Jones potential (see equation 2.4).

$$U(z) = 4\varepsilon \left\{ \left( \frac{\sigma}{z} \right)^{12} - \left( \frac{\sigma}{z} \right)^6 \right\} \quad (2.4)$$

where  $\varepsilon$  is the depth of the potential well, and  $\sigma$  is the distance where the interparticle potential is zero. Contact mode AFM operates when the tip and the sample are very near and thus is the area of greatest electrostatic repulsion or minor attraction. It is also where the magnitude of the force of the interaction is largest. Tapping mode AFM operates in the area of relatively large electrostatic attraction. Non-contact AFM operates when the distance between the tip and sample is large and the magnitude of force of the interaction approaches zero.

The probe or tip can be made of insulating, conducting, or magnetic material. This allows different material properties to be measured, such as, Van der Waals forces, mechanical contact forces, electrostatic forces, and magnetic forces. By making the probe and sample conductive, the AFM forms a capacitor, this technique is known as Kelvin Probe Force Microscopy (KPFM) and is often used to measure the work function of metals and the surface potential of other materials. [21] Non-contacting and tapping modes are better suited for samples which are very thin and sensitive to damage. Molecular sized images are possible to image with such techniques.

## 2.4 X-Ray Diffraction

X-Ray diffraction (XRD) is an analytical technique for characterizing crystalline materials and can yield information about the dimensions of the unit cell. XRD is based off the discovery by Max von Laue in 1912, who discovered that crystalline materials act as diffraction gratings for radiation in the X-ray wavelength. [22] X-ray diffraction is based on constructive interference from monochromatic X-rays interacting with a crystalline material. The X-rays are typically generated by cathode ray tubes, filtered in order to create monochromatic X-rays, and then collimated to allow for diffraction, the X-rays are then directed towards the sample. Constructive interference of the X-rays happens when Bragg's law (see equation 2.5) is satisfied. [23]

$$n\lambda = 2d \sin(\theta) \quad (2.5)$$

The diffracted X-rays can then be collected by a detector and counted. By scanning through  $2\theta$  angles all diffraction directions can be detected due to random arrangements of the material which is often in a powder form. The d-spacing defines the dimensions for the crystal material. [23,24]

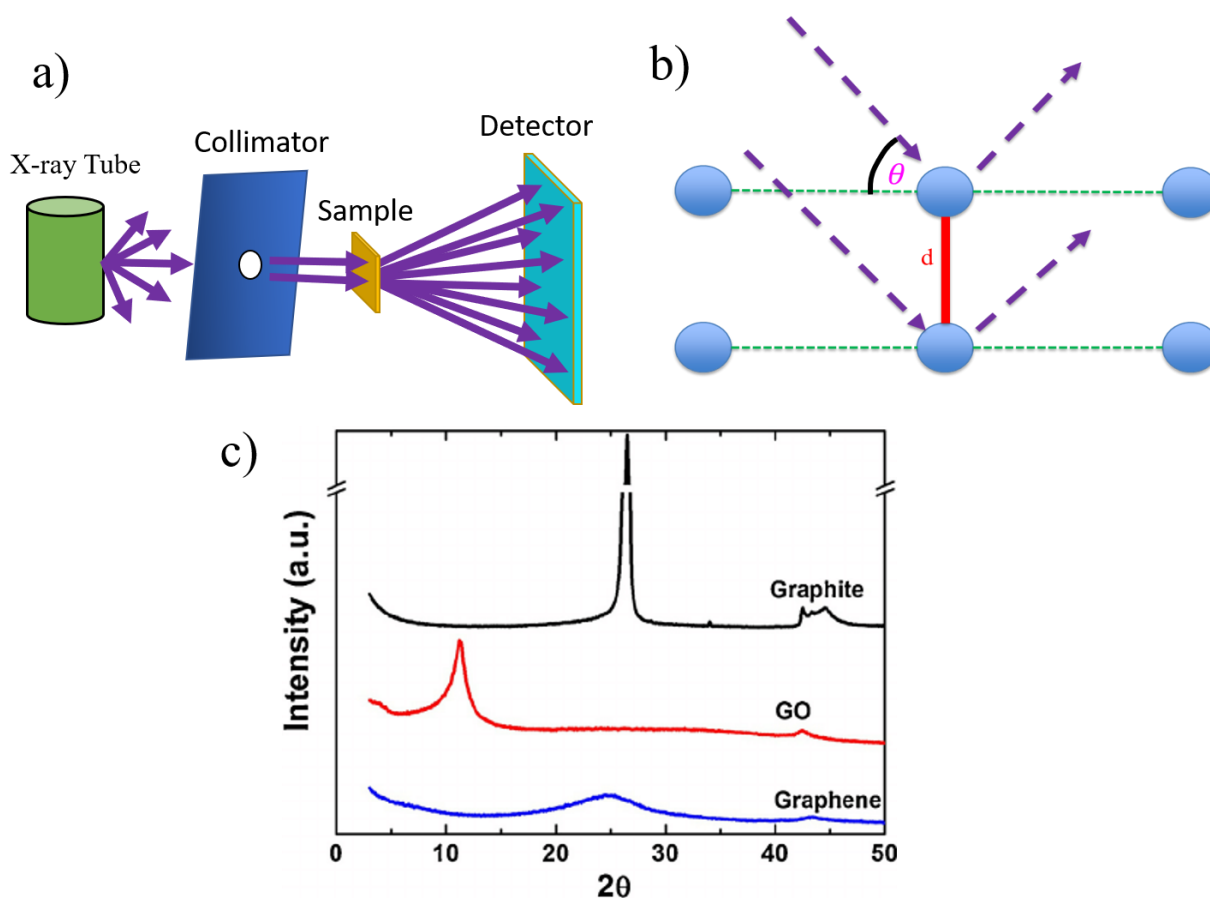


**Figure 2.9: X-ray diffraction setup a) shows an XRD schematic consisting of monochromatic X-ray source which is then collimated and directed to sample where diffraction pattern is produced, b) shows the process of Bragg diffraction c) shows a typical XRD spectra of graphite, graphene, and graphene oxide (This figure from [30] is under a Elsevier License Agreement see 5.3 for further details)**

For determining the interlayer spacing of materials like graphite, the c-axis peak (with Miller indices of 002) can be found at around 26 degrees. Mono-layer graphene should not have a 002 peak in an XRD spectra as there is only one layer of graphene and thus diffraction can not occur. Fig 2.8 c) also shows that the XRD spectra of graphene oxide (GO) shifts down to approximately  $2\theta \approx 10.3^\circ$ , this is due to the intercalation of oxide functional groups, which alters the Van der

Waals potential between layers and increases the distance between layers. In this thesis XRD was used to characterize the c-axis interlayer spacing of multi-layer graphene (non-GO) samples. [24]

## 2.5 Electron Paramagnetic Resonance

It is often necessary to investigate materials which contain paramagnetic sites, this is where electron paramagnetic resonance (EPR) which is also sometimes known as electron spin resonance (ESR), becomes useful. Paramagnetic sites in graphene may be caused by point defects within the crystalline structure of graphene.

$$E = m_s g_e \mu_B B_0 \quad (2.6)$$

Where,  $m_s$  is the electrons magnetic moment and has values of  $m_s = \pm \frac{1}{2}$ ,  $g_e$  is the electrons Landè g-factor and has a value of about 2.0023 for a free electron,  $\mu_B$  is the Bohr magneton, and lastly  $B_0$  is the strength of the magnetic field, a value which is tunable. [28] The technique works by splitting the energy of unpaired electrons by utilizing the Zeeman effect (equation 2.6). Where a magnetic field can split the energies of free electrons as shown in figure 2.7. [25-27] The sample is placed in a microwave cavity, where the interactions between the microwaves and the electrons allows for transitions between the splitted energy states. [25-27] The Zeeman effect tells us how the energy levels split within an atom in the presence of a magnetic field. When the field is relatively weak the interaction can be modelled using the total angular momentum.

$$\vec{J} = \vec{L} + \vec{S} \quad (2.7)$$

Where  $\vec{L}$  is the orbital angular momentum, and  $\vec{S}$  is the spin angular momentum. When the spin-orbital coupling is dominant, the total angular momentum  $\vec{J}$  can be visualized as a vector which

is the vector sum of the both the spin and orbital angular momenta, which precesses around the magnetic field. When the magnetic field is sufficiently large  $\vec{L}$  and  $\vec{S}$  couple more to the magnetic field than to each other. This causes a different pattern in the splitting of the energy level within an atom. This effect is known as the Paschen-Back effect and may allow for more transition possibilities which may in turn alter the EPR signal in the form of a greater number of absorption peaks.

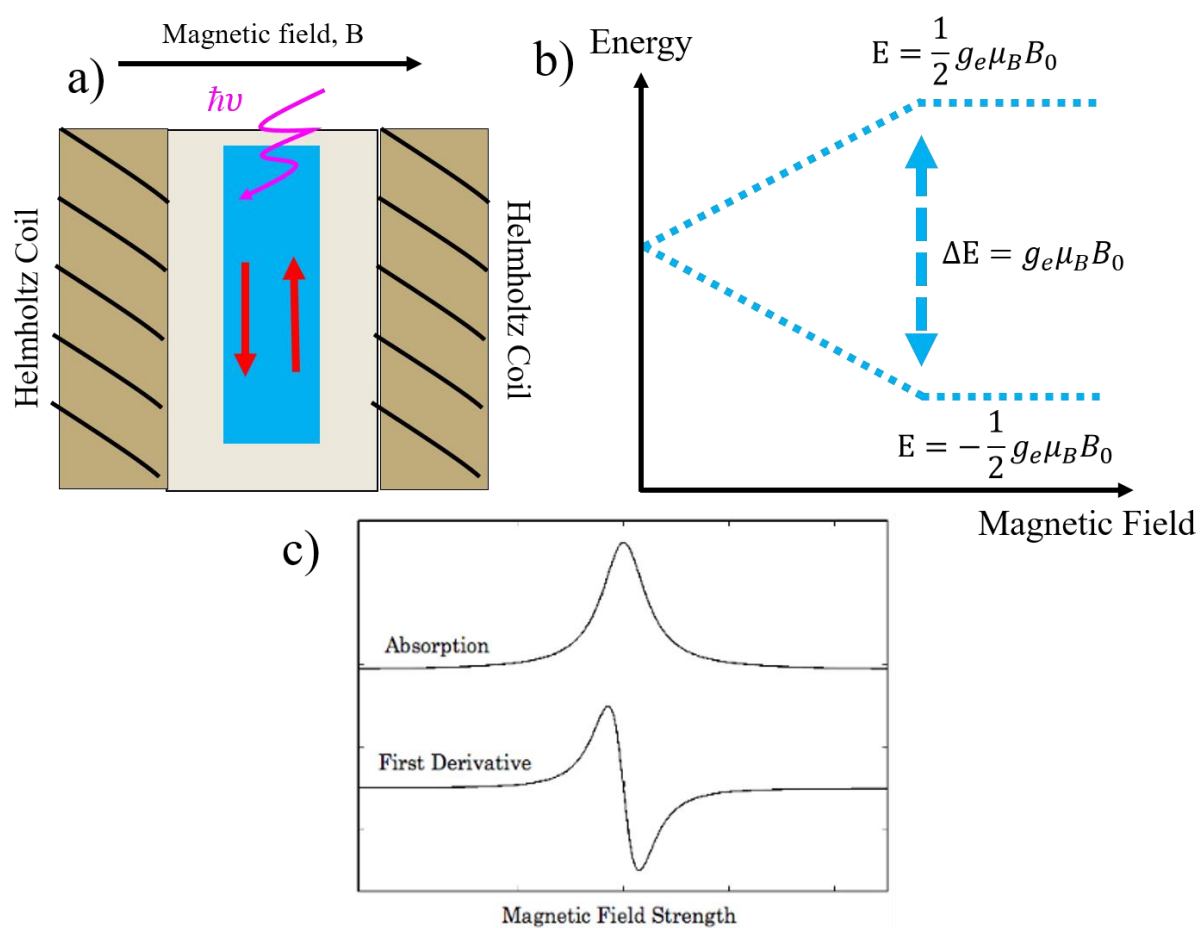


**Figure 2.10: Electron paramagnetic resonance technique a) shows schematic of apparatus where sample (blue) is placed into microwave cavity where microwaves (magenta) interact with paramagnetic centers (red), Helmholtz coils induced magnetic fields, b) shows the Zeeman effect where the energy separation of electron spins is tunable by application of**

**magnetic field, c) shows typical spectra from EPR with both the absorption and the first derivative (This figure from [32] is under a Creative Commons Attribution 3.0**

**International License)**

Microwaves irradiate the sample with a frequency which is held fixed, and the strength of the magnetic field is gradually increased. This causes a larger separation between the energy levels of the magnetic spins within the sample. Eventually, the energy separation is large enough that it becomes equivalent to the energy from the microwaves. When this condition is met (equation 12), transitions between the two energy states is permitted. [28]

$$\hbar\nu = g_e\mu_B B_0 \quad (2.8)$$

The sample will then maximally absorb the microwaves and allow for the greatest number of transitions. However, due to the Paschen-Back effect previously mentioned, the fine splitting allows for a splitting of possible transitions. Due to this effect we may see an increase in the number of absorption peaks.

The density of spins can be calculated by utilizing a reference, where a known concentration of paramagnetic sites is used. This is done by computing the double integral of the EPR signal for both the reference and the sample. The result from the sample can be compared to the reference and a spin density can be calculated. Using this technique, we will be able to get quantitative values for the number of paramagnetic sites in graphite samples, which will give in divalent cations for the defectiveness of the graphite.

## 2.6 Conclusion

In this chapter we introduced five experimental techniques which will be required for the duration of the thesis. Thermal evaporation was used to deposit thin films of aluminum onto

microporous membrane supports, which act as the electrodes for our chemiresistor device in chapter 2. Raman spectroscopy was performed, and by using the ratio of the G, and D spectral peaks, we are able to approximate defectiveness within graphene samples. Atomic force microscopy was also discussed, and the three modes of operation explained by the interaction of the tip and sample, which is modelled by the Lennard-Jones potential. X-ray diffraction was introduced, and the technique for calculating the c-axis interlayer spacing from an XRD spectra was discussed. Electron paramagnetic resonance was also introduced and how this method is able to determine the number of paramagnetic sites within a graphene was mentioned. The aforementioned methods will be of the utmost importance for the coming chapters.

## References

- [1] F. Lévy, *Reference Module in Materials Science and Materials Engineering*, **2016**,
- [2] W. M. Haynes, *CRC Press/Taylor and Francis*, **2014**, 95
- [3] G.S. Bumrah, R. M. Sharma, *Egyptian Journal of Forensic Sciences*, **2016**, 6, 209-215, 3
- [4] D. J. Gardiner, *Springer-Verlag.*, **1989**
- [5] F.A. Settle, *Prentice, Inc., New Jersey*, **1997**
- [6] J.M. Chalmers, H.G.M. Edwards, M.D. Hardgreaves, *John Wiley & Sons Ltd.*, **2012**
- [7] D. A. Skoog, F. J. Holler, S. R. Crouch, *Cengage Learning*, **2006**
- [8] H. H. Willard, L. L. Meritt Jr., J. J. Dean, F. A. Settle Jr., *CBS Publisher & Distributors*, **1988**
- [9] E. Smith, G. Dent, *John Wiley & Sons*, **2005**
- [10] *Vrije Universiteit Brussel: Surf*, Raman
- [11] R. Saito, M. Hofmann, G. Dresselhaus, A. Jorio, M. S. Dresselhaus, *Adv. Phys.*, **2011**, 30, 413-550.
- [12] F. Tuinstra, L. Koenig, *J. Chem. Phys.*, **1970**, 53, 1126-1130.
- [13] A. C. Ferrari, J. Robertson, *Phys. Rev. B*, **2001**, 64, 075414
- [14] I. Childres, L. A. Jauregui, W. Park, H. Cao, Y. P. Chen, *New developments in photon and materials research*, **2013**, 1
- [15] R. Narula, S. Reich, *Phys. Rev. B*, **2008**, 78, 165422

- [16] P. Venezuela, M. Lazzeri, F. Mauri, *Phys. Rev. B*, **2011**, 84, 035433
- [17] M. M. Lucchese, F. Stavale, E. H. Ferreira, C. Vilani, M. V. O. Moutinho, R. B. Capaz, C. A. Achete, A. Jorio, *Carbon*, **2010**, 48, 1592-1597
- [18] E. Abbe, *Anatomy*, **1873**, 9, 413
- [19] L. Yoo, J. Reed, A. Shin, J. L. Demer, *J Biomech*, **2015**, 47, 1899-1903
- [20] M. Ternes, C. P. Lutz, C. F. Hirjibehedin, F. J. Giessibi, *Science*, **2008**, 319, 1066-1069
- [21] M. Nonnenmacher, M. P. O'Boyle, H. K. Wickramasinghe, *Appl. Phys. Lett.*, **1991**, 28, 2921
- [22] M. Eckert, *Annalen der Physik*, **2012**, 5234(5), A83-A85
- [23] A. A. Bunaclu, E. g. Udriştiou, H. Y. Aboul-Enein, *Critical Reviews in Analytical Chemistry*, **2015**, 45, 289-299
- [24] H. Wu, F. Carotti, R. Gakhar, R. O. *Data in Brief*, **2018**, 20, 1816-1821
- [25] C. Naccache, *Magnetic Resonance in Colloid and Interface Science*, 1980, 61, 27-31
- [26] J. E. Wertz, J. R. Bolton, *Electron spin resonance*, **1971**
- [27] P. B. Ayscough, *Methuen and Co LTD, London*, **1967**
- [28] B. Odom, D. Hanneke, B. D'Urso, G. Gabrielse, *Physical Review Letter*, **2006**, 97(3), 030801
- [29] HORIBA Scientific, *AZoM*, **2019**
- [30] F. T. Johra, J. W. Lee, W. Jung, *Journal of Industrial and Engineering Chemistry*, **2014**, 20(5): 2883-2887

- [31] S. M. Hussein, I. F. Crowe, N. Clark, M. Milosevic, A. Vitavaraghavan, F. Y. Gardes, G. Z. Mashanovich, M. P. Halsall, *Nanoscale Research Letters*, **2017**, 12
- [32] M. Pavan, V. Raja, A. R. Barron, A. R., *Chem Libre Texts*, **2019**
- [33] L. M. Malard, M. A. Pimenta, G. Dresselhaus, M. S. Dresselhaus, *Phys. Rep.*, **2009**, 473, 51–87
- [34] A. C. Ferrari, D. M. Basko, *Nat. Nano.*, **2013**, 8, 235-246

## Chapter 3

Tremendous efforts have been undertaken in the fields of nanofiltration and sensing in order to develop water purification and diagnostics devices that are both selective and highly sensitive [1], and special efforts in this area are devoted to the detection of cadmium divalent cations during water purification processes. The substantial effort with  $\text{Cd}^{2+}$  ions are due to their harmful health effects on the human body. Even low levels of exposure to cadmium are known to cause kidney damage, bone demineralization, breast and lung cancer and more [2–5]. Inhalation of cadmium is also associated with fever and in some cases death [6]. Cadmium is necessary in many areas of industry such as in nickel-cadmium rechargeable batteries, photoconductive surfaces for display monitors, and luminescent quantum dots. The US Environmental Protection Agency (EPA) allows for a maximum permissible limit of cadmium of 5ppb, anything exceeding this limit is considered harmful [7,8]. Thus, it is of the utmost importance that cheap and effective in-line methods capable of estimating the amount of cadmium in both the ecosystem as well as the water supply become developed. Several techniques have become developed in order to determine the amount of cadmium in solution. These methods are primarily spectroscopic techniques including atomic absorption spectroscopy, neutron activation spectroscopy, inductively coupled plasma mass spectroscopy, atomic emission spectroscopy, and others [9–12]. Other methods that have been developed are electrochemical cells, and metal oxide nanoparticle or DNA based biosensors [13–17]. The issue with spectroscopic and electrochemical methods is that these are often expensive techniques and make it impossible for in-line measurements of cadmium contaminants, because they require to disperse specific agents that are undesirable in purified water. These also require that a trained individual is required off-site in order to conduct these

measurements. It is necessary to use solid-state devices as this allows for filtrating and sensing without contaminating the water. Solid-state devices for nanofiltration have previously shown issues in terms of selectivity of cadmium ions. Work has recently been done to capture  $\text{Cd}^{2+}$  in the solid state by using  $\text{MoS}_2$  functionalized with cysteine [18]. Additional efforts have been made to increase the porosity of graphene by the deposition of Cu-nanoparticles and their subsequent etching [8]. Graphene is a two-dimensional solid with very highly sought-after properties [19]. It is a zero-band-gap semiconductor with the potential to be dramatically influenced by functional groups [20]. In this paper, we will take advantage of the unique properties of graphite at low defectiveness and its affinity with specific triblock copolymers, in order to create a highly effective in-line sensing apparatus for water quality diagnostics from multilayer graphene. Our device may detect divalent cations below the EPA's permissible limit of 5 ppb for cadmium [10]. This device utilizes cheap and lithography-free microporous membrane supports as well as low-cost data acquisition kits. The device operates in the solid state and thus does not add contaminants to water; it has the potential to be integrated in-line in water filtration apparatuses.

## 3.1 Materials and Methods

### 3.1.1 Sensor and platform design

In order to fabricate our nanofiltration and sensing devices, graphene-based cakes have been deposited onto poly(ether)sulfone (PES) membranes (MicroPES™ FlatMembrane, 3M Canada Co.) which have a significantly higher porosity than graphene and graphite. PES is a microporous membrane material with an average pore size of about 1  $\mu\text{m}$ . Graphene-based cakes have been deposited onto the PES membranes from solution using a vacuum filtration method using a Millipore C164 glass microanalysis filter holder. During vacuum filtration, a differential

pressure of about 60 kPa was established at the membrane, using a Welch (DryFast, Collegiate) diaphragm pump. In order to deposit the graphene-based filter cake, 20 mL of 5 mg/mL of multilayer graphene based aqueous suspension, prepared as below, is utilized.

A graphene-based aqueous suspension was prepared by exfoliating graphite by ultrasonication (Emerson, Branson DHA-1000, 40 kHz 1000 W, 1-hour processing) in a water solution of poly(ethylene glycol)-block-poly(propylene-glycol)-block-poly(ethylene glycol) (PEG-PPG-PEG) triblock copolymer. PEG-PPG-PEG has been demonstrated to exfoliate graphite into high-concentration aqueous dispersions of few layer and multilayer graphene [19], and further details of the exfoliation mechanism not relevant to this study will be offered elsewhere. Two types of graphite have been exfoliated in PEG-PPG-PEG and tested in our water filtration and diagnostics experiments: synthetic turbostratic microcrystalline graphite produced by a turbostratic method (Sigma Aldrich, 282863) and natural hydrothermal graphite (Zenyatta Inc.) ensuring unique properties such as high crystallinity [21]. For hydrothermal vein graphite, four distinct sample batches have been tested at flake diameters of 2.5  $\mu\text{m}$ , 5  $\mu\text{m}$ , 7.5  $\mu\text{m}$ , and 17.5  $\mu\text{m}$ . The 17.5  $\mu\text{m}$  sample was used for sensing experiments as it yields the optimal performance. For synthetic turbostratic graphite, a flake diameter of 20  $\mu\text{m}$ , comparable as possible with the optimized natural graphite diameter, have been used.

In order to determine the role of the block copolymer in our sensing processes, raw graphitic materials were exfoliated using PEG-PPG-PEG at three different polymer chain lengths: i) Pluronic® L-31, BASF Co., average molecular weight  $M_n=1100$  amu; ii) Pluronic® P-123, BASF Co., average molecular weight  $M_n=5600$  amu; and iii) Pluronic® P123, BASF Co.,  $M_n=14,600$  amu. In all cases, PEG-PPG-PEG was dissolved at 0.4 mg/mL in deionized water. After which the various types of graphite previously mentioned were added to this solution at 5

mg/ mL. This produces a black ink in water with minimal residual upon 12h sedimentation.

Vacuum filtration of this ink results into a thick and black stable graphene-based filter cake onto the PES membrane, as shown in Fig. 3.1.

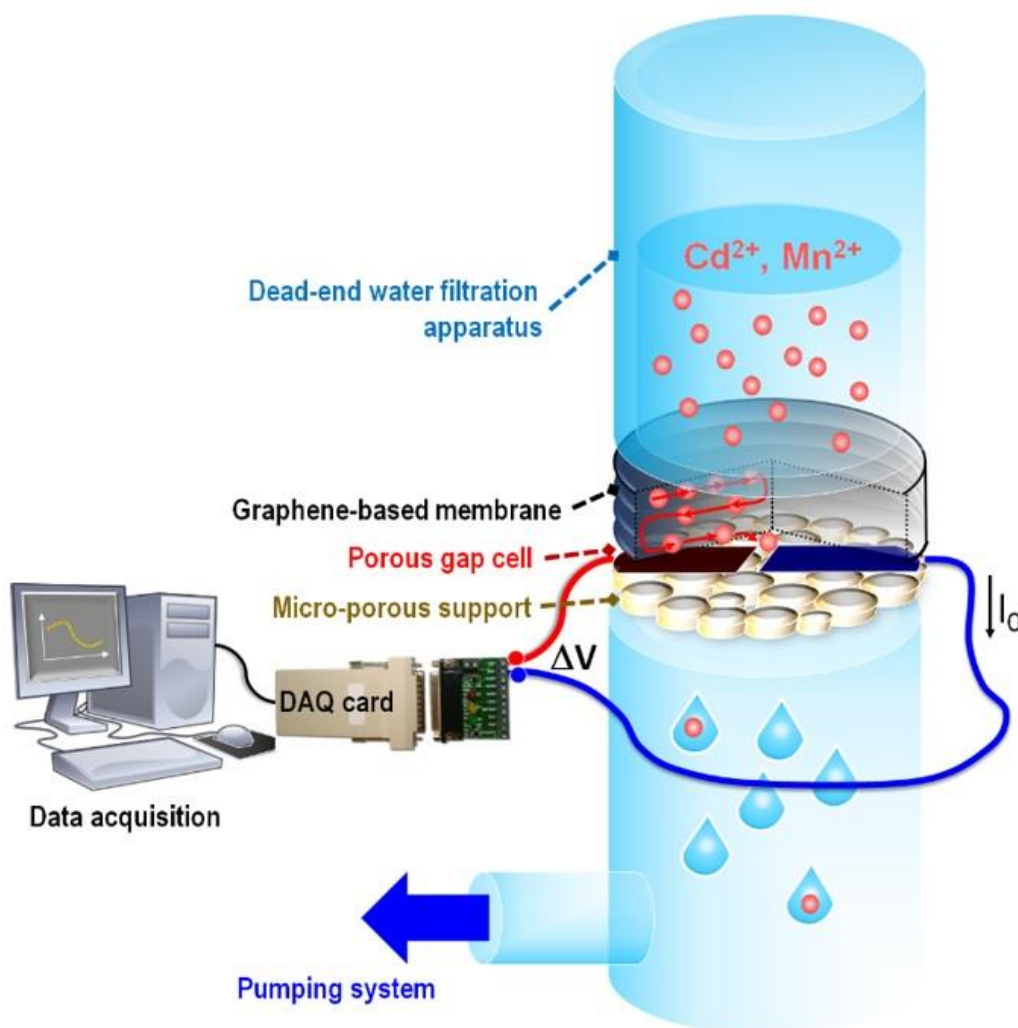


**Figure 3.1.** Graphene-based water filtration and sensing apparatus used in this study. The apparatus utilizes a data acquisition card to create IV curves which allows a computer to calculate the resistivity across the gap cell. The gap cell is the area in between the two aluminum contacts (black and blue). Water is filtered through this process with various types of contaminants and with varying concentrations. The graphene-based filter cake

**captures contaminants which results in a change in the gap cells resistivity acquired over time by the data acquisition system.**

Prior to the deposition of graphene-based filter cakes on PES membranes, aluminum contacts (22 mm width, 25  $\mu\text{m}$  channel length) were thermally evaporated at room temperature onto the PES membranes through a shadow mask utilizing a 25  $\mu\text{m}$  Ni wire to form the channel. In this way porous and flexible gap cells on PES were obtained. The gap-cell thermal evaporation has been carried in an ultra-high vacuum chamber (base pressure of  $10^{-7}$  Pa) using aluminum pellets (99% purity K.J. Lesker Inc.). Aluminum pellets were placed in alumina crucibles (K.J. Lesker cat. no. EVA9AO) supported by a tungsten basket heater (K.J. Lesker Inc., cat. no. EVB8B3030W). Heat was supplied to these assemblies by a 70 A direct current at 9.0 V, via a Hewlett Packard 6466C DC power supply. Thickness of the growing Al film was measured using a calibrated quartz crystal oscillator attached to a Sycom STM-2 thickness monitor. A thickness of 200nm of Al was deposited at  $5.0 \times 10^{-7}$  Pa base pressure. The deposition temperature was kept below 100  $^{\circ}\text{C}$  during the deposition, which is compatible to PES temperature stability. A low deposition rate of  $15 \text{ \AA s}^{-1}$  was used to ensure low temperature during deposition.

### 3.1.2 Sensor Data Acquisition

The sensor device is operated by connecting the chemiresistor gap cell to a digital-analog data acquisition (DAQ) converter (Series 300, EMANT PTE) which can be connected to the USB 2.0 port of a personal computer. An array of analog currents, generated by the USB 2.0 port is fed through the gap cell, and the resulting voltages are measured by the converter and acquired by the personal computer (see Fig. 3.1). The DAQ converter has an 8-bit resolution for its analog input and a 24-bit resolution for its analog output. Data acquisition is performed through a

MATLAB™ routine. The program supplies 0.04 mA of current and proceeds to increment the current by 0.04 mA until a maximum current of 0.6 mA is reached. The corresponding voltages are measured during this process. A second order least-square fit is performed on this data by the same MATLAB™ routine and a value for resistance R is obtained, with the error bar obtained from the quadratic coefficient of the polynomial. The resistivity is then calculated as

$$\rho = \frac{AR}{L} \quad (3.1)$$

where A is the cross-sectional area of the gap cell and L is length of the channel, representing the distance between the electrodes. Resistivity could be acquired and plotted as a function of time, and data were smoothed using a 5-point Savitzky-Golay filter.

### 3.1.3 Sensing Experiments

In order to characterize our devices, preliminary  $\text{Cd}^{2+}$ ,  $\text{Hg}^{2+}$ , and  $\text{Mn}^{2+}$  solutions were prepared at 50 ppm concentration from 1 L of 18 M $\Omega$  deionized water at which requisite amounts of  $\text{CdCl}_2$  (Sigma Aldrich, 24867543),  $\text{HgCl}_2$  (Sigma Aldrich, 215465), and/or  $\text{MnCl}_2$  (Sigma Aldrich, 244589) were added. These chloride salts disassociate in water leaving  $\text{Cd}^{2+}$  (or  $\text{Mn}^{2+}$ ) and two  $\text{Cl}^-$  for each molecule. Solutions pH was not adjusted, as we noticed it has a marginal effect in the filter performance. The 50 ppm solutions were then subsequently diluted to get the requisite concentrations below 50 ppm. Sensing experiments in which the chemiresistor electrical resistivity is continuously monitored as a function of time, as discussed in Section 3.1.2, start by priming the sensor by filtrating 100 mL of 18 M $\Omega$  cm deionized (DI) water for 100 s in a dead-end water filtration configuration (Fig. 3.1) in which the sensing device is inserted between a filtration funnel and a fritted glass platform, which is attached to vacuum filtration flask connected to a Welch diaphragm pump by keeping the flow rate constant at 60 mL/min. After

device priming, 25 mL of DI water with  $\text{Cd}^{2+}$  ions at given concentrations (from 5 ppb to 500 ppb) is poured in the filtration device with the sensor. After the filtration funnel is nearly empty, more pure DI water is supplied in lieu of  $\text{Cd}^{2+}$  containing water, while the gap-cell resistivity continues to be monitored. Subsequent filtration cycles of pure DI water and  $\text{Cd}^{2+}$  containing water have been repeated a number of times, with filter fouling times that depend on the  $\text{Cd}^{2+}$  ion concentration but can be estimated in several tens of minutes. Several filtration cycles were performed to test for stability and reversibility of sensing performance, and for performance limitations due to filter fouling. Afterwards, a new filtration platform can be replaced. An identical procedure has been used to test the system in control experiments with  $\text{Mn}^{2+}$  and  $\text{Hg}^{2+}$  ions. Control experiments have also been performed on bare PES gap cells, without multilayer graphene cake overlapped, to ensure that the resistivity changes in the chemiresistors are related to ion absorption in multilayer graphene, not ionic conductivity from water.

### 3.1.4 Scanning Electron Microscopy

SEM measurements were recorded on a Zeiss LEO 1540XB microscope. In order to improve sample conductivity and enhance resolution, samples were coated with ~5 nm of osmium using a Filgen OPC80T Os plasma coater before images were taken. PES membranes were placed onto a flat sample holder using double-sided carbon tape and silver paint (Pelco® Colloidal Silver Liquid) at the edges of the sample. Samples were then admitted into the SEM vacuum chamber at  $\sim 10^{-6}$  Torr base pressure. The sample morphology images were captured by a secondary emission electron detector at 2.0 kV.

### 3.1.5 Raman Spectroscopy

Unpolarised Raman spectra were recorded in the 100–3200  $\text{cm}^{-1}$  spectral region on a Renishaw InVia spectroscope equipped with a Leica DM2600M microscope and a 20x objective in backscattering arrangement. A 633 nm helium-neon laser with a maximum output power of 17 mW was used as the excitation source. The power at the sample surface was 0.085  $\text{mW}/\mu\text{m}^2$  across a 20  $\mu\text{m}^2$  area. Special attention was paid to avoid damage of the sample by the laser by shuttering the laser when not actively measuring. Raman spectra were recorded using a charged couple device array of 1024×256 pixels, which was cooled to  $-70\text{ }^\circ\text{C}$  using a Peltier cell. The spectrometer was equipped with a lowpass filter for the rejection of elastically scattered laser light. Special attention was devoted to preventing damage to the sample from the laser.

### 3.1.6 Electron Paramagnetic Resonance (EPR)

EPR measurements were recorded on graphite samples used for the fabrication of our graphene-based devices by means of a JEOL FA-200 spectrometer which was operated in the X band (9.5 GHz) at room temperature. Powder graphite samples were positioned into a glass capillary tube with an inner diameter of 1 mm. Capillaries, were then placed into the instrument TE<sub>100</sub> microwave cavity. Natural graphite with average particle sizes of 2.5  $\mu\text{m}$ , 5  $\mu\text{m}$ , and 7.5  $\mu\text{m}$  were measured with a sweep time of 15.0 min, from 332 mT to 372 mT dc magnetic field, with a receiver gain of 200, 0.3 mT modulation width, 0.03 s time constant, a 1 mW microwave power. The same parameters were also used for natural graphite at 17.5  $\mu\text{m}$  flake size, as well as synthetic graphite at 20  $\mu\text{m}$  flake size, but a longer sweep time of 4.0 min was required for these samples at lower EPR signal.

### 3.1.7 Powder X-ray Diffraction (XRD)

Powder XRD measurements were performed on a set of exfoliated graphene samples as well as graphitic raw material. The first sample was as-received natural graphite powder prior to any exfoliation treatment. Another reference sample was prepared from natural graphite exfoliated with sodium dodecyl sulfate (SDS), an anionic surfactant [22], which has been frequently used to produce few-layer graphene in the literature. Two additional samples were prepared by treatment with the lowest and highest molecular weight PEG-PPG-PEG copolymer. All samples were exfoliated as mentioned in sect. 3.1.1. Samples were ground to ensure uniform particle size. Powder diffraction data were collected using an Inel Powder diffractometer equipped with a CuK $\alpha$  sealed tube source, an Inel XRG3000 generator, and an Inel CPS 120 detector. The CPS is a curved detector collecting the diffracted X-rays over  $2\theta$  up to  $120^\circ$ .

## 3.2 Results and Discussion

### 3.2.1 Membrane Characterizations

#### 3.2.1.1 Scanning Electron Microscopy

SEM was performed on two types of samples at similar average flake diameter: natural hydrothermal vein graphite and synthetic graphite, directly on the cakes used for sensing experiments. The images of these samples are shown in Fig. 3.2 very similar between each other. In both samples, the average flake size is about  $2\ \mu\text{m}$  in diameter, which indicates a significant fragmentation of the flakes, over pristine raw graphite material, during their ultrasonication and dispersion in PEG-PPG-PEG. We observe that in both cases we see uniform, dense, and relatively similar filtration “cakes”. This may imply that the difference in sensing between these two samples may be caused instead by microscopic differences between the two systems, for instance differences in the graphene interlayer spacing, or the presence of point defects. These hypotheses will be tested with additional characterization via Raman [23] and EPR [24,25]

spectroscopy, two analytical techniques capable of quantifying the degree of defectiveness and impurities in graphitic systems. We anticipate that very different crystalline quality and defect densities will be found in synthetic/turbostratic and hydrothermal/vein graphite, which will explain the different sensing performance of multilayer graphene exfoliated from these two types of graphite. Although, the SEM images (Fig. 3.2) show relatively thick flakes, the flakes are proper multilayer graphene (or thin graphite) regardless of the number of layers in the flakes.

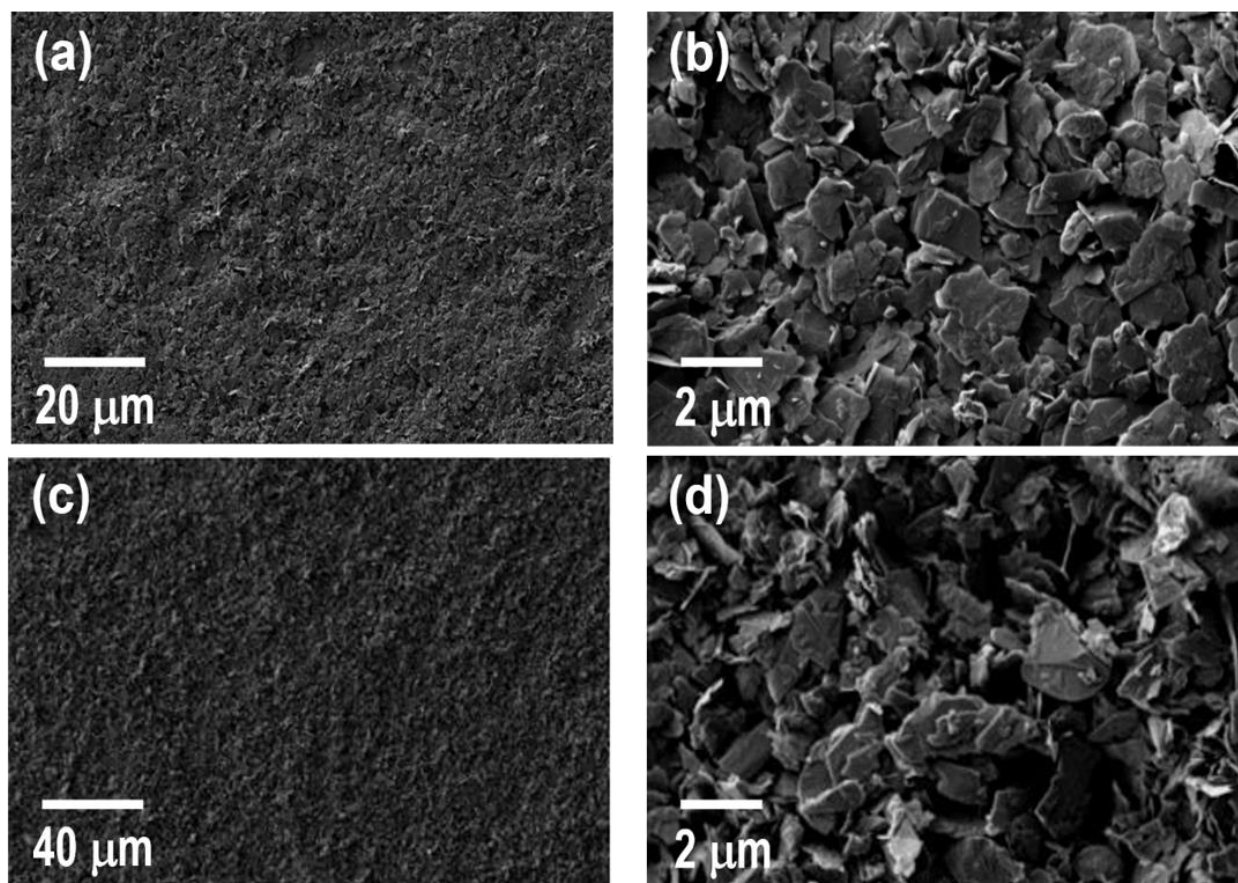


**Figure 3.2: Scanning Electron Microscopy images showing filtration “cakes” prepared from synthetic graphite (top row) at (a) low and (b) high magnification; and natural vein graphite at (a) low and (b) high magnification. Comparison of micrographs recorded from synthetic and hydrothermal graphite reveal that the flake size is the same in both cases.**

The mechanism we are exhibiting cannot be proven in bulk graphite, as flakes which are too thick will result in excessive interflake spacing which will not allow permeation between graphene layers, as most water will pass between graphite grains. Conversely, if single-layer graphene (or few-layer graphite) is used no effect is observed.

### 3.2.1.2 Raman Spectroscopy

Raman spectroscopy was used to investigate the quality of the different multilayer graphene cakes. From Raman data, we can determine some critical parameters that are correlated to the graphene defectiveness, correlation length, or crystallite size. Raman spectroscopy was carried out in order to test the quality of the different multilayer graphene filter cakes. This helped us determine the quality of the resulting multilayer graphene samples before and after PEG-PPG-PEG exfoliation. By considering the Raman spectra of our samples, shown in Fig. 3.2, we can notice the larger and more protruded D-peak of synthetic graphite at  $1360\text{ cm}^{-1}$  frequency shift, to be compared to the lower D-peak intensity of its natural vein counterpart. Due to the equal molecular weight of PEG-PPG-PEG (Pluronic<sup>®</sup> P-123, BASF Co.,  $M_n=14,600$  amu) used to exfoliate both natural and synthetic graphite samples, we can attribute any difference in the Raman-forbidden D-peak intensity to the breathing modes of the  $sp^2$  atoms in the aromatic rings of the graphite [23]. Additionally, we do not see substantial change in the Raman-forbidden D-peak with Pluronic chain length. This peak is only Raman active in the presence of crystallographic imperfections of graphite and graphene, such as: defects, amorphous phases, and finite crystal domains. The G peak, always Raman-active, is noticeable at  $1590\text{ cm}^{-1}$  frequency shift, and is due to the stretching of the  $sp^2$  carbon bonds in both rings and chains [23]. Therefore, a high  $I_D/I_G$  intensity ratio indicates small aromatic domains in graphite or graphene, or, at a constant domain diameter, a higher defect or impurity concentration. Our SEM

measurements show that the crystallite size is the same across all samples. This implies that any change in the  $I_D/I_G$  intensity ratio must be attributed to a change in defect density. This can be quantified by observing [23] that the Raman correlation length,  $L_a$ , is inversely proportional to the  $I_D/I_G$  ratio.  $L_a$  loosely corresponds to the flake diameter in low-defect graphite and graphene, while it is a measurement of the distance between defects or impurities in high-defect graphite and graphene.

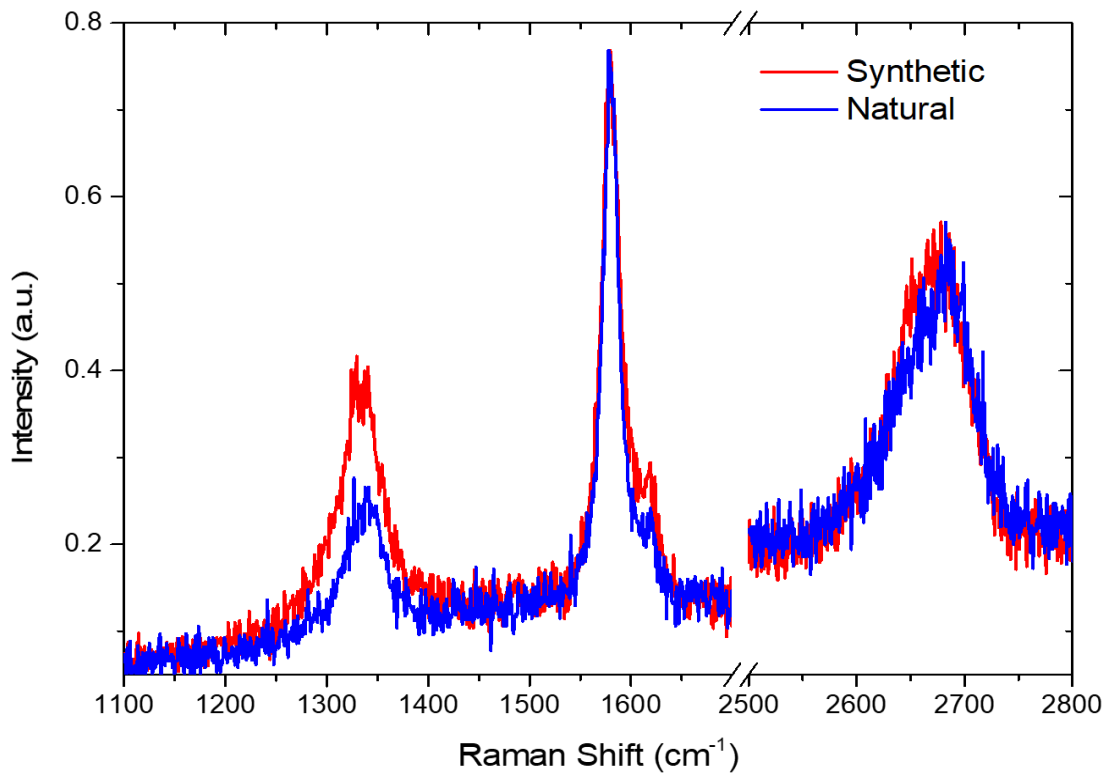


**Figure 3.3: Raman spectra showing the G (1580 cm<sup>-1</sup>) and D (1360 cm<sup>-1</sup>) peaks of natural vein and synthetic graphite, as well as the second-order 2D peak. The higher D peak and  $I_D/I_G$  ratio of synthetic graphite is clearly noticeable**

In Table 1, the  $I_D/I_G$  ratios from our samples are presented, along with the Raman correlation lengths calculated according to Ref. [23]. We know from SEM observations (Section 3.1.1) that

the average crystallite diameter is approximately the same for both natural and synthetic graphite samples (17.5  $\mu\text{m}$  and 20  $\mu\text{m}$ , respectively). Therefore, the lower value of  $L_a$  in synthetic graphite is an in divalent cation that, in this sample, the distance between defects is lower in this sample has a higher defect density. The lower defectiveness of natural vein graphite will also be corroborated by quantitative estimates of the point defect density by EPR spectroscopy. In addition, both samples, synthetic and natural, feature a two-phonon Raman active 2D peak at  $2680\text{ cm}^{-1}$ . The position of this peak corroborates that the active layer of our devices is formed by multilayer graphene, as opposed of graphite or few-layer graphene [23].

	$I_D/I_G$	$L_a$ (nm)
Synthetic/PES	0.454	85
Hydrothermal/PES	0.273	141

**Table 3.1:  $I_D/I_G$  and  $L_a$  values from Raman on natural (hydrothermal) and synthetic graphite.**

### 3.2.1.3 Electron Paramagnetic Resonance

EPR measurements were performed to gain insight into the concentration and nature of paramagnetic defects on the graphite samples tested. There are two major possible causes for paramagnetic centres in graphitic samples [24,25]. The first are defects caused by spins on the edge of the flakes of graphite. The other are defects within the graphite sample. Edge defects on graphite would cause a very distinct trend where the number of spins caused by edge defects would decrease with inverse proportionality with respect to the size of the graphite flake. In Fig. 4, EPR measurements performed on natural graphite samples at different flake size (from 2.5 to 17.5  $\mu\text{m}$ ) indicate that a clear trend exists where the spin concentration caused by defects at the

flake edges is inversely proportional to the size of graphite flakes. In addition to that, Fig. 3.4 shows that synthetic graphite shows a higher paramagnetic defect concentration, which indicates that, at a constant concentration of paramagnetic point defects at the edges, it shows a higher defect concentration within the flakes, which may explain the less consistent interlayer spacing, and the less selective sensing performance, as detailed in the next sections.

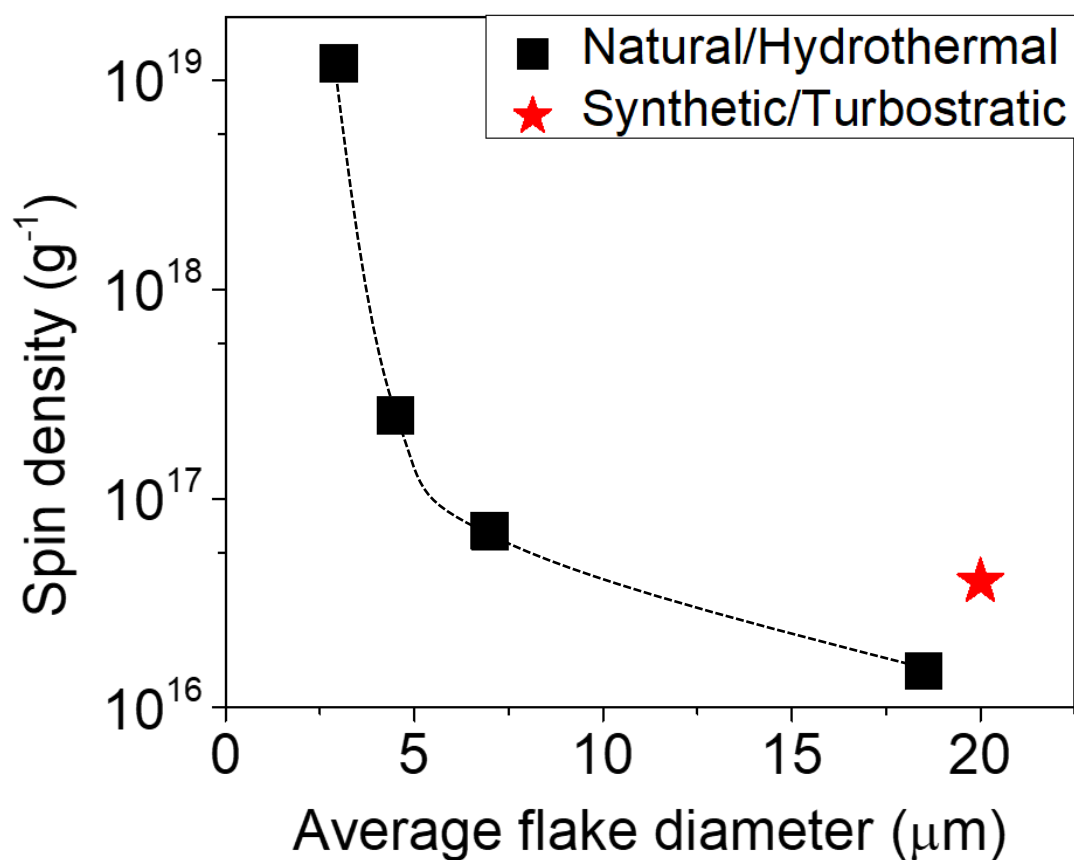
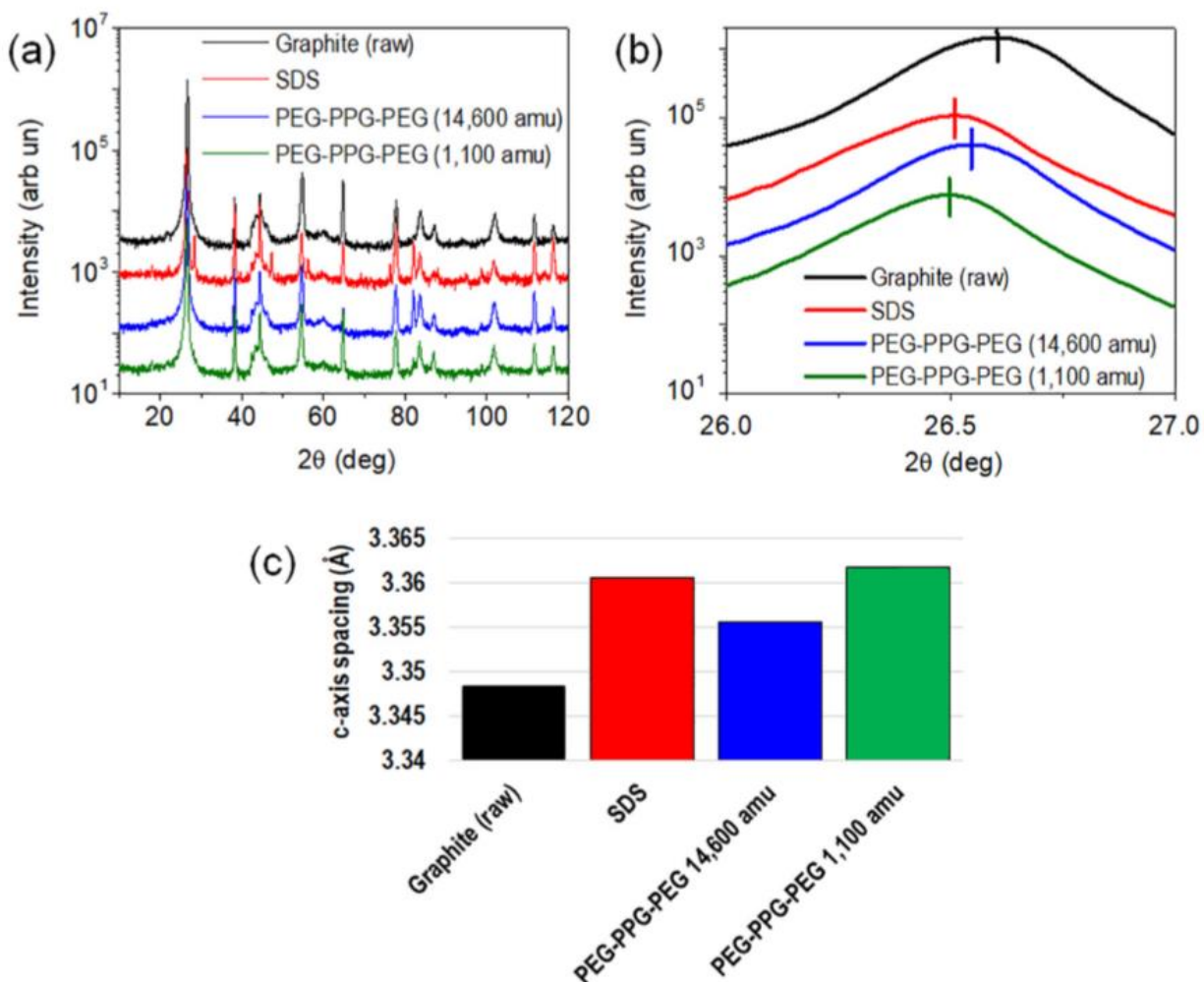


**Fig. 3.4: Concentration of paramagnetic point defects determined from EPR measurements showing the number of spins of hydrothermal vein graphite versus the average size of graphite flakes suggesting that a vast majority of defects sit on the edge of measured flakes.**

#### 3.2.1.4 Powder XRD

Fig. 3.5 demonstrates the effects on the XRD spectra of natural graphite exfoliation with different surfactants, including sodium dodecyl sulfate (SDS) and PEG-PPG-PEG block copolymers at varying molecular weight. We anticipate that, for our water purification performance purposes, the small shifts of the (002) peak at  $2\theta \approx 26\text{--}27$  deg. (highlighted in panel b) are particularly significant. Specifically, the peak position, that can be calculated using Bragg's law [26], (panel c) indicates the c-axis spacing modifications occurring in few-layer graphene due to the intercalation by different types of surfactants. From panel b, a noticeable shift along the (002) plane depending on the type of surfactant being used is noticeable. Specifically, it can be observed that adjustment of the molecular weight of PEG-PPG-PEG allows for tuning of the c-axis spacing from 3.35 to 3.36 Å.

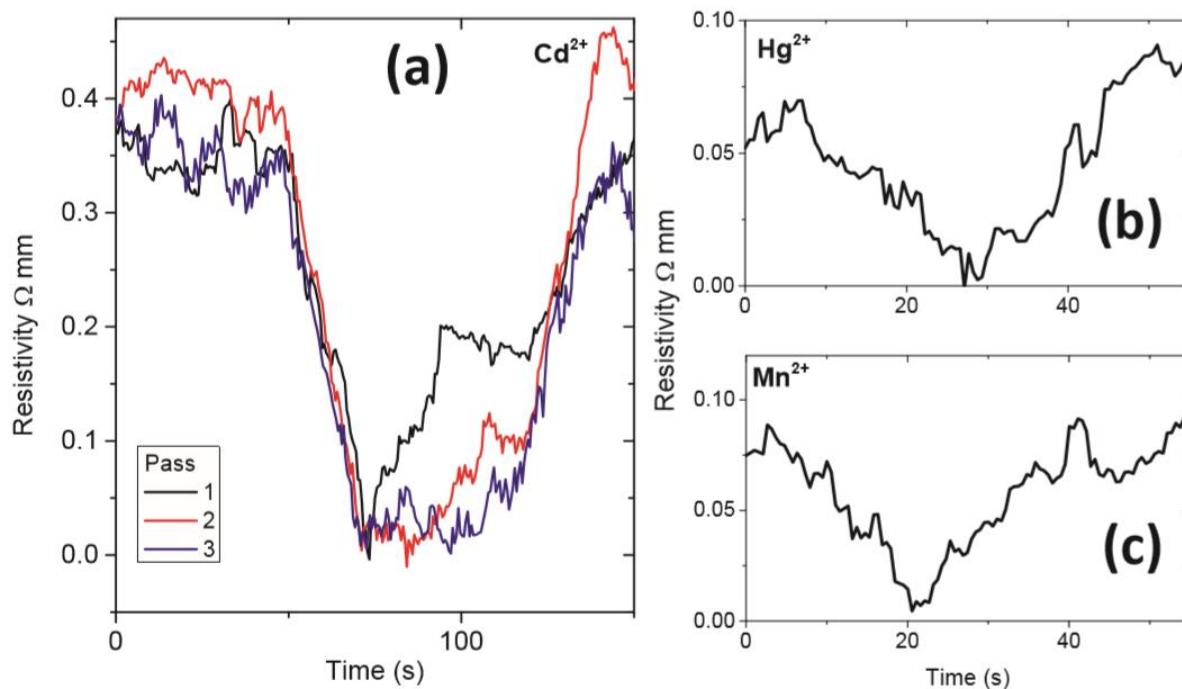
Although this change is relatively small, it is well above the uncertainty limit, and we anticipate it may play a significant role in selective retention of metal ions as their intercalation through graphene layers is extremely sensitive to c-axis spacing. Section 3.2.1 will describe how PEG-PPG-PEG at 11,600 amu molecular weight offers the ideal c-axis spacing for  $\text{Cd}^{2+}$  ion intercalation and trapping in between graphene layers. It is also worth noting that 11,600 amu PEG-PPG-PEG offers a c-axis spacing that is significantly different from both PEG-PPG-PEG at lower molecular weight as well as SDS, a popular surfactant for exfoliating graphite into multi-layer graphene. Furthermore, from Fig. 3.5a, it is apparent that SDS leads to a "satellite" (002) peak at a higher angle, which suggests a multimodal distribution of c-axis spacings for multi-layer graphene exfoliated by this surfactant. Conversely, one single and relatively sharp peak is present in PEG-PPG-PEG exfoliated multi-layer graphene, which suggests a more deterministic c-axis spacing and, consequently, its better suitability towards selective chemiresistor sensing performance.



**Figure 3.5:** (a) X-ray diffraction spectra of graphite powder and multilayer graphene exfoliated from different surfactants. The (002) peak is evident in all cases. A satellite peak is present in SDS-exfoliated multilayer graphene, indicating a multimodal distribution in c-axis spacings; (b) detail of (002) peaks showing shifts different at different values of  $2\theta$  as a consequence of different c-axis spacings; (c) c-axis spacings calculated using Bragg's law. We anticipate that different c-axis spacings lead to different abilities to selectively trap  $\text{Cd}^{2+}$  ions in multilayer graphene interlayers, different electrical properties of graphene and, therefore, tunable sensing performance.

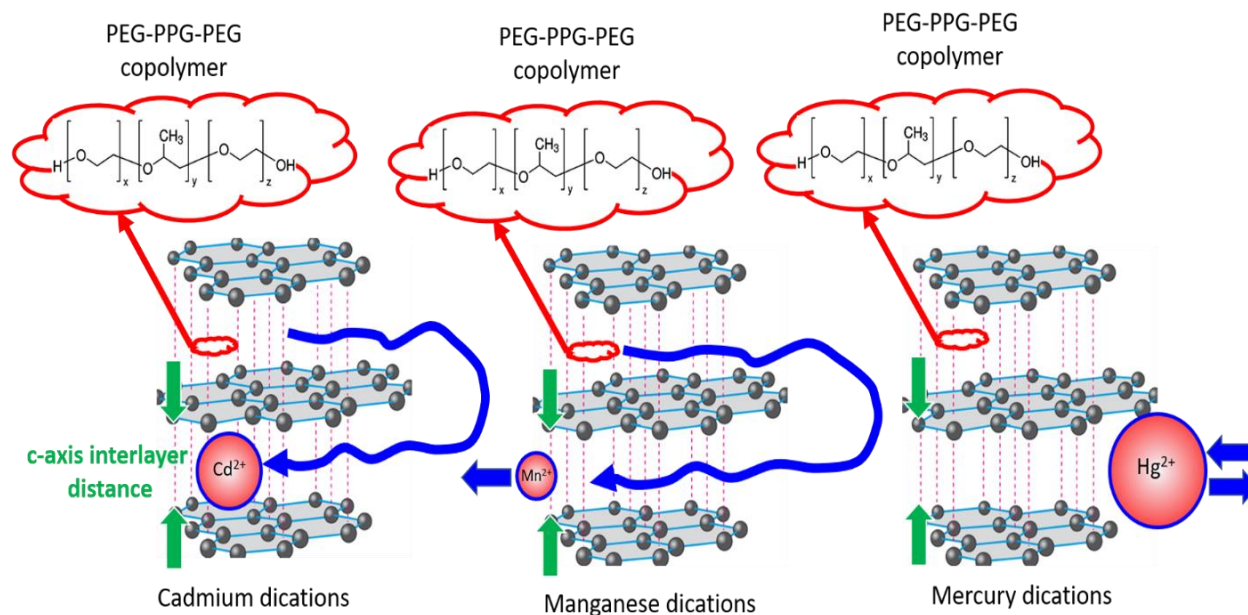
### 3.2.2 Chemiresistor Sensing Performance

Fig 3.6 shows a comparison between the effects caused by the addition of heavy metal containing water to the sensing apparatus. It is seen that the sensor has a much larger sensitivity to  $\text{Cd}^{2+}$  than manganese and mercury. The difference in sensitivity has several possible explanations, one of which is that the ionic conductivity within the gap cell has increased. This, in turn, will result in what appears to be a decrease in the resistivity of the multi-layer graphene within the gap cell. However, several tests can be done to check if the device is only detecting ionic conductivity within the gap cell. No change in conductivity is observed in control experiments without a graphene cake deposited on top of the Al contacts and the microporous PES support. Concerning the specific sensitivity to  $\text{Cd}^{2+}$ , noticeable from Fig. 3.6, we can observe that  $\text{Cd}^{2+}$  ions possess intermediate hydrodynamic radii between  $\text{Mn}^{2+}$  and  $\text{Hg}^{2+}$  [8,26]. Several ‘passes’ were performed for all sensing experiments, to test for potential fouling of filter cakes. It can be observed in Fig. 3.6 c) that there is negligible fouling of filter and no observed change in detection performance.



**Figure 3.6: Response, in terms of resistivity change, of a sensing system with graphene-based active component prepared from natural hydrothermal vein graphite to (a) Cd<sup>2+</sup>, (b) Mn<sup>2+</sup>, and (c) Hg<sup>2+</sup> divalent cations at 125 ppb concentration.**

Smaller ions at lower hydrodynamic radii may easily intercalate through the layers of graphene without being retained. Conversely, the same phenomenon may prevent heavy metal ions, at larger hydrodynamic radius, to penetrate through the interlayer spacings, which may explain why Cd<sup>2+</sup> possess the optimal size for being trapped inside graphene cakes, as depicted in Fig. 3.7, and to produce changes in their conductivity.



**Figure 3.7: Suggested mechanism for capture and sensing of  $\text{Cd}^{2+}$  ions from water by multilayer graphene. Ions get trapped between layers of graphite when their hydrodynamic diameter is close to the interlayer spacing between graphene planes, which is on its turn controlled by intercalation of PEG-PPG-PEG of different chain length. Smaller divalent cations are not retained within the interlayer spacings, while excessively larger ions are not able to intercalate graphene layers.**

Charge transfer between divalent cations and  $\pi$ -electrons in graphene is responsible for the Fermi energy shift from the apex of the Dirac cone, with a consequent increase in conductivity.

Specifically, charge transfer between divalent cations and  $\pi$ -electrons in graphene is responsible for the Fermi energy shift from the apex of the Dirac cone, with a consequent increase in conductivity. Fig. 3.8 demonstrates the relationship between the relative change in the resistivity of the gap cells and the concentration of heavy metal ions filtrated through them. We notice that in devices incorporating synthetic graphite the response at 500 ppb does not have as drastic of a change in resistivity as the response to 125 ppb does. This is most likely due to the device

reaching a saturation concentration and causing the device to have not as large of a response. Fig. 3.8 shows a linear relationship between change in resistivity and impurity concentration for  $\text{Mn}^{2+}$  ions but show a logarithmic trend for  $\text{Cd}^{2+}$ . This is strong evidence that the involved phenomenon is different from that of ionic conductivity within the gap cell is taking place. Ionic conductivity is linear regarding the charge of the ion as well as the charge carrier mobility, and of course the ion concentration, as shown in Eq. (3.2):

$$\sigma_{ion} = N_{ion}q\mu_{ion} \quad (3.2)$$

where  $N_{ion}$  is the charge carrier concentration,  $q$  is the electric charge, and  $\mu_{ion}$  is the carrier mobility.

$$\mu_{ion} = \frac{e\tau}{m} \quad (3.3)$$

The vertical axis in Fig. 3.8,  $\delta\rho/\rho$ , is proportional to the conductivity. Therefore, if the major effect was ionic conductivity within the gap cell then this relationship should always be linear, not logarithmic as observed for  $\text{Cd}^{2+}$  ions. In addition to control experiments without multilayer graphene active layer, this points to a different physical origin of the process.

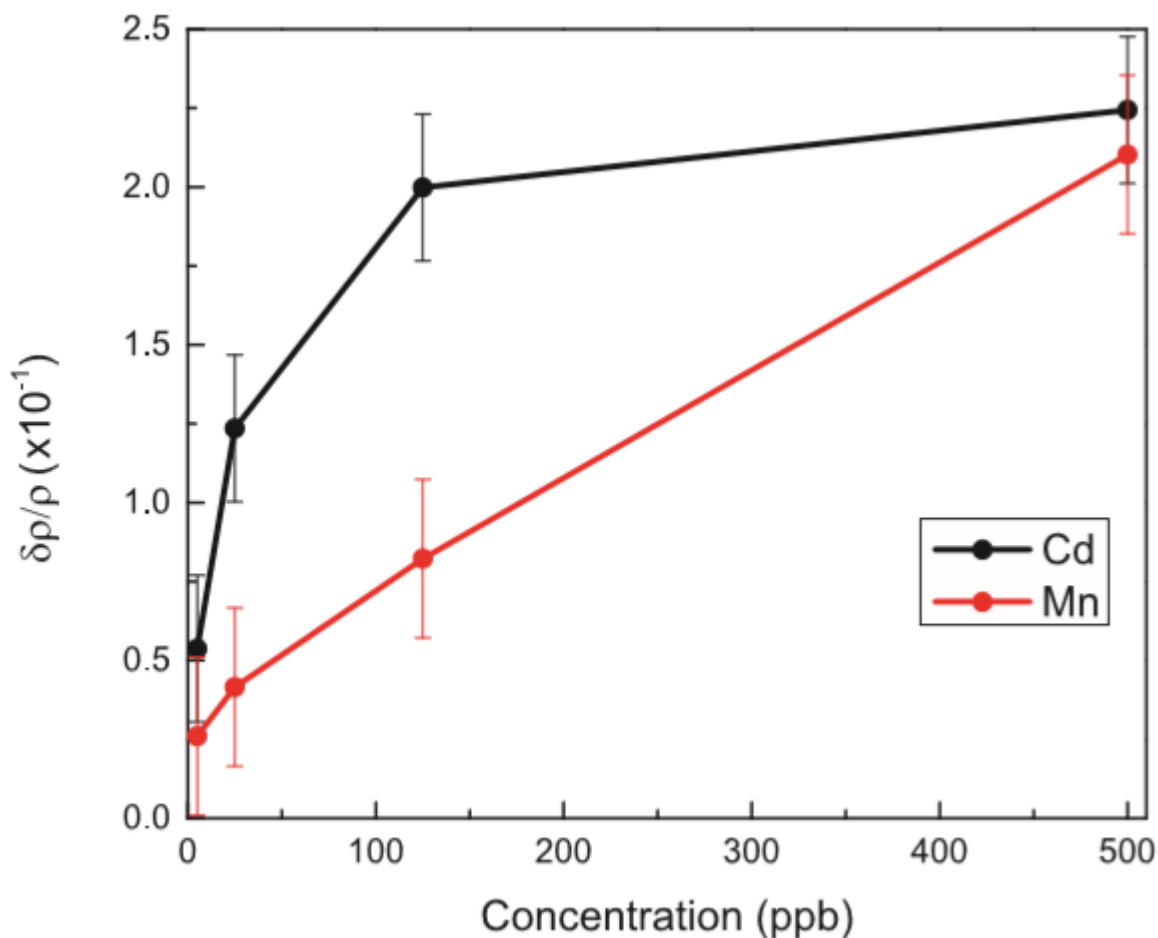


**Figure 3.8: Relative change of resistivity of the sensing system as a function of the concentration of  $\text{Cd}^{2+}$  and manganese  $\text{Mn}^{2+}$  divalent cations in water. Resistivity changes at 5 ppb, 25 ppb, 125 ppb, and 500 ppb concentrations are reported, with a linear regime at low concentrations and a saturation regime at higher concentrations.**

We observe a stark difference in  $\text{Cd}^{2+}$  ion detection performance when comparing high-quality natural vein graphite to the more defective synthetic graphite. This is evident from Fig. 3.9 where current noise from the device incorporating synthetic graphite is much greater, making it less suited to sense  $\text{Cd}^{2+}$  ions with good accuracy. This suggests that natural graphite is superior to its

synthetic counterpart due to higher surface cleanliness, which is consistent with its lower defectiveness, as evident from Raman and EPR measurements discussed in the previous sections.

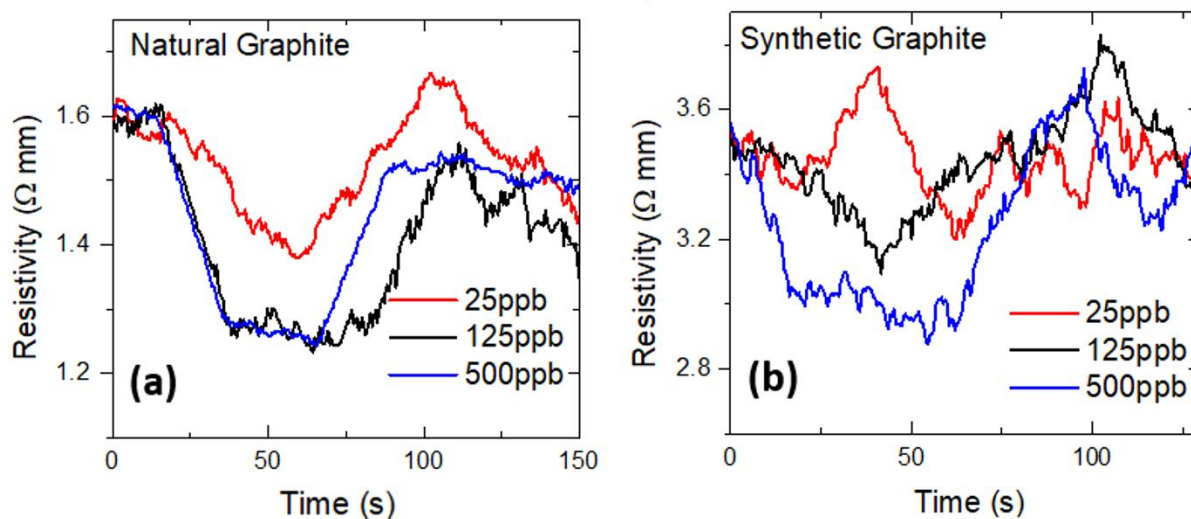


**Figure 3.9: Comparison of the responses to  $\text{Cd}^{2+}$  at different concentrations with sensing systems using multilayer graphene sensing “cakes” prepared from (a) natural graphite and (b) synthetic/turbostratic graphite.**

It is important to understand the reason for high-quality natural graphite to perform better than synthetic graphite and why it is selective to heavy metal ions such as  $\text{Cd}^{2+}$  as opposed to others, such as  $\text{Mn}^{2+}$ . We may infer that lower defectiveness allows for more consistent interlayer spacings between layers and may enhance the performance of natural graphite. The lower surface potential of the natural graphite may cause a change in the distance between individual graphene flakes in the graphite due to exfoliation. Natural graphite’s lower surface potential may allow the copolymer surfactant to intercalate the graphite layers and change the Van der Waals interlayer interactions.

### 3.2.2.1 Effect of Molecular Weight of PEG-PPG-PEG on Sensing Performance

We notice from Fig. 3.10 that the response of the water sensing apparatus is drastically different, depending on the molecular weight and chain length of the PEG-PPG-PEG block copolymer used to exfoliate graphite and remaining within the multilayer graphene cake. The response of the sensing apparatus to the same concentration of  $\text{Cd}^{2+}$  changes with different molecular weight of PEG-PPG-PEG used to exfoliate graphite. The higher the molecular weight of PEG-PPG-PEG being used, the higher the sensitivity to  $\text{Cd}^{2+}$  ions. This leads us to suspect that intercalation of PEG-PPG-PEG at different molecular weight, which has been shown in Fig. 3.5 to produce different c-axis spacing in multilayer graphene, also plays a critical role in trapping  $\text{Cd}^{2+}$  ions between graphene layers, with important effects on the electrical properties of their active layer, with an important role in their detectability.

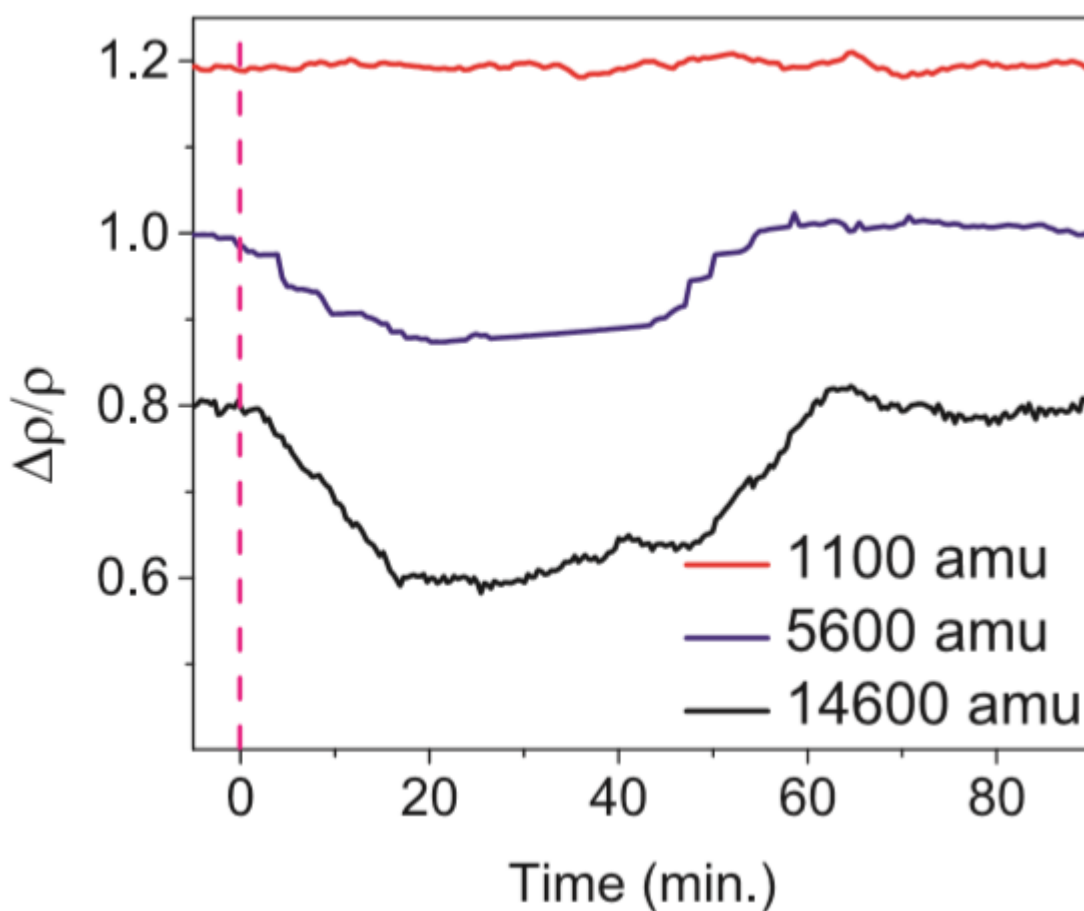


**Figure 3.10: Response of chemiresistors prepared with varying PEG-PPG-PEG molecular weight using natural hydrothermal vein graphite. Data refer to the insertion of 125 ppb of cadmium in water. It can be observed that Mn=14,600 amu lead to the best sensing performance.**

Fig. 3.11 demonstrates the change in volume of multi-layer graphene exfoliated from different surfactants relative to the corresponding volume of natural graphite being used. The change in volume has been calculated using Archimedes' law once the surfactant volume has been subtracted. From Fig. 3.11, it is apparent that the molecular weight of PEG-PPG-PEG has a significant effect on the volume of exfoliated multi layer graphene and, consequently, its c-axis spacing. Samples have been exfoliated from the same type of graphite. This corroborates our hypothesis about the effect of molecular weight of PEG-PPG-PEG on the ability to tune the c-axis spacing, selectively capture  $\text{Cd}^{2+}$  ions in the interlayer, and, therefore, affect the selectiveness of the sensor sensing performance.

Combining the results from Figs. 3.5, 3.10, and 3.11 it becomes apparent that the c-axis spacing in multilayer graphene need to be carefully adjusted in order to maximize the sensitivity to specific ions in a sensing apparatus. Low molecular weight of PEG-PPG-PEG causes an excessive c-axis spacing for  $\text{Cd}^{2+}$  intercalation and sensing, whereas an excessive molecular weight PEG-PPG-PEG (14,600 amu) may result in a too large c-axis spacing for  $\text{Cd}^{2+}$  ion trapping and, subsequently, in too little ion concentration to affect the chemiresistor's electrical properties.

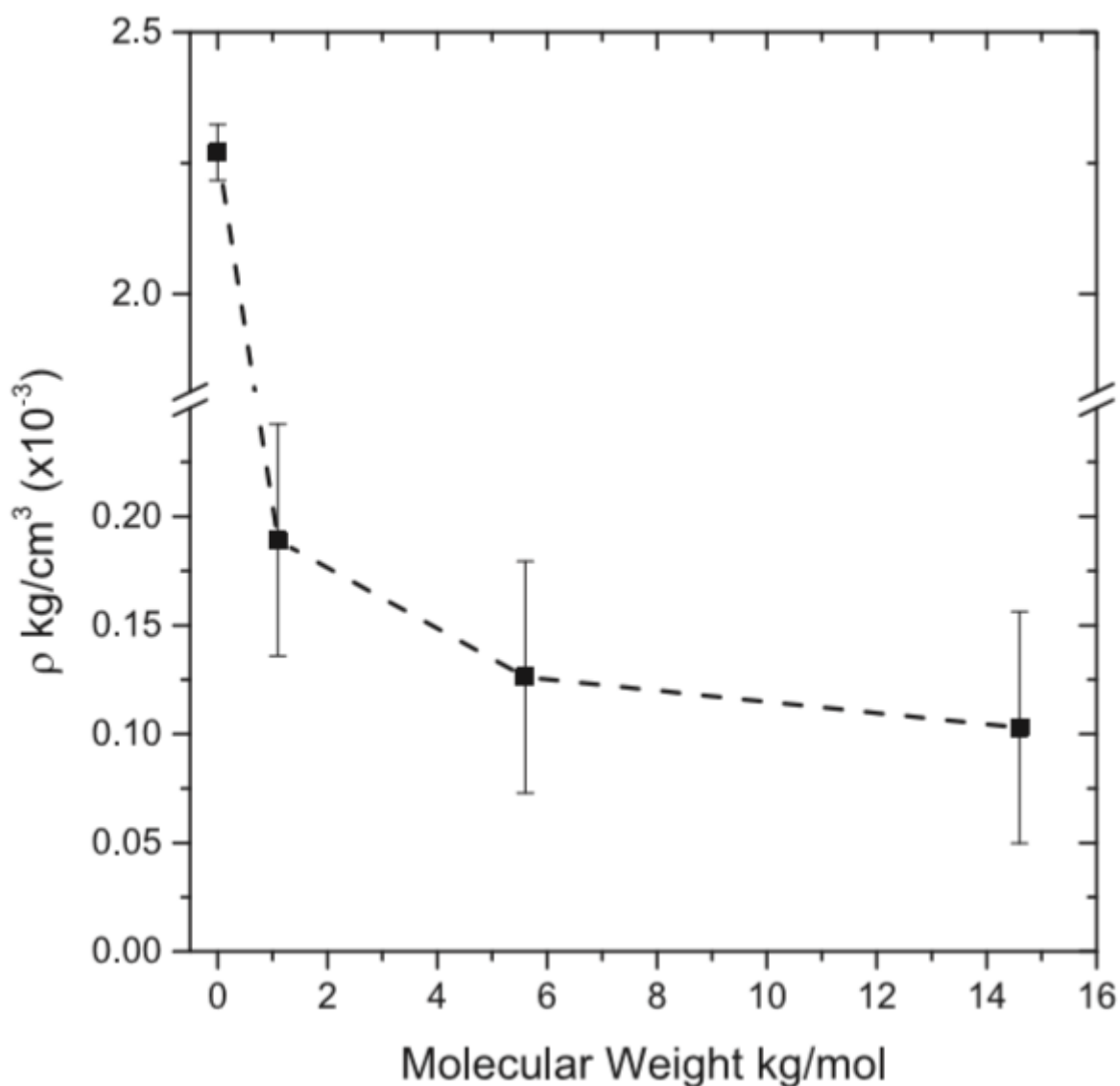


**Figure 3.11. Density and volume changes of multilayer graphene “cakes” as a function of the molecular weight of PEG-PPG-PEG copolymer used to exfoliate graphite, indicating that the molecular weight has effects on the multilayer graphene density and, therefore, on the interlayer spacing distance. Data refer to multi-layer graphene exfoliated from hydrothermal vein graphite.**

### 3.4 Conclusion

There are many methods to date to detect cadmium in water, these include various spectroscopic and electrochemical techniques. These methods are difficult and expensive to execute. This paper demonstrates a novel method of detecting low concentrations of cadmium ions in water. This method, unlike many comparable methods allows for low cost and ease of use without the need for off site trained personnel. The method allows aqueous cadmium to pass through a small gap cell (in the solid-state) containing graphite which both filters and senses cadmium.

Simultaneously, a data acquisition kit creates IV curves and computes the resistivity of the gap cell. This paper has also demonstrated that natural graphite at low defectiveness is superior to more defective synthetic graphite for sensing cadmium in the chemiresistor architecture proposed in this study. We also note that the molecular weight of the polymer used to exfoliate graphite is able to affect the sensitivity to specific metal ion contaminants. Although our paper is a proof-of-concept study, a variety of metal ions can be tested in further studies.

## References

- [1] Y. K. Siong, M. Atabaki and J. Idris, *Water Resources*, **2013**
- [2] G. Aragay, J. Pons and A. Merkoçi, *Chemical Reviews*, **2011**, 111 (5), 3433-3458
- [3] J. W. Hamilton, R. C. Kaltreider, O. V. Bajenova, M. A. Ihnat, J. McCaffrey, B. W. Turpie, E. E. Rowell, J. Oh, M. J. Nemeth, C. A. Pesce, and J. P. Lariviere, *Environmental Health Perspectives*, **1998**, 106, 1005-1015
- [4] B. L. Vallee and D. D. Ulmer, *Annual Review of Biochemistry*, **1972**, 41 (1), 91-128
- [5] T. Partanen, P. Heikkila, S. Hernberg, T. Kauppinen, G. Moneta and A. Ojajarvi, *Scandinavian Journal of Work, Environment & Health*, **1991**, (4), 231-239
- [6] M. Jaishankar, T. Tseten, N. Anbalagan, B. B. Mathew and K. N. Beeregowda, *Interdisciplinary toxicology*, **2014**, 7 (2), 60-72
- [7] L. Järup, *British Medical Bulletin*, **2003**, 68 (1), 167-182
- [8] J. Park, P. Bazylewski and G. Fanchini, *Nanoscale*, **2016**, 8 (18), 9563-9571
- [9] L. B. Allen, P. H. Siitonen, H. C. Thompson, *Journal of Agricultural and Food Chemistry*, **1997**, 45 (1), 162-165
- [10] J. Gasparik, D. Vladarova, M. Capcarova, P. Smehyl, J. Slamecka, P. Garaj, R. Stawarz and P. Massanyi, *Journal of Environmental Science and Health, Part A*, **2010**, 45 (7), 818-823
- [11] A. T. Townsend, K. A. Miller, S. McLean and S. Aldous, *Journal of Analytical Atomic Spectrometry*, **1998**, 13 (11), 1213-1219
- [12] R. Flamini and A. Panighel, *Mass Spectrometry Reviews*, **2006**, 25 (5), 741-774
- [13] X. Chai, L. Zhang and Y. Tian, *Analytical Chemistry*, **2014**, 86 (21), 10668-10673
- [14] G.-L. Liu, J.-F. Wang, Z.-Y. Li, S.-Z. Liang and X.-N. Wang, *Biomedical and Environmental Sciences*, **2009**, 22 (3), 188-193

- [15] M. Hua, S. Zhang, B. Pan, W. Zhang, L. Lv and Q. Zhang, *Journal of Hazardous Materials*, **2012**, 211-212, 317-331
- [16] B. Bansod, T. Kumar, R. Thakur, S. Rana and I. Singh, *Biosensors and Bioelectronics*, **2017**, 94, 443-455
- [17] L. Pujol, D. Evrard, K. Groenen-Serrano, M. Freyssinier, A. Ruffien-Cizsak and P. Gros, *Frontiers in chemistry*, **2014**, **2**, 19-19
- [18] P. Bazylewski, S. Van Middelkoop, R. Divigalpitiya and G. Fanchini, *FlatChem*, **2018**, 11, 15-23
- [19] J.-W.T. Seo, A.A. Green, A.L. Antaris, M.C. Hersam, *J. Phys. Chem. Lett.*, **2011**, **2**, 1004
- [20] K.S. Novoselov, V.I. Fal'ko, L. Colombo, P.R. Gellert, M.G. Schwab, K. Kim, *Nature*. **2012**, 490, 192
- [21] A.G. Conly, L.C. Moore, 2015, in: G.J Simandl, M. Neetz, (Eds.), Symposium on Strategic and Critical Materials Proceedings, British Columbia Ministry of Energy and Mines, British Columbia Geological Survey, Victoria, BC, Paper 2015-3, p. 173.
- [22] M. Lotya, Y. Hernandez, P.J. King, R.J. Smith, V. Nicolosi, L.S. Karlsson, F.M. Blighe, S. De, Z. Wang, I.T. McGovern, G.S. Duesberg, J.N. Coleman, *JACS*, **2009**, 131, 3611–3620.
- [23] A.C. Ferrari, J. Robertson, *Phys. Rev. B*, **2000**, 61, 14095–14107
- [24] J. Kausteklis, P. Cevc, D. Arčon, L. Nasi, D. Pontiroli, M. Mazzani, M. Riccò, *Phys. Rev. B*, **2011**, 84, 125406.
- [25] G.M. Arnold, *Carbon*, **1967**, 5, 33–42.
- [26] G.E. Bacon, *Acta Crystallogr.*, **1951**, 4, 558–561

## Chapter 4

### 4.1 Introduction

There is a recognized need for cost effective methods to both sense contaminants and purify contaminated water sources, which has driven rapid advancements in thin film water filtration, waste water utilization, and contaminant sensing [1], [2]. Graphene has been implemented successfully as a water filtration material due to low cost, availability, ease of use and versatility of graphene-based thin film membranes and graphene oxide sorbents [1], [3]. Molybdenum disulfide ( $\text{MoS}_2$ ) is a highly investigated material that possesses a layered structure similar to graphite.  $\text{MoS}_2$  can be exfoliated into few-layer platelets, but with electrical and structural properties significantly different from graphene [4], [5]. Where graphene and thin graphite films are zero-band gap or semi metallic materials,  $\text{MoS}_2$  is an intrinsic semiconductor with a direct bandgap of 1.95 eV and an indirect band gap of 1.2 eV [6]. When exfoliated into few layer platelets, the properties of  $\text{MoS}_2$  depend highly on the number of the  $\text{MoS}_2$  layers as well as their stacking, and on the attachment of specific functional groups [6], [7]. The semiconducting property of  $\text{MoS}_2$  opens new avenues towards its use as a tool for removal and high-sensitivity detection of metal contaminants in water.

A variety of trace metals in water have been identified to have toxicological or carcinogenic effects in humans. Specifically,  $\text{Hg}^{2+}$ ,  $\text{Pb}^{2+}$ ,  $\text{As}^{3+}$  affect the central nervous system, while  $\text{Cu}^{2+}$ ,  $\text{Cd}^{2+}$ ,  $\text{Hg}^{2+}$ ,  $\text{Pb}^{2+}$  target kidneys and liver and  $\text{Ni}^{2+}$ ,  $\text{Cu}^{2+}$ ,  $\text{Cd}^{2+}$ ,  $\text{Cr}^{3+}$  have detrimental effects on skin, bones, and teeth [8], [9], [10], [11]. Ingestion of these metals through water consumption is cumulative and can cause serious health problems even when present in ppb levels. Both capture and detection of these metals from water are priorities at the industrial

and residential levels. Current standard detection techniques to trace heavy metals in water down to the part-per-trillion (ppt) range include atomic absorption spectroscopy [12], inductively coupled plasma-mass spectrometry, mass spectroscopy [13], [14], and X-ray fluorescence [15]. High detection limits with lower complexity can be achieved with enhanced materials such as metal–organic frameworks [16], DNA-based biosensors [17], electrochemical sensors [18], [19], metal oxide nanoparticles [20], [21], and more recently using layered materials including graphite, graphene, graphene oxide, and MoS<sub>2</sub> [22], [23], [24], [25]. Nano structured materials can offer higher detection limits with reduced complexity due to a high surface area and may be conducting or semiconducting. MoS<sub>2</sub> field effect transistors have been demonstrated that make use of the semiconducting band gap in MoS<sub>2</sub> and have been used to sense Ag<sup>2+</sup> or arsenite ions absorbed onto the device surface and detected through changes in current–voltage characteristics [25]. However, MoS<sub>2</sub> for detection of heavy metals in water has not been realized.

Absorption and by extension chemical sensing of Cd can be accomplished using thiol containing small molecules such as L-cysteine. L-Cysteine has been used as both a fabrication aid and as a coating shell for metal nanoparticles [26], [27], due to the high affinity of the thiol group for metal ions. L-cysteine has been used to coordinate the growth of PbS and CdS nanowires and nanoparticles, respectively, by providing the sulphur source to nucleate growth [26], [27]. The thiol group is highly sensitive to divalent metal ions, allowing L-cysteine to cover the nanoparticle surface as a shell that modifies the size and chemical properties of the nanoparticles. In the case of CdS, applying a shell of L-cysteine reduces the toxic effects of Cd to aquatic plant life [28]. The metal-coordinating abilities of L-cysteine in aqueous environments can be translated to metal ion absorption on an L-cysteine functionalized filtration membrane.

In this article, the fabrication of MoS<sub>2</sub> nanosheets functionalized with L-cysteine by an amide cross-linking reaction is reported for the first time, combined with extensive characterization of their structural and water purification properties. Aqueous suspensions of functionalized MoS<sub>2</sub> nanosheets prepared by this method and deposited as thin film membranes are capable of absorbing up to  $76 \pm 15$  mg Cd<sup>2+</sup> per gram of membrane material, while showing minimal absorption of other divalent metals under identical conditions. The addition of L-cysteine to the membranes sensitizes them to preferentially capture Cd<sup>2+</sup> ions, making MoS<sub>2</sub>-Cys nanosheets ideal for selective absorption and detection of dilute cadmium ions in water.

## 4.2 Experimental

### 4.2.1 Exfoliated MoS<sub>2</sub>

Microcrystalline MoS<sub>2</sub> powder (Sigma Aldrich, CAS 1317-33-5, average 6  $\mu$ m, max. 40  $\mu$ m) was used as a precursor to prepare exfoliated MoS<sub>2</sub> nanosheets functionalized with carboxyl groups (MoS<sub>2</sub>-COOH). 600 mg of MoS<sub>2</sub> powder was combined with 3 mL of thioglycolic acid (Sigma Aldrich, CAS 68-11-1) and stirred for 24 hrs at room temperature. After stirring, 30 mL of distilled water (pH = 3.3) was added to the mixture, followed by sonication for 2 hrs. After sonicating, the mixture was allowed to rest and sediment at room temperature for 48 h. The top 2/3 of the final MoS<sub>2</sub>-COOH solution without sediment was decanted to a clean glass bottle, producing a final solution containing 3 g/L on average of MoS<sub>2</sub> determined by weighing the sediment, with pH = 2.7.

### 4.2.2 Cysteine Functionalization

MoS<sub>2</sub>-COOH was functionalized with L-cysteine (Sigma Aldrich, CAS 59–90-4) using an amide cross-linking reaction. The pH of the MoS<sub>2</sub>-COOH suspension was adjusted to 4.0–5.0 using ammonium hydroxide. N-(3-Dimethyl-aminopropyl)-N'-ethylcarbodiimide hydrochloride (EDC, Sigma Aldrich, CAS 25952-53-8) was added to the MoS<sub>2</sub>-COOH solution in 1:1 and 1:10 mass ratios. Subsequently, N-Hydroxysuccinimide (NHS, Sigma Aldrich, CAS 6066-82-6) was added to the solution in 1:1.5 and 1:15 mass ratios over MoS<sub>2</sub>, and the mixture was stirred for 15 mins. A separate solution of L-cysteine in water was prepared at a pH of 6.0–7.0. The two solutions of MoS<sub>2</sub>-COOH and the L-cysteine were then combined using 1:1 and 1:10 mass ratios and stirred for 2 h at room temperature to carry out the functionalization procedure. Fig. 4.1 presents a schematic of this procedure. Thin film membranes were prepared by vacuum filtration onto polyether sulfone (PES, 3M Canada Co.) porous support backing membranes with a nominal pore size of 200 nm, followed by washing in a distilled water bath, and drying at 50 °C in air. The final masses per volume of solution of MoS<sub>2</sub>-Cys deposited on the membranes were 0.12 g/50 mL, 0.10 g/40 mL, 0.07 g/30 mL and 0.05 g/20 mL. Reported pH values were measured using an ECOPHTEST2 pH Tester, and water conductivity was measured using an Omega CBD-387 ionic conductivity meter. The filter masses were determined by weighing the PES filter backing before and after deposition of MoS<sub>2</sub>. Filtration membranes with 1:10 MoS<sub>2</sub>:Cys mass ratio were used for thermal gravimetric analysis, all other analyses were conducted with a 1:1 mass ratio.

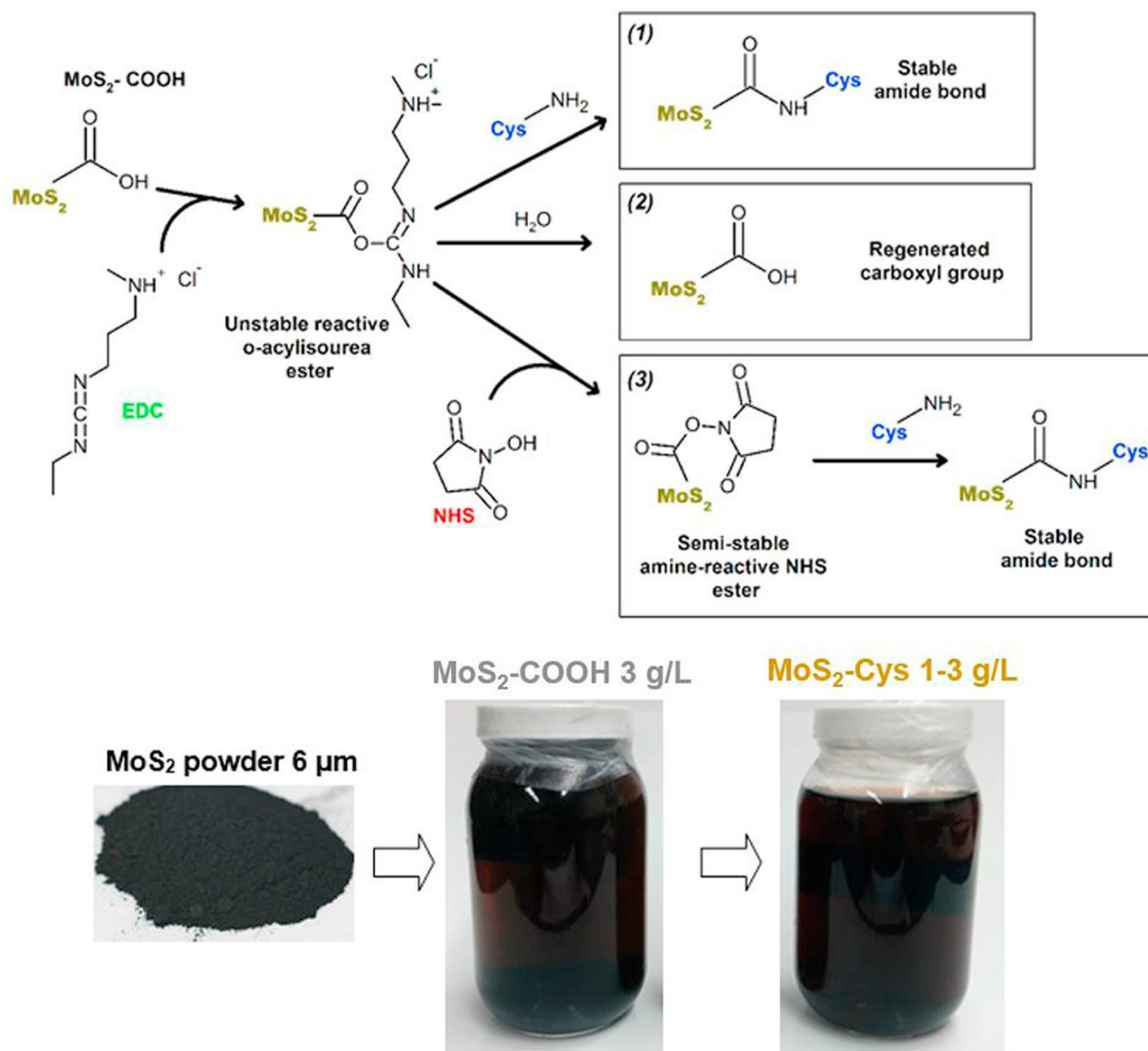


**Figure 4.1:** Scheme of the process used to functionalize MoS<sub>2</sub> – COOH with L-cysteine. Three possible reaction pathways that may result in a stable amide bond or a regenerated carboxyl group are indicated. NHS is used to stabilize the reaction a prevent quenching of the intermediate ester and subsequent regeneration of the carboxyl group, such that reaction pathway (3) dominates. Images of the MoS<sub>2</sub>-COOH and MoS<sub>2</sub>-Cys solutions after sedimentation are shown.

MoS<sub>2</sub>-COOH nanosheets dispersed in water at high concentration are ideal platforms for additional functionalization processes due to the intriguing chemistry enabled by carboxyl groups at their edges and defect sites on the surface [29]. Fig. 4.1 demonstrates a functionalization process in which COOH groups can be used to covalently attach L-cysteine to the MoS<sub>2</sub> backbone. Although the paradigm of amide-cross linking reactions is quite general, it has not been explored in the context of MoS<sub>2</sub> functionalization for selective metal absorption. L-cysteine attachment has been achieved through amide cross linking using N-(3-Dimethylaminopropyl)-N'-ethylcarbodiimide hydrochloride (EDC), with N-Hydroxysuccinimide (NHS) playing the role of a stabilizer. This procedure starts with MoS<sub>2</sub>-COOH nanosheets suspended in water. Subsequently, EDC is used as an amide cross-linker as it is stable in aqueous solutions. Cross-linking with L-cysteine using EDC has two competing outcomes that are illustrated in Fig. 4.1: (1) either a stable amide bond is created, or (2) the carboxyl group is regenerated through hydrolysis. To prevent the competing hydrolysis reaction, NHS is used to stabilize the intermediate reaction component. A reaction pathway as in Fig. 4.1, scheme (3) has been targeted. This process uses NHS to obtain nanosheets of MoS<sub>2</sub> functionalized with L-cysteine in an aqueous environment.

#### 4.2.3 Raman/FTIR/UV-Vis characterization

Unpolarised Raman spectra were recorded in the 100–3200 cm<sup>-1</sup> spectral region on a Renishaw InVia spectroscope equipped with a Leica DM2600M microscope and a 50x objective in a backscattering arrangement. A 633 nm helium–neon laser with a maximum output power of 17 mW was used as the excitation source. The power at the sample surface was 0.02 mW/μm<sup>2</sup> across an 8 μm<sup>2</sup> area. Special attention was paid to avoid damage of the sample by the laser by shuttering the laser when not actively measuring. Raman spectra were recorded using a

charged couple device (CCD) array of  $1024 \times 256$  pixels, which was cooled to  $-70$  °C using a Peltier cell. The spectrometer is equipped with a low pass filter for rejection of elastically scattered laser light. Raman measurements were performed on MoS<sub>2</sub> and MoS<sub>2</sub>-Cys samples drop cast from solution onto (1 1 0) silicon wafers. Samples were dried in air on a hot plate at 50 °C until nearly dried, then washed with distilled water. After washing, samples were dried again at 50 °C until all water was visibly evaporated. Fourier Transform Infrared (FTIR) spectroscopy measurements were performed in the 500–4500 cm<sup>-1</sup> spectral region using a Thermo Scientific Nicolet 6700 FT-IR Spectrometer. Samples were drop cast onto (1 1 0) silicon wafers from as-prepared MoS<sub>2</sub> -COOH and MoS<sub>2</sub>-Cys solutions and dried in air on a hot plate at 50 °C until nearly dried, then washed with distilled water. After washing, samples were dried again at 50 °C until the water was visibly evaporated. UV-Vis was conducted in the 250–700 nm range using a Shimadzu UV-1800 UV Spectrophotometer. Measurements were conducted on 3 mL aliquots of MoS<sub>2</sub> -COOH and MoS<sub>2</sub>-Cys solutions as-prepared.

#### 4.2.4 SEM/EDX/AFM/TGA/XRD Characteristics

Scanning electron microscopy (SEM) and Energy-dispersive X-ray spectroscopy(EDX) (Zeiss LEO 1540XB instrument) were used to characterize exfoliated MoS<sub>2</sub> flakes before and after exposure to metal ions. SEM samples were prepared by vacuum filtration onto polycarbonate membranes (pore size 0.5 μm). Samples were coated with 1 nm layer of osmium prior to measurement to increase the surface conductivity using an Os plasma coater (Fl ogen, OPC80T). EDX was performed on prepared membranes after vacuum filtration of MoS<sub>2</sub> or MoS<sub>2</sub>-Cys using silver paste around the edges, but without osmium coating on the surface. Tapping-mode atomic force microscopy (AFM) images using silicon tips with 75 KHz resonance frequency and 2.8 N/m force constant were recorded on the same samples (without Os

coating) using a Witec Alpha300S AFM microscope. Scanned areas were  $1.5 \mu\text{m}^2$  and  $5 \mu\text{m}^2$ . Thermal gravimetric analysis (TGA) was conducted in air with a heating rate of  $20 \text{ }^\circ\text{C}/\text{min}$  up to a final temperature of  $550 \text{ }^\circ\text{C}$  using a TA Instruments Q50 TGA Thermogravimetric Analyzer. Samples for TGA consisted of circular membranes approximately 5 mm in diameter that were stamped from MoS<sub>2</sub>-Cys/PES membranes prepared by vacuum filtration of 50 mL of MoS<sub>2</sub>-Cys (1:10 ratio) solution. Two membranes were exposed to metal ions by soaking for 24 hrs in 50 ppm solutions of either Cd<sup>2+</sup> or Mn<sup>2+</sup> ions. Powder X-ray diffractometry (XRD) was performed using an Inel CPS diffractometer equipped with a Cu K $\alpha$  X-ray source. Powder samples (0.2 g) were prepared by filtration of MoS<sub>2</sub>-COOH and MoS<sub>2</sub>-Cys suspensions through 0.22  $\mu\text{m}$  filters, followed by drying at  $70 \text{ }^\circ\text{C}$  in air until a dry powder was obtained.

## 4.3 Results and Discussion

### 4.3.1 MoS<sub>2</sub> Nanosheet Characterization

Exfoliated MoS<sub>2</sub> nanosheets possess a high surface area and high density of edges that provide a large number of sites for functionalization or absorption. MoS<sub>2</sub> nanosheets were prepared by first exfoliating MoS<sub>2</sub> powder by stirring with thioglycolic acid to introduce oxygen functional groups. The process results in a large number of nanosheets functionalized with carboxylic acid groups, with a high density along their edges [29]. These nanosheets can be further dispersed in water to produce a highly concentrated MoS<sub>2</sub>-COOH ink that is stable over long periods of time. The structure of these nanosheets is shown in Fig. 4.2 and was investigated by atomic force microscopy (AFM) and scanning electron microscopy (SEM) after vacuum filtration of solution onto a track-etched polycarbonate membrane. The nanosheets are revealed to be flat and uniform, with a lateral size ranging from 100 to 300 nm. AFM micrographs find the flakes to be significantly exfoliated down from large microcrystalline grains in the starting powder ( $6 \mu\text{m}$

average) to 10–20 layer-thick nanosheets. AFM images before and after functionalization (see Fig. A1) indicate the lateral size of the flakes increases, on average to 200–450 nm after functionalization, to be compared with 100–300 nm before the functionalization process. This suggests that not all of the L-cysteine molecules are chemically attached to MoS<sub>2</sub>, but a fraction of them are adsorbed at the edges or on the surface of the flakes.

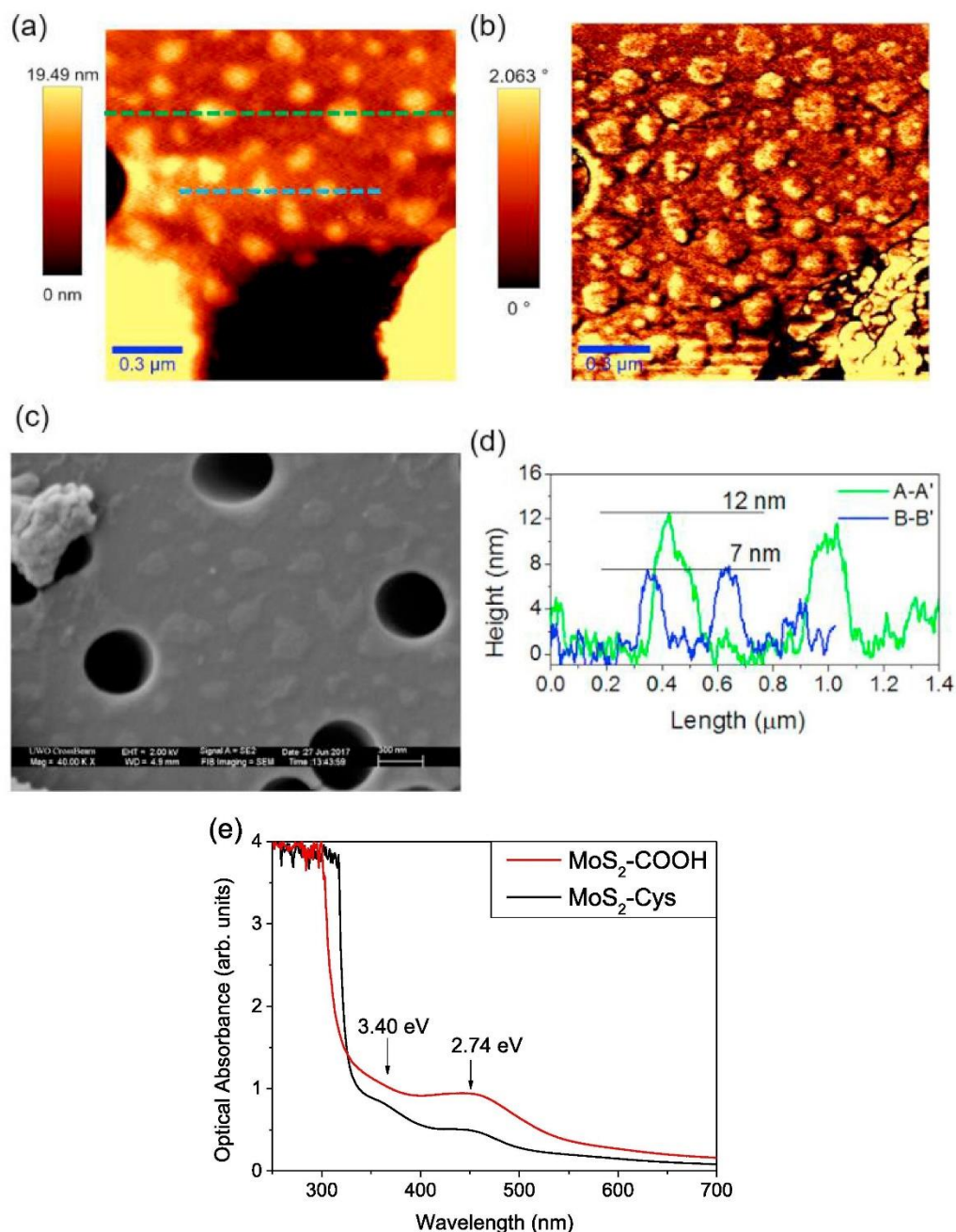


**Figure 4.2: Characterization of thioglycolic acid-exfoliated MoS<sub>2</sub> flakes: (a) Tapping mode AFM topography and (b) phase images Comparison of AFM images for MoS<sub>2</sub>-COOH filtrated onto polycarbonate membranes. (c) An SEM image of MoS<sub>2</sub> flakes filtrated onto a track etched polycarbonate membrane shows small flakes ranging from 100 to 300 nm in diameter. (d) AFM cross sections, showing that the thickness of MoS<sub>2</sub> flakes prior to functionalization with L-cysteine is in the 7–12 nm range, with an average height of  $10 \pm 1$  nm. (e) UV–Vis spectra of MoS<sub>2</sub>-COOH and MoS<sub>2</sub>-Cys water solutions, identifying two blue-shifted excitonic peaks.**

The optical properties of MoS<sub>2</sub> before and after functionalization were investigated as shown in Fig. 4.2(e) using UV–Vis spectroscopy. The concentration of MoS<sub>2</sub>-COOH as prepared is approximately 3 g/L as determined by weighing the sediment, and the UV–Vis absorbance intensity at 450 nm is consistent with this value when compared to MoS<sub>2</sub> nanosheets suspended in water that appear in the literature [30]. MoS<sub>2</sub> without chemical treatment possesses two well-known excitonic peaks, *A* and *B*, appearing in the 600–700 nm range [31]. In this case, these peaks are replaced with a pair of features significantly blue shifted to roughly 450 nm (3.40 eV) and 370 nm (2.74 eV). A blue shift of the *A* and *B* excitonic peaks to lower wavelength has been observed due to quantum confinement when MoS<sub>2</sub> has been exfoliated into nanosheets [31]. This result qualitatively confirms the result obtained from AFM scans, indicating that MoS<sub>2</sub> nanosheets are in fact present in solution before and after functionalization.

Fig. 4.3 presents the Raman spectra of MoS<sub>2</sub> nanosheets before and after L-cysteine functionalization. Assignment of Raman-active vibrations for both MoS<sub>2</sub> and L-cysteine is listed in Table 1, and was made according to Refs. 29, 32–35. From the spectrum before functionalization, numerous Raman peaks, typical of the MoS<sub>2</sub> backbone, can be identified

(see Fig. 3(a), red curve). These peaks include bands that are visible due to excitation by the 633-nm wavelength Raman laser [32], [33]. The use of a relatively long excitation wavelength, in the red photon energy range, affords a unique view of the vibrational spectrum of MoS<sub>2</sub> due to strong absorption at room temperature that is resonant with the direct band gap of this material ( $E_{\text{gap}} = 1.95$  eV, corresponding to 635.9 nm) [32]. Additional Raman spectra corroborating these assignments are reported in Fig. S2 of the Supplementary Information. Frequency, shape, and intensity of these vibrations are consistent with MoS<sub>2</sub> flakes with thickness of 10 layers or greater [32]. Fig. 4.3(a) also shows a broad peak centered at  $1595\text{ cm}^{-1}$ , which can be assigned to the C=O stretching mode from carboxyl groups attached to MoS<sub>2</sub>. Several low-intensity peaks in the  $750\text{--}900\text{ cm}^{-1}$  frequency range are documented in the literature [33]. They are known to arise from higher molybdenum oxides (e.g. MoO<sub>3</sub>, Mo<sub>4</sub>O<sub>11</sub>) which are expected from the exfoliation process [29]. After copious washing of the samples with water, no trace of hydrocarbon (CH<sub>n</sub>) stretching bands from thioglycolic acid can be seen above  $2500\text{ cm}^{-1}$ . However, the CH<sub>n</sub> spectral region becomes active again after functionalization, due to the presence of L-cysteine-related vibrations. The shape of the CH<sub>n</sub> peaks, centered at  $2800\text{ cm}^{-1}$ , is the same as in Ref. 35, in which the spectrum of L-cysteine in the presence of water was reported. S-H stretching vibrations, centered at  $2576\text{ cm}^{-1}$ , can be observed in Fig. 4.3(c). The S-H peak is relatively broad, up to  $100\text{ cm}^{-1}$  in width, due to coordination with water [35]. This is an important result, and shows that the thiol chemistry used to exfoliate MoS<sub>2</sub> in the presence of thioglycolic acid can also take place using the thiol group of L-cysteine. Therefore, the presence of the S-H stretching mode after functionalization indicates that a significant number of sulfur-related defect sites present in the MoS<sub>2</sub> starting material have been functionalized by thioglycolic acid [36].

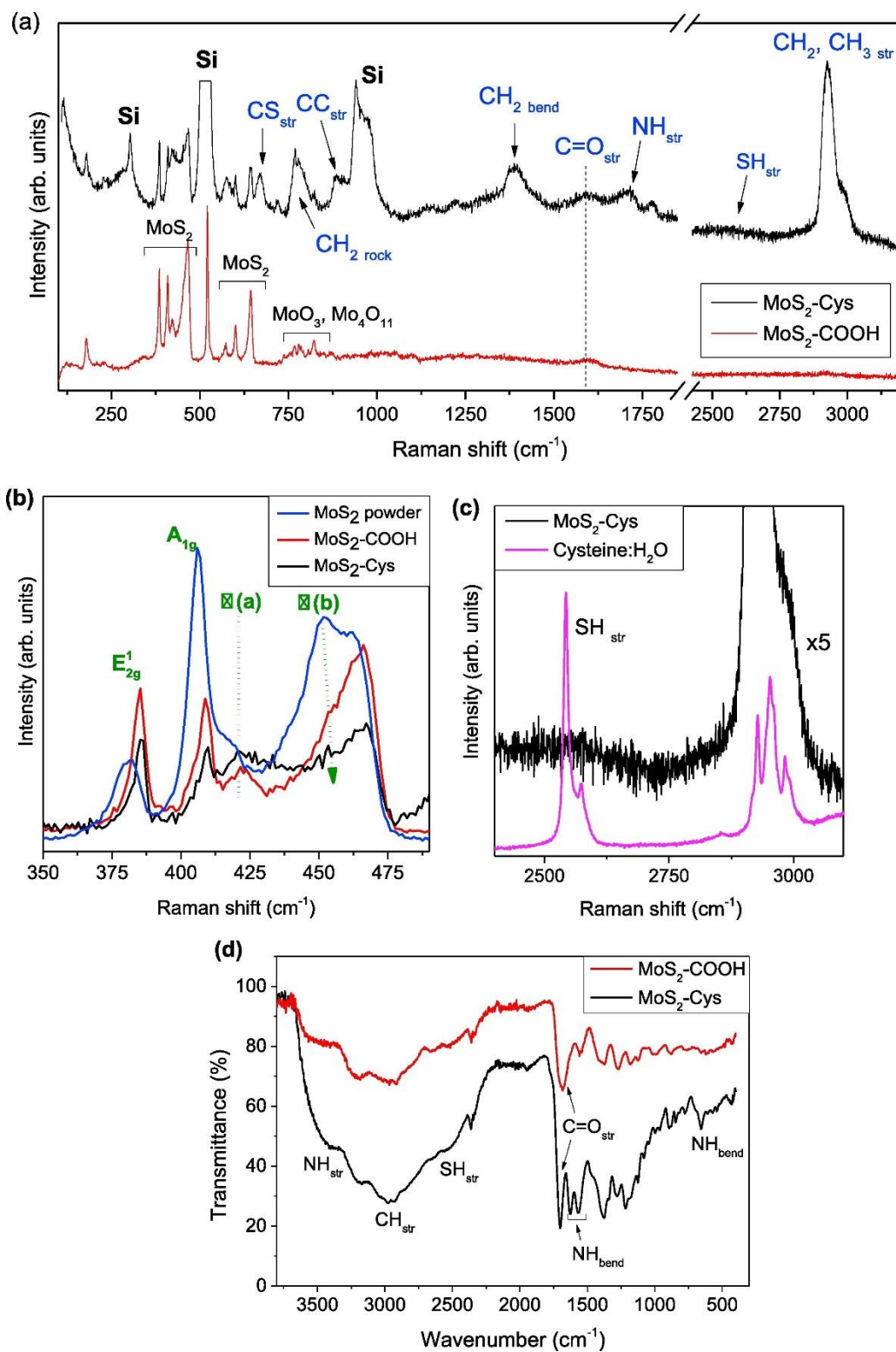


**Figure 4.3: (a) Raman spectra of MoS<sub>2</sub>-COOH compared to MoS<sub>2</sub>-Cys. (b) Characteristic peaks of MoS<sub>2</sub> before and after L-cysteine functionalization. After the addition of L-**

cysteine, characteristic L-cysteine bands are visible in the Raman spectrum. (c) Raman bands representing SH stretching modes in L-cysteine can be identified and they are necessary for the coordination of metal ions. (d) FTIR spectra confirm the results from Raman, showing peaks representing amide bonds between MoS<sub>2</sub> and cysteine.

MoS <sub>2</sub> modes	$\omega$ (cm <sup>-1</sup> )	Cysteine modes	$\omega$ (cm <sup>-1</sup> )
<i>C=O str</i>	1595	<i>CH<sub>3</sub> str</i>	2995
<i>MoO<sub>3</sub> Mo-O str</i>	823	<i>CH<sub>2</sub> str</i>	2935
<i>X</i>	779	<i>CH str</i>	2926
<i>2 x E<sup>1</sup><sub>2g</sub></i>	768	<i>SH str</i>	2576
<i>A<sup>1</sup><sub>1g</sub> (M) + LA(M)<sup>h</sup> (<math>\omega</math>(b)-mode)</i>	644	<i>NH str</i>	1715
<i>E<sup>1</sup><sub>2g</sub> (M) + LA(M)</i>	601	<i>NHS residue</i>	1775
<i>E<sub>1g</sub></i>	573	<i>C=O str</i>	1595
<i>E<sub>2u</sub>(M) + ZA(M)</i>	528	<i>CH<sub>2</sub> bend</i>	1395
<i>E<sub>1g</sub> + XA</i>	466	<i>CH<sub>2</sub> wagg</i>	1216
<i><math>\omega</math>(a)-mode</i>	423	<i>CH<sub>2</sub> twist</i>	1140
<i>S-Mo-S str A<sub>1g</sub></i>	409	<i>CC str</i>	906
<i>S-Mo-S str E<sup>1</sup><sub>2g</sub></i>	385	<i>CC str</i>	885
<i>A<sub>1g</sub>(M)-LA(M)<sup>h</sup></i>	178	<i>CH<sub>2</sub> rock</i>	774
		<i>NHS residue</i>	718
		<i>CS str</i>	671
		<i>SS bend</i>	504

Table 4.1: Experimental Raman peak assignments.  $\omega$ (a)-mode and  $\omega$ (b)-mode refer to notation in Fig. 4.3.

Two other Raman bands, centered at  $1715\text{ cm}^{-1}$  and  $671\text{ cm}^{-1}$ , are signatures of  $\text{NH}_n$  stretching and C-S stretching modes, respectively. They can be assigned to amide bridge groups between  $\text{MoS}_2$  and L-cysteine, confirming that L-cysteine has been chemically attached to  $\text{MoS}_2$  during the process. From AFM measurements after functionalization (see Fig. A1 in the Supplementary Information) the average thickness of the flakes is unchanged after functionalization. This indicates that the  $\text{NH}_n$  stretching vibrations originate from L-cysteine amide bonds on the surface and edges of  $\text{MoS}_2$  flakes, not from amide groups intercalated between  $\text{MoS}_2$  layers. This is also consistent with the XRD analysis (Fig. 4.4). L-cysteine can only be present where a COOH group has already been introduced, and it is unlikely that any COOH groups are present between the  $\text{MoS}_2$  layers. If this were the case the flakes would exfoliate further.

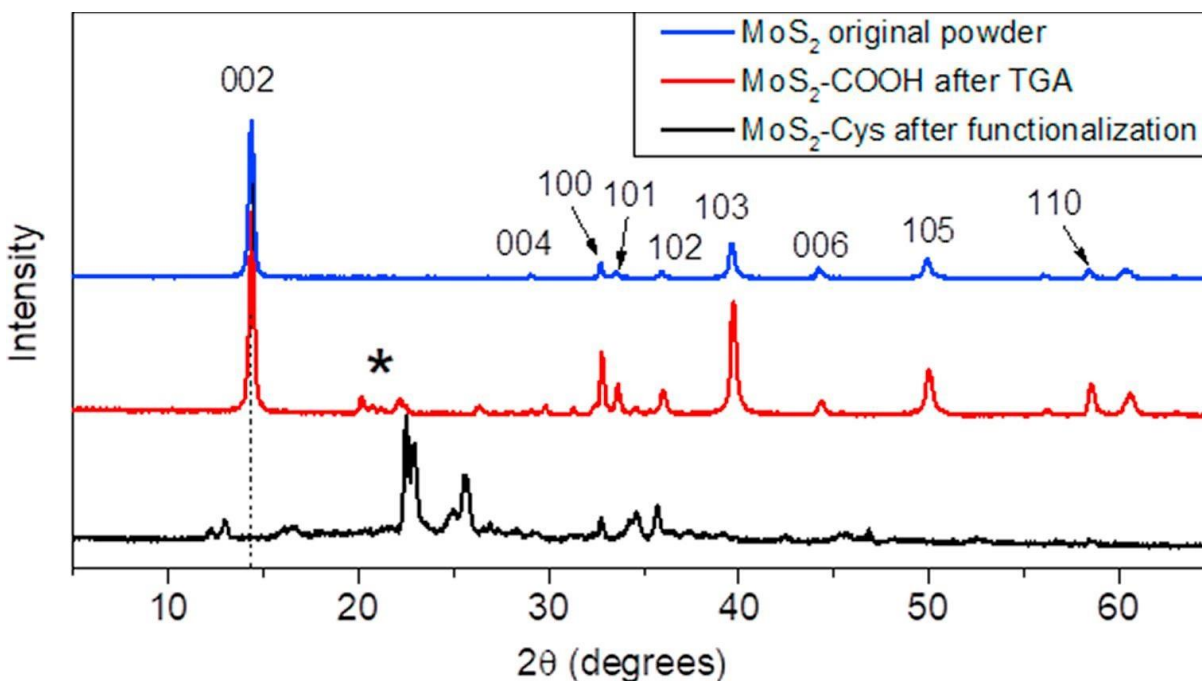


**Figure 4.4: Powder X-ray diffraction patterns of the  $\text{MoS}_2$  original powder (blue line) and powder samples prepared from solution after mixing with thioglycolic acid (red line) and after L-cysteine functionalization (black line).**

Fig. 4.3(b) shows the frequency region with the  $E_{12g}$  and  $A_{1g}$  Mo-S stretching modes characteristic of  $MoS_2$  [34]. Two additional peaks labeled as  $\omega(a)$  and  $\omega(b)$  can be seen in the spectrum of unmodified microcrystalline  $MoS_2$  powder. Peak  $\omega(a)$  is a dispersive mode assigned to two-phonon processes involving out-of-plane vibrations along the c-axis [34]. A relative decrease in intensity of this mode is associated with a decrease in particle thickness during exfoliation. Peak  $\omega(b)$  is associated with the  $2 \times LA(M)$  mode and can no longer be resolved after exfoliation due to the decrease in particle size from micron size to the nanoscale. After functionalization with L-cysteine, minimal changes are apparent in both the line shape and positions of these  $MoS_2$  peaks. Minimal changes to the Mo-S stretching modes after functionalization indicate that the  $MoS_2$  has not been further exfoliated by L-cysteine.

To verify the chemical functionalization of  $MoS_2$ , FTIR measurements were carried out as shown in Fig. 4.3(d), with experimental peak assignments tabulated in Table 2. The assignments in this table were made according to Refs. 29, 37. Before functionalization with cysteine,  $MoS_2$ -COOH displays the expected Mo-S stretching peak indicating  $MoS_2$  at  $480\text{ cm}^{-1}$ , and C=O stretching at  $1687\text{ cm}^{-1}$  originating from the carboxylic acid that has been introduced [37]. Peaks in the range of  $1200\text{--}1550\text{ cm}^{-1}$  can be assigned to thioglycolic acid residue that has not been completely removed by washing. After cysteine functionalization two prominent features appear at  $1567\text{ cm}^{-1}$  and  $1627\text{ cm}^{-1}$  indicating secondary amide groups where cysteine is attached to  $MoS_2$ . The C=O stretching feature is retained after functionalization, but with a slight red-shift as the contributions from this vibration are carboxylic acid groups on cysteine as well as residuals on the  $MoS_2$  that have not reacted with cysteine. An SH stretching vibration can also be seen at  $2550\text{ cm}^{-1}$  arising from thiol groups contributed by cysteine, as well as a large, broad

shoulder at  $3371\text{ cm}^{-1}$  representing the NH stretching mode. Combined with the Raman data, FTIR confirms that  $\text{MoS}_2$  has been successfully functionalized with cysteine (Table 4.3).

<b>MoS<sub>2</sub>-COOH modes</b>	<b><math>\omega</math> (cm<sup>-1</sup>)</b>	<b>MoS<sub>2</sub>-Cys modes</b>	<b><math>\omega</math> (cm<sup>-1</sup>)</b>
<i>Mo-S<sub>str</sub></i>	480	<i>NH out-of-plane bend</i>	657
<i>Thioglycolic acid residue</i>	1276	<i>C—O<sub>str</sub></i>	1215
<i>Thioglycolic acid residue</i>	1392	<i>CH<sub>2</sub>, CH<sub>3</sub>bend</i>	1385
<i>Thioglycolic acid residue</i>	1554	<i>NH in-plane bend</i>	1567
<i>C=O<sub>str</sub></i>	1687	<i>NH in-plane bend</i>	1627
<i>CH<sub>str</sub></i>	2921	<i>C=O<sub>str</sub></i>	1700
<i>CH<sub>str</sub></i>	2975	<i>SH<sub>str</sub></i>	2550
		<i>CH<sub>str</sub></i>	2921
		<i>CH<sub>str</sub></i>	2975
		<i>NH<sub>str</sub></i>	3371

**Table 4.2: Experimental FTIR peak assignments**

<b>Element</b>	<b>Weight %</b>	<b>Atomic %</b>
C K	65.3	73.27
O K	28.92	24.54
Al K	0.49	0.24
Si K	0.29	0.14
S K	2.21	0.92
Mo L	1.87	0.78
Ag L	0.66	0.08
Cd L	0.25	0.03

**Table 4.3: Elemental atomic and weight composition of Cysteine functionalized MoS<sub>2</sub> nanosheets determined from analysis of the EDX spectra shown in Fig. 4.5.**

In order to gain insight into the MoS<sub>2</sub> and interlayer spacing rotational order of stacked MoS<sub>2</sub> sheets after functionalization, powder X-ray diffraction patterns were collected before and after functionalization, as shown in Fig. 4.4. The XRD pattern of the as-received MoS<sub>2</sub> powder displays all of the peaks that were previously reported for MoS<sub>2</sub> [38], [39]. The position of the (0 0 2) peak indicates an interlayer distance of  $c = 6.2 \pm 0.1 \text{ \AA}$  with prominent (1 0 3) and (1 0 5) peaks showing rotational ordering of the MoS<sub>2</sub> layers [39]. In addition, the (1 1 0) peak can be used to calculate the a-spacing to be  $3.26 \pm 0.02 \text{ \AA}$  for all three samples, larger than the reported value of  $3.16 \text{ \AA}$  for single crystal MoS<sub>2</sub> [39]. After treatment with thioglycolic acid, COOH groups have been introduced and the MoS<sub>2</sub> has been exfoliated in flakes thicker than 10 layers. All peaks observed in the MoS<sub>2</sub> starting material are reproduced in the exfoliated material, as well as a new set of signals centered around  $22^\circ$  marked with a (\*) in Fig. 4 that are assigned to disorder introduced by the exfoliation process. The reproduction of XRD peaks from the original powder after exfoliation indicates that the MoS<sub>2</sub> flakes are functionalized with COOH primarily at edge sites, while the disorder peaks (\*) appear due to COOH groups present on the flat surface of the flakes at defect sites.

The XRD patterns change significantly when MoS<sub>2</sub> is functionalized with L-cysteine, with several new sets of peaks appearing, as shown in Fig. 4.4. Two new sets of peaks, centered at  $12^\circ$  and  $16^\circ$ , are assigned to (0 0 1) and (0 0 2) reflections between MoS<sub>2</sub> layers that have become separated after functionalization. The position of two broad peaks at  $12.2^\circ$  and  $12.9^\circ$  indicate a spacing between Mo layers of MoS<sub>2</sub>-Cys =  $7.2 \pm 0.1 \text{ \AA}$  which is larger than the spacing in unmodified MoS<sub>2</sub>, while the a-spacing remains unchanged. Given the van der Waals diameter of

a water molecule is approximately 2.8 Å, the larger spacing is not sufficient to accommodate water molecules or relatively large functional groups, including COOH or L-cysteine. Conversely, the presence of two broad peaks implies that the MoS<sub>2</sub> layers have become disordered after L-cysteine functionalization. Additionally, the appearance of (0 0 1) reflection peaks, combined with the absence of the (1 0 3) and (1 0 5) peaks in MoS<sub>2</sub>-Cys, suggests that the layers are stacked in a rotationally disordered structure [40]. It is proposed that such a disordered MoS<sub>2</sub> structure most likely originates from L-cysteine functionalization that is not limited to the edges of the flakes and occurs across the surface of the MoS<sub>2</sub> where COOH groups were attached corresponding to the locations of defect sites. Additional diffraction peaks in the range of 22–24° are inconsistent with crystallized L-cysteine or cystine and are assigned to disorder introduced by functionalization [41].

#### 4.3.2 Preferred Sensitivity to Cd<sup>2+</sup> ions

Fig. 4.5 shows a set of thin film membranes of MoS<sub>2</sub>-Cys on porous PES supports, as well as control membranes of MoS<sub>2</sub>-COOH. Membranes are prepared at varying volumes of MoS<sub>2</sub>-Cys and non-functionalized MoS<sub>2</sub>-COOH suspensions. Before functionalization with L-cysteine, the membranes are dark gray in color, which is similar to the original MoS<sub>2</sub> powder. After functionalization, both the solution and the resulting membranes on PES display a distinct brown color. To examine the performance of these devices in terms of metal ion capture from water, MoS<sub>2</sub>-COOH and MoS<sub>2</sub>-Cys membranes were immersed in solutions of CdCl<sub>2</sub> or MnCl<sub>2</sub> in water and allowed to rest for 24 hrs. After removing the membranes from water, the remaining concentration of metal ions in water was measured as a function of the ionic conductivity.

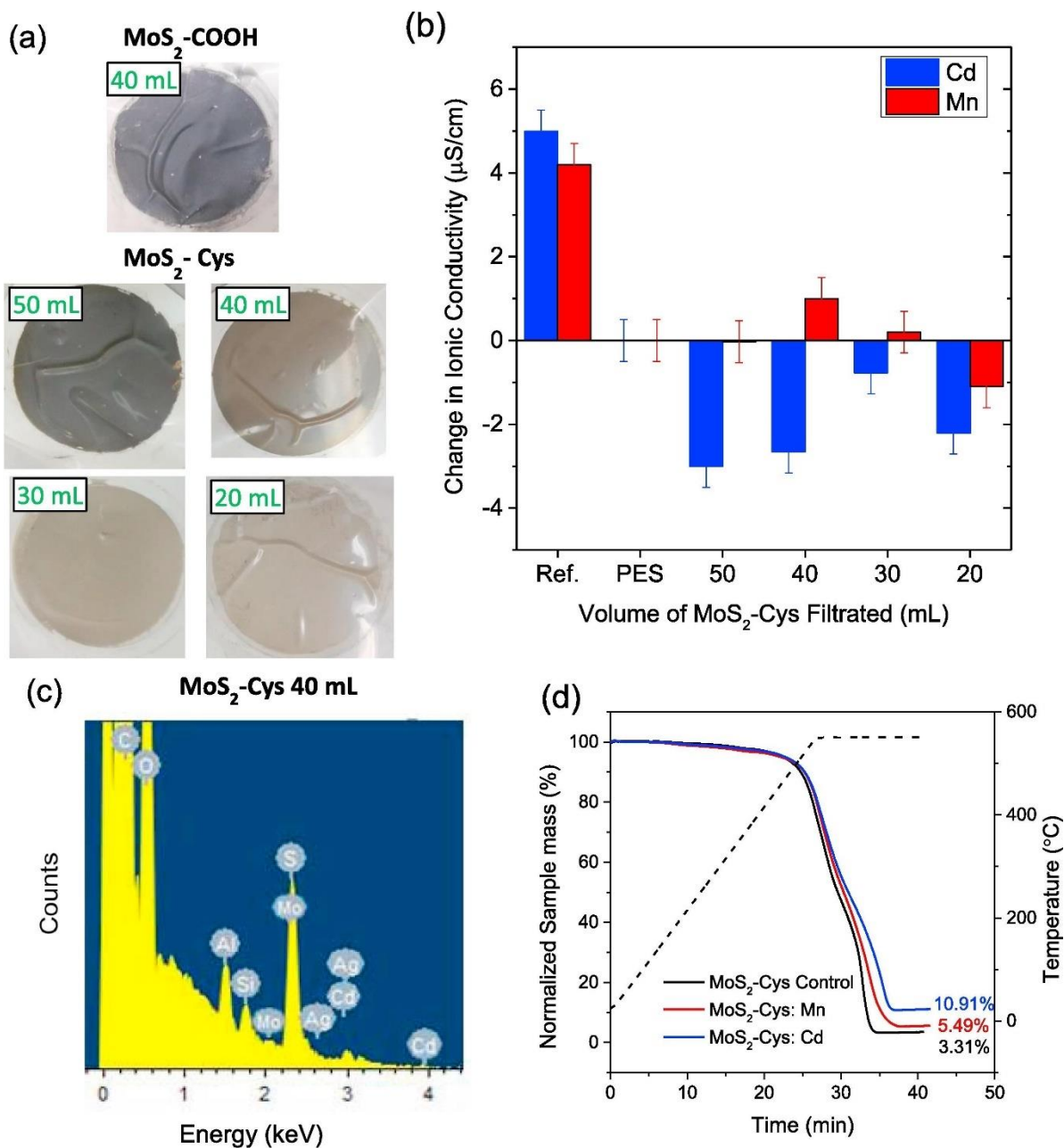


**Figure 4.5:** (a) Membranes prepared from MoS<sub>2</sub>-COOH or MoS<sub>2</sub>-Cys solution by vacuum filtration onto PES membranes (42 mm diameter) with different filtration volumes as labelled. (b) The change in ionic conductivity of a 10 ppm soaking solution due to adsorption of Cd or Mn metal ions versus the mass of MoS<sub>2</sub>-Cys deposited on the filter,

**compared to a bare PES support and a reference MoS<sub>2</sub>-COOH membrane. (c) EDX shows evidence of Cd absorbed to the surface MoS<sub>2</sub>-Cys, while Mn could not be detected on either MoS<sub>2</sub>-Cys or the MoS<sub>2</sub>-COOH reference (Fig. A3). Si, Al, and Ag signals are also present from the stub used to mount the sample, as well as from silver paste. (d) TGA analysis of MoS<sub>2</sub>-Cys after exposure to 50 ppm Mn or Cd metal ions in solution. Examination of the residual inorganic products shows a larger mass of absorbed Cd compared to Mn. The control sample was tested as-prepared without any metal ion exposure.**

The change in ionic conductivity of the metal ion solutions after membrane soaking is shown in Fig. 4.5(b) as a function of the volume of MoS<sub>2</sub>-Cys solution deposited to prepare the membranes. In all cases the tested MoS<sub>2</sub>-Cys membranes showed preferential absorption of Cd<sup>2+</sup> ions over Mn<sup>2+</sup>. A negligible change in the ionic conductivity of Mn<sup>2+</sup> solution is observed, and the bare PES support indicated negligible absorption of either metal ion. The variation in amount of Cd<sup>2+</sup> absorbed versus the volume of MoS<sub>2</sub>-Cys solution filtrated depends on the surface area of the membrane. When pressure filtration or stirring are not used, the absorption of ions on a membrane is a function of the exposed area, including the internal surface area of the membrane. The maximum absorption of Cd<sup>2+</sup> ions is observed for the functionalized membrane with the smallest area coverage, which is consistent with the hypothesis that L-cysteine functionalization mainly occurs at the edges of MoS<sub>2</sub> platelets. Fig. 4.5 also shows that, above a critical membrane thickness, a higher concentration of MoS<sub>2</sub>-Cys platelets is not leading to additional capture of Cd<sup>2+</sup> ions, as it does not expose a larger amount of functionalized MoS<sub>2</sub> platelets. Energy-dispersive X-ray (EDX) spectroscopy measurements (Fig. 4.5c, and values in Table 4.2) confirm the presence of Cd onto MoS<sub>2</sub>-Cys membranes after their immersion in water, while no evidence of Mn could not be detected, either on MoS<sub>2</sub>-Cys or

MoS<sub>2</sub>-COOH membranes (see Fig. S3). EDX measurements confirm the lack of metal absorption on the MoS<sub>2</sub>-COOH reference membranes, no Mn or Cd can be detected in either case.

The mass of Cd or Mn absorbed to the membranes was quantified more accurately using TGA as shown in Fig. 4.5(d). The TGA curves are similar for each MoS<sub>2</sub>-Cys sample tested, with the greatest mass of remaining inorganic material shown after soaking for 24 hrs in Cd<sup>2+</sup> ion solution. With knowledge of the starting masses of the control, Mn, and Cd exposed samples (1.1490 mg, 1.1630 mg, and 1.2710 mg, respectively) the mass of absorbed metal ions can be calculated. Considering that the films were prepared by vacuum filtration, the difference in film thickness between samples is taken into account with an error of 1.5% applied to the TGA final results. Applying this error to the final values shows that these MoS<sub>2</sub>-Cys membranes are capable of absorbing up to  $76 \pm 15$  mg Cd<sup>2+</sup> ions per gram of MoS<sub>2</sub>-Cys, compared to  $21 \pm 15$  mg/g for Mn. This interaction of Cd with MoS<sub>2</sub>-Cys makes these membranes suitable for absorption and sensing applications where there is a need to differentiate between metal ions in solution. The active mechanism of metal absorption is coordination to L-cysteine or cystine, making these membranes preferentially sensitive to metals such as Cd and Hg that coordinate with L-cysteine or cystine [42], [43]. Since cysteine functionals are required to absorb Cd, the concentration of cysteine used in the fabrication procedure can be varied to control the amount of Cd absorbed to the membrane.

The absorption uptake of Cd<sup>2+</sup> on MoS<sub>2</sub>-Cys is comparable to other materials designed for heavy metal absorption [44], [45], while additionally demonstrating ion selectivity. Graphene oxide and oxidized carbon nanotubes (CNT) are highly efficient at metal absorption by forming chemical bonds between oxide functional groups and dissolved metal ions, but are not selective [45], [31]. The large concentration of oxygen functional groups on graphene oxide or oxidized CNTs

provides absorption proportional to the surface area of the particles, making these materials are sensitive to a wide variety of aqueous metal ions including  $\text{Pb}^{2+}$ ,  $\text{Cu}^{2+}$ ,  $\text{Mn}^{2+}$ ,  $\text{Cr}^{3+,4+}$ ,  $\text{Ni}^{2+}$  and  $\text{Zn}^{2+}$  as well as Cd. By contrast  $\text{MoS}_2$ -Cys is shown to be sensitive specifically to Cd, while effectively ignoring other divalent metals such as Mn. From the Raman spectra in Fig. 4.3, the  $\text{MoS}_2$  nanosheets remain intrinsically semiconducting even after functionalization, making  $\text{MoS}_2$ -Cys well suited to electrochemistry or chemiresistor -based sensing applications.

$\text{Cd}^{2+}$  is the ideal target for this filtration apparatus as it has the proper coordination to bond with L-Cysteine (unlike other heavy metals Mn, Hg, etc.), it is also the correct size to fit in the functionalized cysteine complexes. Other metal ions such as Mn, though are approximately equal in size to cadmium, have drastically differing hydrodynamic radiuses, caused by there different electron configurations. Other contaminants (such as  $\text{Na}^+$ ) may be drastically too large or too small to be trapped by the functionalized  $\text{MoS}_2$ , even with similar coordination (such as Zn or Hg) and thus permeate through the filter. The combination of these two facts may allow us to selectively capture cadmium.

#### 4.4 Conclusion

In conclusion, we have demonstrated for the first time the functionalization of carboxylated  $\text{MoS}_2$  nanosheets with L-cysteine, an important amino acid possessing a reactive thiol group with an affinity for the critical divalent heavy metal ion Cd. Subsequently, we have shown that L-cysteine functionalized nanosheets have the potential to absorb Cd ions from water. Few layer  $\text{MoS}_2$ -COOH was obtained from an oxidization route that is relatively simple in comparison to the multi-step processes that are normally required to obtain competing carboxyl-functionalized water purification materials, particularly graphene oxide. Exfoliated  $\text{MoS}_2$ -COOH

nanosheets functionalized with L-cysteine can be readily suspended in water, and used to prepare thin film membranes with high surface area and strong potential as sorbants. Membranes fabricated from MoS<sub>2</sub>-Cys on porous supports are capable of selectively absorbing Cd<sup>2+</sup> ions up to 76 ± 15 mg/g depending on the concentration of cysteine used in the fabrication, while significantly lower absorption of other divalent ions such as Mn<sup>2+</sup> is observed.

Sensitivity to specific ions provides MoS<sub>2</sub>-Cys with capturing and detection capabilities that are normally not observed from competing materials for water filtration, including graphene oxide and carbon nanotubes. The preferential absorption of Cd<sup>2+</sup> cations makes functionalized molybdenum disulfide a strong candidate material for selective water purification, as well as a potential chemiresistor material to sense Cd<sup>2+</sup> from aqueous environments. This work introduces a new paradigm towards the functionalization of two-dimensional MoS<sub>2</sub> nanosheets for water purification and diagnostics applications, with the promise of high selectivity for the detection and removal of harmful metal ions from drinking water.

## 4.5 References

- [1] A. Aghigh, V. Alizadeh, H. Y. Wong, Md. S. Islamb, N. Amin, M. Zaman. **2015**, 365, 389.
- [2] J. Yin, B. Deng, *J. Membr. Sci.*, **2015**, 479, p. 256
- [3] J. Park, P. Bazylewski, G. Fanchini, *Nanoscale*, **2016**, 8, p. 9563
- [4] M. El Garaha, S. Bertolazzia, S. Ippolitoa, M. Erediaa, I. Janicab, *et al.*, *FlatChem*, **2018**, 9, p. 33-39
- [5] T. Das, J.-H. Ahn, *FlatChem*, **2017**, 3, p. 43-63
- [6] D. Lembke, A. Kis, *ACS Nano*, **2012**, 6, p. 10070
- [7] S. Kumari, H.P. Mungse, R. Gusain, N. Kumar, H. Sugimura, O.P. Khatri, *FlatChem*, **2017**, 3, pp. 16-25
- [8] G. Aragay, J. Pons, A. Merkoci, *Chem. Rev.*, **2011**, 111, p. 3433
- [9] J.W. Hamilton, R.C. Kaltreider, O.V. Bajenova, M.A. Ihnat, J. McCaffrey, B.W. Turpie, E. Rowell, J. Oh, M.J. Nemeth, C.A. Pesce, J.P. Lariviere, *J. Environ. Health.*, **1998**, 106, p. 1005
- [10] B.L. Vallee, D. Ulmer, *Annu. Rev. Biochem.*, **1972**, 41, p. 91
- [11] T. Partanen, P. Heikkila, S. Hernberg, T. Kauppinen, G. Moneta, A. Ojajarvi *Scand. J. Work Environ. Health.*, **1991**, 17, p. 231
- [12] J. Gasparik, D. Vladarova, M. Capcarova, P. Smehyl, J. Slamecka, P. Garaj, R. Stawarz, P.J. Massanyi, *Environ. Sci. Health A*, **2010**, 45, p. 818
- [13] T. Townsend, K.A. Miller, S. McLean, S.J. Aldous, *ICP-MS Anal. At. Spectrom.*, **1998**, 13, p. 1213

- [14] R. Flamini, A. Panighel, *Mass. Spectrom. Rev.*, **2006**, 25, p. 741
- [15] F.E. McNeill, J.M. O'Meara, *Adv. X-ray Anal.*, **1999**, 41, p. 910
- [16] N.D. Rudd, H. Wang, E.M.A. Fuentes, Fernandez, S.J. Teat, F. Chen, G. Hall, Y. J. Chabal, J. Li, *ACS Appl. Mater. Inter.*, **2016**, 8, p. 30294
- [17] Y. Zhou, L. Tang, G. Zeng, C. Zhang, Y. Zhang, X. Xie, *Sens. Actuators B.*, **2016**, 223, p. 280
- [18] B.K. Bansoda, T. Kumar, R. Thakur, S. Rana, I. Singh, *Biosens. Bioelectron.*, **2017**, 94, p. 443
- [19] L. Pujol, D. Evrard, K. Groenen-Serrano, M. Freyssinier, A. Ruffien-Cizsak, P. Gros, *Front. Chem.*, **2014**, 2, p. 1
- [20] M. Hua, S. Zhang, B. Pan, W. Zhang, L. Lv, Q. Zhang, *J Hazard Mater.*, **2012**, 211, p. 317
- [21] M. Li, H. Gou, I. Al-Ogaidi, N. Wu, *ACS Sust. Chem. Eng.*, **2013**, 1, p. 713
- [22] X. Xuan, Md.F. Hossain, J.Y. Park, *Sci. Rep.*, **2016**, 6, p. 33125
- [23] K. Mao, Z. Wu, Y. Chen, X. Zhou, A. Shen, J. Hu, *Talanta*, **2015**, 132, p. 658
- [24] S. Wu, Z. Zeng, Q. He, Z. Wang, S.J. Wang, Y. Du, Z. Yin, X. Sun, W. Chen, H. Zhang, *Small*, **2012**, 8, p. 2264
- [25] P. Li, D. Zhang, Y. Sun, H. Chang, J. Liu, N. Yin, *Appl. Phys. Lett.*, **2015**, 109, 063110
- [26] X.-F. Shen, X.-P. Yan, *J. Mater. Chem.*, **2008**, 18, p. 4631

- [27] S. Xiong, B. Xi, C. Wang, G. Zou, L. Fei, W. Wang, Y. Qian, *Chem. Eur. J.*, **2007**, 13, p. 3076
- [28] A. Khataee, A. Movafeghi, F. Nazari, F. Vafaei, M.R. Dadpour, Y. Hanifehpour, S.W.Joo, *J. Nanopart. Res.*, **2014**, 16, p. 2774
- [29] R. Anbazhagan, H.-J. Wang, H.-C. Tsai, R.-J. Jeng, *RSC Adv.*, **2014**, 4, p. 42936
- [30] A.K. Mishra, K.V. Lakshmi, L. Huang, *Sci. Rep.*, **2015**, 5, p. 15718
- [31] J.-S. Kim, H.-W. Yoo, H.O. Choi, H.-T. Jung, *Nano. Lett.*, **2014**, 14, p. 5941
- [32] B.C. Windom, W.G. Sawyer, D.W. Hahn, *Tribol. Lett.*, **2011**, 42, p. 301
- [33] M. Dieterle, G. Mestl, *Phys. Chem. Phys.*, **2002**, 4, p. 822
- [34] M. Placidi, M. Dimitrievska, V. Izquierdo-Roca, X. Fontané, A. Castellanos-Gomez, A. Pérez-Tomás, N. Mestres, M. Espindola-Rodriguez, S. López-Marino, M. Neuschitzer, V. Bermudez, A. Yaremko, A. Pérez-Rodríguez, *2D Mater.*, **2015**, 2, 035006
- [35] P. Bazylewski, R. Divigalpitiya, G. Fanchini, *RSC Adv.*, **2017**, 7, p. 2964
- [36] S. Chou, M. De, J. Kim, S. Byun, C. Dykstra, J. Yu, J. Huang, V. Dravid  
*J. Am. Chem. Soc.*, **2013**, 135, p. 4584
- [37] L. Li, Q. Zhang, Y. Ding, X. Cai, S. Gua, Z. Cao, *Anal. Methods.*, **2014**, 6, p. 2715
- [38] R. Sitko, E. Turek, B. Zawisza, E. Malicka, E. Talik, J. Heimann, A. Gagor, B. Feista, R. Wrzalik, *Dalton Trans.*, **2013**, 42, p. 5682

- [39] W.M.R. Divigalpitiya, S.R. Morrison, R.F. Frindt, *Thin Solid Films.*, **1990**, 186, p. 177
- [40] P. Joensen, E.D. Crozier, N. Alberding, R.F. Frindt, *J. Phys. C: Solid State Phys.*, **1987**, 20, p. 4043
- [41] C. Foces-Foces, M.V. Roux, R. Notario, M. Segura, *J. Therm. Anal. Calorim.*, **2011**, 105, p. 747
- [42] J.G. Parsons, K.M. Dokken, J. McClure, J.-L. Gardea-Torresdey, *Polyhedron*, **2013**, 56, p. 237
- [43] E. Furia, G. Sindona, *J. Chem. Eng. Data*, **2010**, 55, p. 2985
- [44] M.A. Tofighy, T. Mohammadi, *J. Hazard. Mater.*, **2011**, 185, p. 140
- [45] B. Xu, Y. Su, L. Li, R. Liu, Y. Lv, *Sens. Actuators B.*, **2017**, 246, p. 380

## Chapter 5

### 5.1 Conclusion

In chapter 3, I described a novel apparatus design which allows for the selective capture and detection of heavy metal divalent cations in water. This is done by the use of a computer operated low cost data acquisition card (DAQ) which is controlled by a MATLAB<sup>®</sup> routine. This software runs IV curves between two Al electrodes which have been thermally evaporated onto poly(ether)sulfone (PES) microporous membranes. The distance (or gap) between electrodes is on the order of 10 microns and is formed by the use of a shadow mask in the thermal evaporator. These membranes allowed us to vacuum filter graphite solution onto the PES creating a filter cake. This filter cake is made from multilayer graphene which has been exfoliated in a PEG-PPG-PEG and water solution. The molecular weight of the PEG-PPG-PEG copolymer used in exfoliation was found to change the c-axis interlayer spacing of the MLG. This finding was then exploited in order to ‘fine-tune’ the interlayer spacing to the ideal electrostatic distance between the layer of graphene for the heavy metal divalent cations to become trapped. A comparison was made between turbostratic synthetic graphite and natural hydrothermal vein graphite. The natural hydrothermal vein graphite showed improved sensing performance. A combination of SEM, Raman and EPR characterization were utilized to show that the natural hydrothermal vein graphite was of superior quality to its synthetic counterpart and thus explains the better performance due to the higher affinity of the surfactant to the graphene layers.

In chapter 4, we investigated a new technique for the selective capture of heavy metals in water, specific attention was given to cadmium for its vast use in industry. Due to the well-known affinity of L-Cysteine to the metal ions as exemplified by its use in coating of heavy metal

particles L-Cysteine was the optimal choice. Using a simple method of exfoliating MoS<sub>2</sub> using thioglycolic acid (TGA), we were then able to functionalize MoS<sub>2</sub> with L-Cysteine using an amide cross linking reaction. After the functionalization, AFM and SEM characterization techniques were implemented to investigate the morphology of the MoS<sub>2</sub> flakes. Raman and XRD were used to verify the degree of functionalization as well as to gain information about the structure of MoS<sub>2</sub>. Filtration tests were performed by measuring the change in ionic conductivity before and after filtration. EDX was also performed to estimate the amount of Cd which had been absorbed by the filter cake. Volumes of MoS<sub>2</sub> solution used to create the filter cakes were altered in order to create a parametric study of the effectiveness of filtration.

## 5.2 Future Work

There is a great deal of potential work that is possible in the future for the use of multi layer graphene sensing apparatus in chapter 3 for other applications. Further verification of the defects within MLG should be investigated by looking at the diffraction pattern from a tunneling electron microscopy (TEM) of the MLG sample. X-ray photoelectron spectroscopy (XPS) could also be done to test for possible retention of Cd<sup>2+</sup> in the MLG. Foremost however, would be to investigate how tunable the MLG is to PEG-PPG-PEG, and how that could be utilized to select for different heavy metal ions. This not only would better verify the effect observed in chapter 3, but also implies that this technique could be used to selectively detect a wide variety of harmful heavy metals. Additionally, some work has been done looking at the absorption of poly aromatic hydrocarbons (PAHs) onto graphene, which has shown that the PAHs act as an n-dopant. [1] This may cause a noticeable change in the conductivity of the MLG within the gap cell of the device and thus be detectable.

In chapter 4 we investigated, L-Cysteine functionalized MoS<sub>2</sub> to selectively capture MoS<sub>2</sub>. This could be utilized in the sensing apparatus discussed in chapter 3 and perhaps also allow for the selective, and pH tunable sensing of Cd divalent cations in water. In fact, although not included in this thesis, Dr. Paul Bazylewski, Prof. Fanchini and I are currently in the process of publishing this work. We could also look at functionalizing MoS<sub>2</sub> with different amino acids to capture and sense other heavy metal ions. Further investigation into the chemical components absorbed by the filter could be done by X-ray photoelectron spectroscopy (XPS). Also, further study of the bonding mechanism between L-Cysteine and Cd<sup>2+</sup> would be helpful to both determine methods of optimizing the current filtration design, as well as finding other compounds which can functionalize MoS<sub>2</sub> to selectively capture heavy metal ions.

## References

[1] B. Li, P. Ou, Y. Wei, X. Zhang, J. Song, *Materials*, **2018**, 11(5), 726

### 5.3 List of Permissions

Figures 1.2 and 2.4

License: CC BY-SA 4.0

For the fulfilment of licence agreement, a link is provided.

URL: <https://creativecommons.org/licenses/by-sa/4.0/>

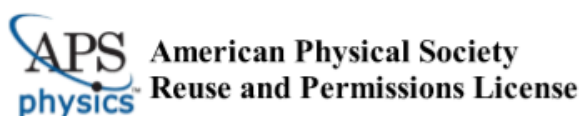
Figures 1.6 and 2.7

Licence: CC BY-NC-ND 3.0

For the fulfilment of licence agreement, a link to said URL is provided.

URL: <https://creativecommons.org/licenses/by-nc-nd/3.0/>

Figure 1.3



16-Jul-2019

This license agreement between the American Physical Society ("APS") and Sheldon Van Middelkoop ("You") consists of your license details and the terms and conditions provided by the American Physical Society and SciPris.

#### Licensed Content Information

**License Number:** RNP/19/JUL/016710  
**License date:** 16-Jul-2019  
**DOI:** 10.1103/RevModPhys.81.109  
**Title:** The electronic properties of graphene  
**Author:** A. H. Castro Neto et al.  
**Publication:** Reviews of Modern Physics  
**Publisher:** American Physical Society  
**Cost:** USD \$ 0.00

#### Request Details

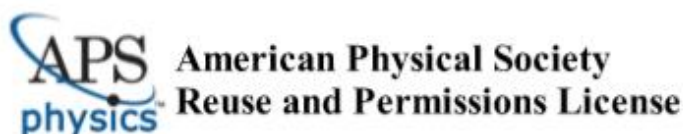
**Does your reuse require significant modifications:** No  
**Specify intended distribution locations:** Canada  
**Reuse Category:** Reuse in a thesis/dissertation  
**Requestor Type:** Student  
**Items for Reuse:** Figures/Tables  
**Number of Figure/Tables:** 1  
**Figure/Tables Details:** Figure 2: Illustration of honeycomb lattice and its Brillouin zone.  
**Format for Reuse:** Electronic

#### Information about New Publication:

**University/Publisher:** University of Western Ontario  
**Title of dissertation/thesis:** Application of 2D Materials to In-line Chemiresistor Cadmium Dication Detection in Water  
**Author(s):** Sheldon Van Middelkoop  
**Expected completion date:** Jul. 2019

#### License Requestor Information

**Name:** Sheldon Van Middelkoop  
**Affiliation:** Individual  
**Email Id:** svanmidd@uwo.ca  
**Country:** Canada

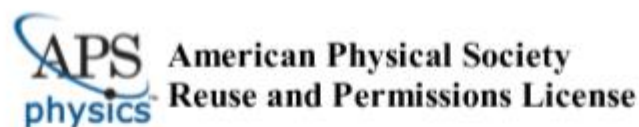


#### TERMS AND CONDITIONS

The American Physical Society (APS) is pleased to grant the Requestor of this license a non-exclusive, non-transferable permission, limited to Electronic format, provided all criteria outlined below are followed.

1. You must also obtain permission from at least one of the lead authors for each separate work, if you haven't done so already. The author's name and affiliation can be found on the first page of the published Article.
2. For electronic format permissions, Requestor agrees to provide a hyperlink from the reprinted APS material using the source material's DOI on the web page where the work appears. The hyperlink should use the standard DOI resolution URL, <http://dx.doi.org/{DOI}>. The hyperlink may be embedded in the copyright credit line.
3. For print format permissions, Requestor agrees to print the required copyright credit line on the first page where the material appears: "Reprinted (abstract/excerpt/figure) with permission from [(FULL REFERENCE CITATION) as follows: Author's Names, APS Journal Title, Volume Number, Page Number and Year of Publication.] Copyright (YEAR) by the American Physical Society."
4. Permission granted in this license is for a one-time use and does not include permission for any future editions, updates, databases, formats or other matters. Permission must be sought for any additional use.
5. Use of the material does not and must not imply any endorsement by APS.
6. APS does not imply, purport or intend to grant permission to reuse materials to which it does not hold copyright. It is the requestor's sole responsibility to ensure the licensed material is original to APS and does not contain the copyright of another entity, and that the copyright notice of the figure, photograph, cover or table does not indicate it was reprinted by APS with permission from another source.
7. The permission granted herein is personal to the Requestor for the use specified and is not transferable or assignable without express written permission of APS. This license may not be amended except in writing by APS.
8. You may not alter, edit or modify the material in any manner.
9. You may translate the materials only when translation rights have been granted.
10. APS is not responsible for any errors or omissions due to translation.
11. You may not use the material for promotional, sales, advertising or marketing purposes.
12. The foregoing license shall not take effect unless and until APS or its agent, Aptara, receives payment in full in accordance with Aptara Billing and Payment Terms and Conditions, which are incorporated herein by reference.
13. Should the terms of this license be violated at any time, APS or Aptara may revoke the license with no refund to you and seek relief to the fullest extent of the laws of the USA. Official written notice will be made using the contact information provided with the permission request. Failure to receive such notice will not nullify revocation of the permission.
14. APS reserves all rights not specifically granted herein.
15. This document, including the Aptara Billing and Payment Terms and Conditions, shall be the entire agreement between the parties relating to the subject matter hereof.

Figure 1.4



16-Jul-2019

This license agreement between the American Physical Society ("APS") and Sheldon Van Middelkoop ("You") consists of your license details and the terms and conditions provided by the American Physical Society and SciPris.

#### Licensed Content Information

<b>License Number:</b>	RNP/19/JUL/016711
<b>License date:</b>	16-Jul-2019
<b>DOI:</b>	10.1103/RevModPhys.81.109
<b>Title:</b>	The electronic properties of graphene
<b>Author:</b>	A. H. Castro Neto et al.
<b>Publication:</b>	Reviews of Modern Physics
<b>Publisher:</b>	American Physical Society
<b>Cost:</b>	USD \$ 0.00

#### Request Details

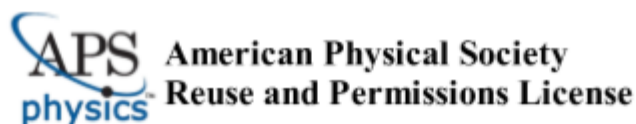
<b>Does your reuse require significant modifications:</b>	No
<b>Specify intended distribution location:</b>	Canada
<b>Reuse Category:</b>	Reuse in a thesis/dissertation
<b>Requestor Type:</b>	Student
<b>Items for Reuse:</b>	Figures/Tables
<b>Number of Figure/Tables:</b>	1
<b>Figure/Tables Details:</b>	Band structure of graphene. The Dirac cone
<b>Format for Reuse:</b>	Electronic

#### Information about New Publication:

<b>University/Publisher:</b>	University of Western Ontario
<b>Title of dissertation/thesis:</b>	Application of 2D Materials to In-line Chemiresistor Cadmium Dication Detection in Water
<b>Author(s):</b>	Sheldon Van Middelkoop
<b>Expected completion date:</b>	Jul. 2019

#### License Requestor Information

<b>Name:</b>	Sheldon Van Middelkoop
<b>Affiliation:</b>	Individual
<b>Email Id:</b>	svanmidd@uwo.ca
<b>Country:</b>	Canada

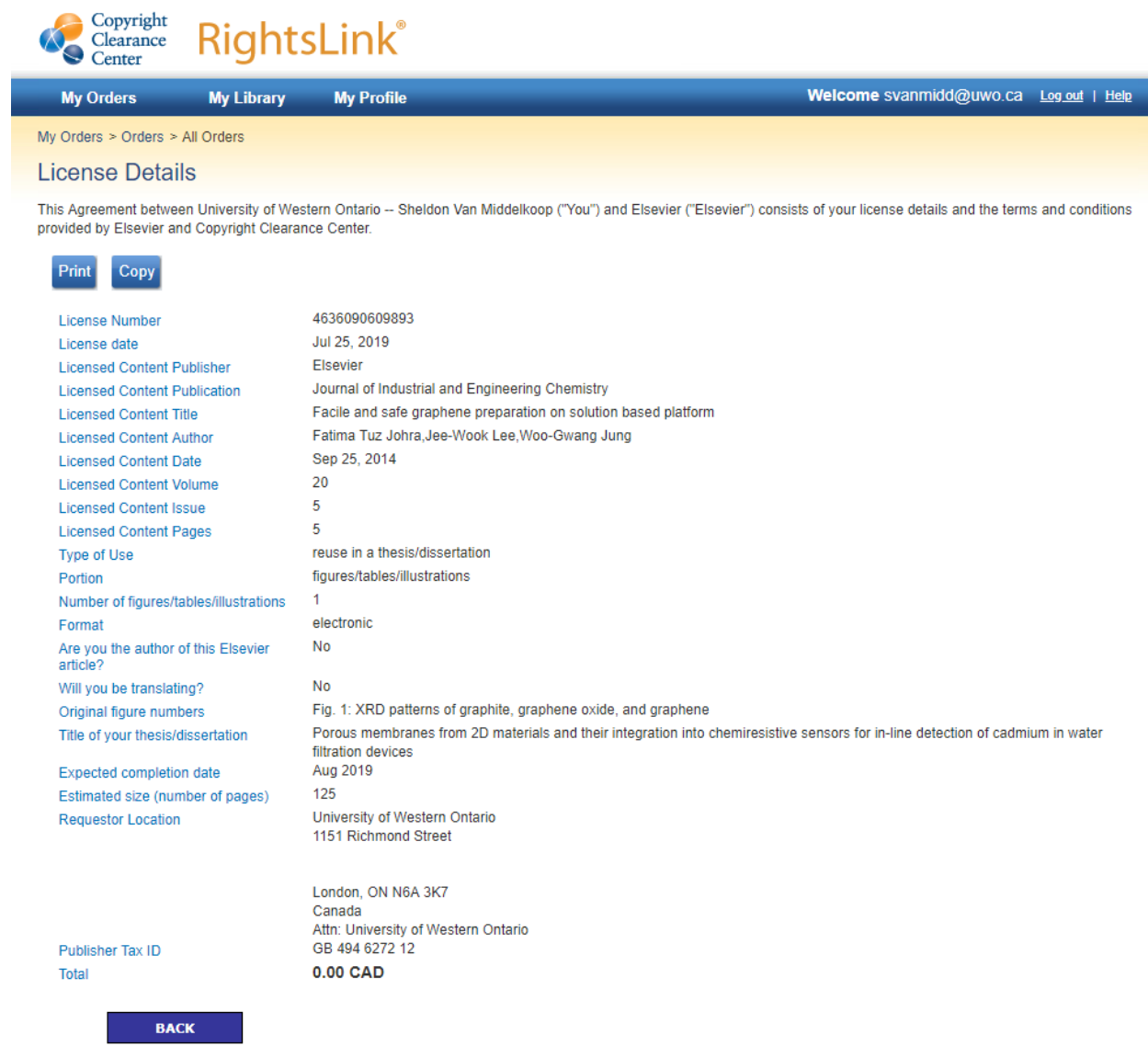


#### TERMS AND CONDITIONS

The American Physical Society (APS) is pleased to grant the Requestor of this license a non-exclusive, non-transferable permission, limited to Electronic format, provided all criteria outlined below are followed.

1. You must also obtain permission from at least one of the lead authors for each separate work, if you haven't done so already. The author's name and affiliation can be found on the first page of the published Article.
2. For electronic format permissions, Requestor agrees to provide a hyperlink from the reprinted APS material using the source material's DOI on the web page where the work appears. The hyperlink should use the standard DOI resolution URL, <http://dx.doi.org/DOI>. The hyperlink may be embedded in the copyright credit line.
3. For print format permissions, Requestor agrees to print the required copyright credit line on the first page where the material appears: "Reprinted (abstract/excerpt/figure) with permission from [(FULL REFERENCE CITATION) as follows: Author's Names, APS Journal Title, Volume Number, Page Number and Year of Publication.] Copyright (YEAR) by the American Physical Society."
4. Permission granted in this license is for a one-time use and does not include permission for any future editions, updates, databases, formats or other matters. Permission must be sought for any additional use.
5. Use of the material does not and must not imply any endorsement by APS.
6. APS does not imply, purport or intend to grant permission to reuse materials to which it does not hold copyright. It is the requestor's sole responsibility to ensure the licensed material is original to APS and does not contain the copyright of another entity, and that the copyright notice of the figure, photograph, cover or table does not indicate it was reprinted by APS with permission from another source.
7. The permission granted herein is personal to the Requestor for the use specified and is not transferable or assignable without express written permission of APS. This license may not be amended except in writing by APS.
8. You may not alter, edit or modify the material in any manner.
9. You may translate the materials only when translation rights have been granted.
10. APS is not responsible for any errors or omissions due to translation.
11. You may not use the material for promotional, sales, advertising or marketing purposes.
12. The foregoing license shall not take effect unless and until APS or its agent, Aptara, receives payment in full in accordance with Aptara Billing and Payment Terms and Conditions, which are incorporated herein by reference.
13. Should the terms of this license be violated at any time, APS or Aptara may revoke the license with no refund to you and seek relief to the fullest extent of the laws of the USA. Official written notice will be made using the contact information provided with the permission request. Failure to receive such notice will not nullify revocation of the permission.
14. APS reserves all rights not specifically granted herein.
15. This document, including the Aptara Billing and Payment Terms and Conditions, shall be the entire agreement between the parties relating to the subject matter hereof.

Figure 2.6



The screenshot displays the RightsLink interface. At the top left is the Copyright Clearance Center logo. The main header features the RightsLink logo and navigation links for 'My Orders', 'My Library', and 'My Profile'. A welcome message for 'svanmidd@uwo.ca' is visible on the right, along with 'Log out' and 'Help' links. Below the header, a breadcrumb trail reads 'My Orders > Orders > All Orders'. The main section is titled 'License Details' and contains a paragraph explaining the agreement between the University of Western Ontario and Elsevier. Two buttons, 'Print' and 'Copy', are provided. A detailed list of license information follows, including fields like License Number, License date, Licensed Content Publisher, Licensed Content Publication, Licensed Content Title, Licensed Content Author, Licensed Content Date, Licensed Content Volume, Licensed Content Issue, Licensed Content Pages, Type of Use, Portion, Number of figures/tables/illustrations, Format, Are you the author of this Elsevier article?, Will you be translating?, Original figure numbers, Title of your thesis/dissertation, Expected completion date, Estimated size (number of pages), Requestor Location, and Publisher Tax ID. The total cost is listed as 0.00 CAD. A 'BACK' button is located at the bottom of the license details section.

Copyright Clearance Center  
RightsLink®

My Orders My Library My Profile Welcome svanmidd@uwo.ca Log out | Help

My Orders > Orders > All Orders

## License Details

This Agreement between University of Western Ontario -- Sheldon Van Middelkoop ("You") and Elsevier ("Elsevier") consists of your license details and the terms and conditions provided by Elsevier and Copyright Clearance Center.

[Print](#) [Copy](#)

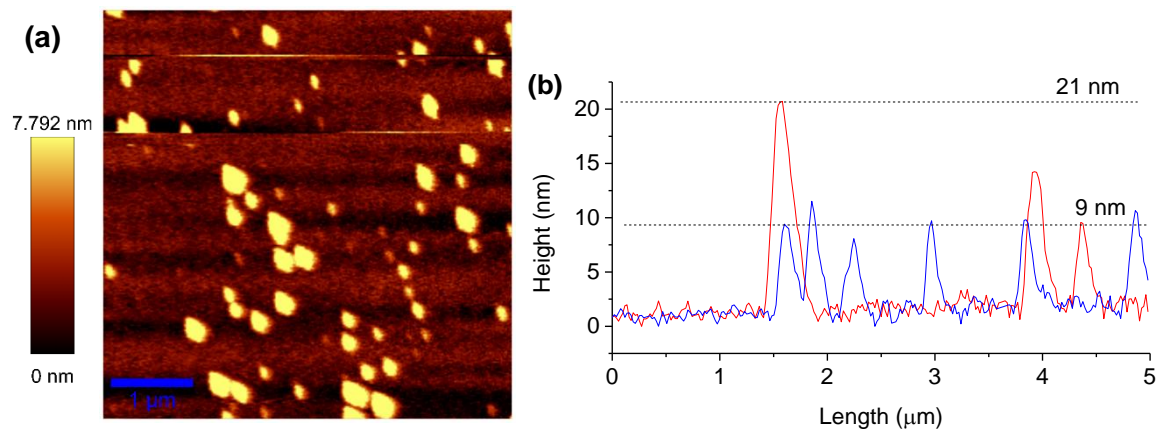
License Number	4636090609893
License date	Jul 25, 2019
Licensed Content Publisher	Elsevier
Licensed Content Publication	Journal of Industrial and Engineering Chemistry
Licensed Content Title	Facile and safe graphene preparation on solution based platform
Licensed Content Author	Fatima Tuz Johra, Jee-Wook Lee, Woo-Gwang Jung
Licensed Content Date	Sep 25, 2014
Licensed Content Volume	20
Licensed Content Issue	5
Licensed Content Pages	5
Type of Use	reuse in a thesis/dissertation
Portion	figures/tables/illustrations
Number of figures/tables/illustrations	1
Format	electronic
Are you the author of this Elsevier article?	No
Will you be translating?	No
Original figure numbers	Fig. 1: XRD patterns of graphite, graphene oxide, and graphene
Title of your thesis/dissertation	Porous membranes from 2D materials and their integration into chemiresistive sensors for in-line detection of cadmium in water filtration devices
Expected completion date	Aug 2019
Estimated size (number of pages)	125
Requestor Location	University of Western Ontario 1151 Richmond Street  London, ON N6A 3K7 Canada Attn: University of Western Ontario GB 494 6272 12
Publisher Tax ID	
Total	<b>0.00 CAD</b>

[BACK](#)

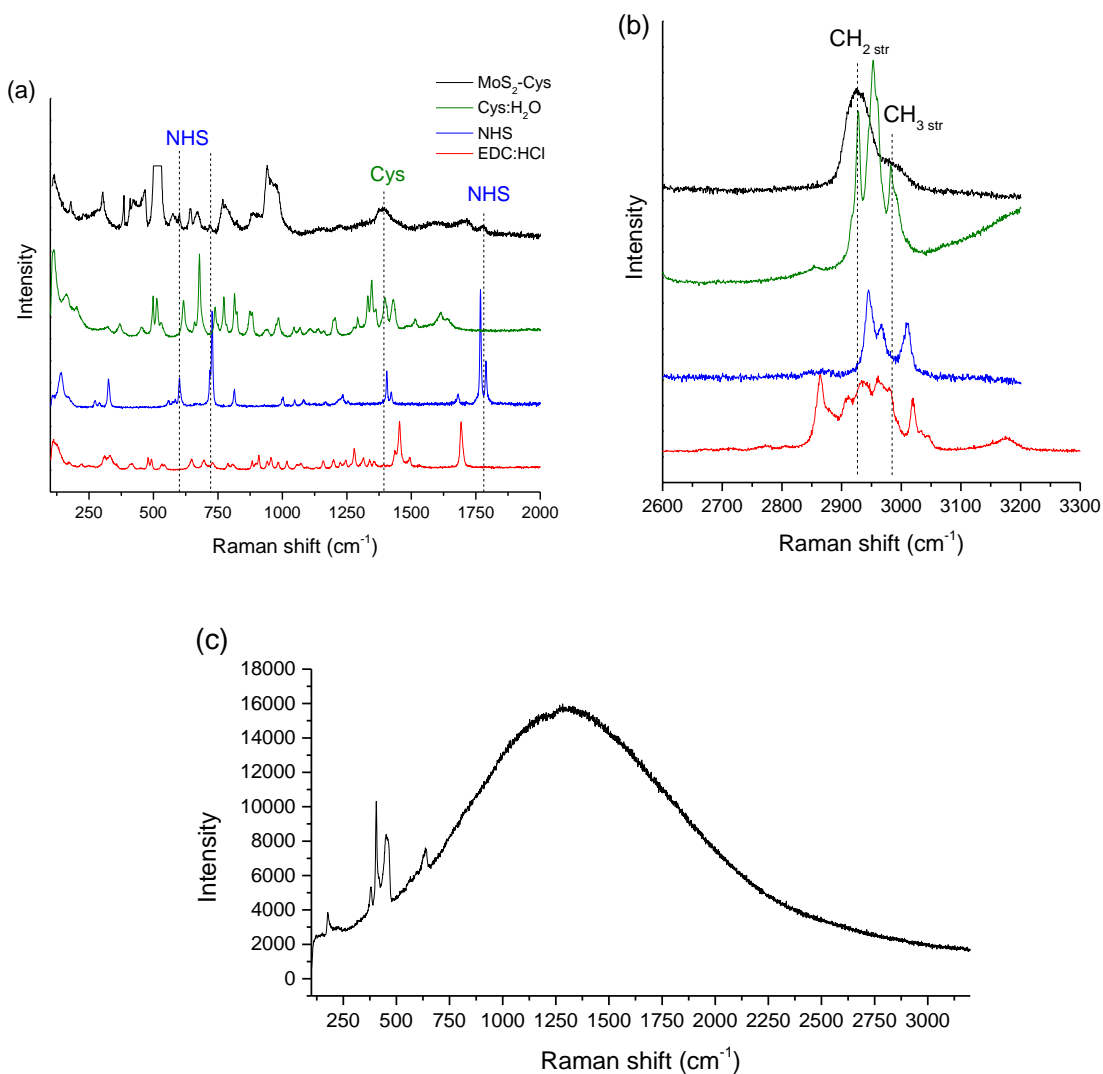
## 5.4 Chapter 4 Appendix

### **Table of Contents**

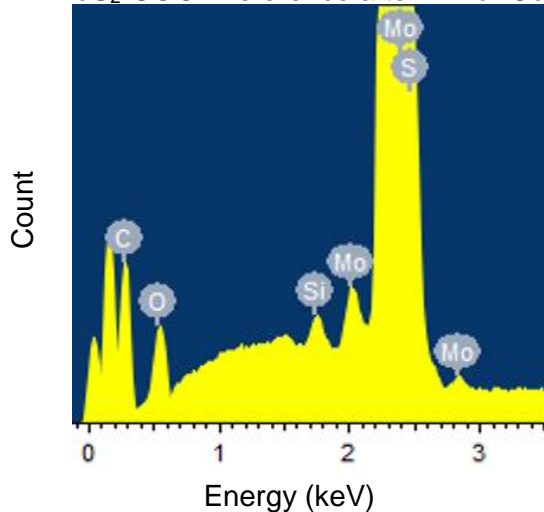
Figure A1. AFM image and cross-section of MoS <sub>2</sub> -Cys.....	109
Figure A2. Raman of reference materials used in MoS <sub>2</sub> -Cys synthesis.....	110
Figure A3. EDX measurements of the MoS <sub>2</sub> after Cd or Mn.....	111



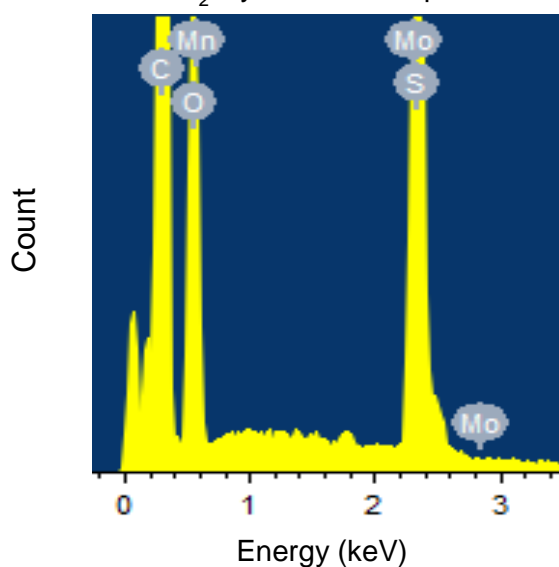
**Figure A1:** (a) AFM image of MoS<sub>2</sub>-Cys deposited on a track etched polycarbonate filter. (b) Cross-sections to examine the size of the flakes show that after functionalization they do not increase significantly in height, but are marginally larger in size laterally, with a size range of 200-450 nm.



**Figure A2:** Raman of reference materials used in MoS<sub>2</sub>-Cys synthesis: NHS and EDC showing (a) low and (b) high frequency regions. (c) The spectrum of micro crystalline MoS<sub>2</sub> powder. The large background peak resulting from excitation with the 633 nm laser is clearly visible.

**(a)** MoS<sub>2</sub>-COOH reference after Mn or Cd**MoS<sub>2</sub>-COOH element percentages**

Element	Weight%	Atomic%
C K	33.15	64.99
O K	5.09	7.49
Si K	0.23	0.20
S K	25.02	18.37
Mo L	36.50	8.96
Mn K	0.00	0.00
Cd L	0.00	0.00

**(b)** MoS<sub>2</sub>-Cys after Mn exposure**MoS<sub>2</sub>-Cys element percentages**

Element	Weight%	Atomic%
C K	66.94	76.65
O K	23.60	20.29
S K	5.96	2.56
Mo L	3.50	0.50
Mn K	0.00	0.00

**Figure S3:** (a) EDX measurements of the reference sample MoS<sub>2</sub>, after exposure to Mn or Cd ions in solution. Signals arising from these two elements are not evident in the reference. (b) EDX spectrum of MoS<sub>2</sub>-Cys after exposure to Mn ions only. Similar to the reference, no trace of absorbed Mn can be detected on the sample. The tables to the right of each spectra show the associated element percentages.

## 5.5 Curriculum Vitae

### Sheldon Van Middelkoop

*Masters of Science, Western University*

#### Academic studies

- Sep. 2017–  
Aug. 2019 **Master of Science**, *Experimental Condensed Matter Physics*, Western University,  
Thesis Supervisor: Dr. Giovanni Fanchini.
- Sep. 2012–  
Sept. 2017 **Bachelor of Science**, *Physics*, Wilfrid Laurier University,  
Undergraduate Thesis Supervisor: Dr. Ian Hamilton.

#### Work experience

##### Wilfrid Laurier University

- Sep. 2016–  
Dec. 2016 **Instructional Assistant for the Physics and Astronomy Department.**  
Lab demonstrator for second year electronics labs
- May. 2017–  
Aug. 2017 **Undergraduate Research Assistant.**  
Assisted in running density functional theory simulations on graphene quantum dots.

##### Western University

- Sep. 2017–  
May. 2019 **Teaching Assistant for the Physics and Astronomy Department.**  
Lab demonstrator for first year labs
- Sep. 2017–  
Aug. 2019 **Graduate Research Assistant,**  
*Utilizing 2D materials for in a chemiresistor architecture for metal ion detection in water..*

#### Publications

##### Published

- I. Haranas, O. Ragos, I. Gkigkitzis, I. Kotsireas, C. Martz, and **S. Van Middelkoop**.  
"The Poynting-Robertson effect in the Newtonian potential with a Yukawa correction".  
*Astrophysics and Space Science*, **3**:363, (2018).
- P. Bazylewski, **S. Van Middelkoop**, R. Divigalpitiya, and G. Fanchini.  
"Cysteine-functionalized molybdenum disulphide membranes for heavy metal ion  
capture and sensing", (2018).
- C. Martz, **S. Van Middelkoop**, I. Gkigkitzis, and I. Haranas. "Yukawa potential orbital  
energy and its relation to orbital mean motion as well to the graviton mediating the  
interaction in celestial bodies", (2018).
- S. Van Middelkoop**, A. Cen, and G. Fanchini. "Graphene based solid-state chemristor  
device for selective water filtration and sensing of cadmium dications", (2019).

### Submitted

**P. Bazylewski**, S. Van Middelkoop, R. Divigalpitiya, and G. Fanchini. "*Mos2 chemiresistors functionalized with l-cysteine for ph-tunable detection of metal ions in water*", (2019).

---

### Conferences

- o 102nd Canadian Chemistry Conference and Exhibition (June 2019)  
Few-layer graphene sensors for the detection of Cd<sup>2+</sup> ions during water purification processes